

CONVECTIVE STORM DEVELOPMENT IN CONTRASTING
THERMODYNAMIC AND KINEMATIC ENVIRONMENTS

Zur Erlangung des akademischen Grades eines
DOKTORS DER NATURWISSENSCHAFTEN
von der Fakultät für Physik
der Universität Karlsruhe (TH)

genehmigte

DISSERTATION

von

Pieter Groenemeijer, M.Sc.
aus Haarlem (Niederlande)

Tag der mündlichen Prüfung: 22. Mai 2009

Referent: Prof. Dr. Ch. Kottmeier

Korreferent: Prof. Dr. K. D. Beheng

Abstract

The characteristics of deep moist convection in the troposphere strongly depend on the thermodynamic and kinematic environment in which it occurs. In particular, the relative strength of vertical wind shear in comparison to buoyancy forces has a strong influence on the dynamics of a convective storm, which has implications for its longevity and severity. By means of two case studies, one of a situation in which buoyancy forces dominated over shear-induced forces, and one in which shear was at least as important as buoyancy, the dynamical differences are explored. Mesoscale processes that act near convective storms in these two very different environments, are highlighted. In the weak vertical shear case study, observations of the downward branch of the convective circulation are discussed. It is demonstrated that part of this downward motion is not induced by hydrometeor phase changes, water loading, or dynamically-forced pressure perturbations, but instead by buoyancy-induced pressure gradients. The resulting warm, dry, and subsiding flow, that spreads out horizontally above the boundary layer, is identified as a likely cause for the lack of secondary convective initiation near the initial storm system. The downdraught air increases convective inhibition as a combined result of a temperature increase above the boundary layer, and downward mixing of dry air into the boundary layer. The second case study focuses on the development of a convective storm exhibiting a rotating updraught and a strong tornado in downtown Birmingham, UK. For this case, it is shown that strong vertical wind shear was important for the storm's behaviour, and that the rotation in the storm's updraught can be reproduced by a numerical model, run with 1.1 kilometre grid spacing. Additionally, it is found that only within a 30–50 km wide zone, located on the immediate cold side of a warm front, sufficient Convective Available Potential Energy (CAPE) and wind shear were present to sustain such rotating mini-supercell storms. Within the zone, total CAPE was still relatively low, but a relatively high fraction of it was located in the lowest few kilometres, producing a similar environment as found in hurricane rain-bands, that several studies have shown to frequently contain mini-supercells. Finally, with a concise literature review, the notion shown that the absence or presence of wind shear has important implications for the probability, type and intensity of severe weather is reinforced. This enables weather forecasters to assess the severe weather threat posed by convective storms based on environmental parameters when accurate explicit numerical simulations are not available.

Contents

1	Introduction	5
2	Convective instability	7
2.1	One-dimensional assessments of instability	8
2.1.1	Absolute instability	8
2.1.2	Conditional instability	9
2.1.3	Potential instability	10
2.1.4	Thermal buoyancy and latent instability	10
2.1.5	Comparison of different instability concepts	13
2.2	Variability of thermodynamic parameters	15
3	Convection in weak vertical wind shear	21
3.1	Perturbation pressure and flow adjustment to thermal buoyancy	21
3.2	The PRINCE measurement campaign	25
3.3	Measurement systems	26
3.4	Meteorological set-up	27
3.5	Convective initiation	30
3.6	The mature and decaying storm system	33
3.7	Inhibition by compensatory subsidence	41
3.8	Discussion and conclusions	42
4	Convection in strong vertical wind shear	43
4.1	Convection in unidirectional shear	44
4.2	Convection in shear turning with height	47
4.3	A Richardson Number	49

5	Observations and modelling of a storm in strong vertical wind shear	53
5.1	Synoptic-scale introduction	54
5.2	Analysis of the observations	55
5.3	Numerical simulation of the 28 July 2005 case with the COSMO model . . .	66
5.3.1	Model description and setup	67
5.3.2	Results	71
5.3.3	Forcing terms in the perturbation pressure equation	77
6	Relevance of the results to severe weather threat	79
7	Summary and conclusions	84

Chapter 1

Introduction

The topic of this work is the dynamics of deep, moist convection in the earth's atmosphere, with special focus on the aspects that could render the convective storms *severe*. Severe storms are accompanied by extreme rainfall, severe wind gusts, tornadoes, large hail, and frequent lightning. Across the world and within Europe, such events produce significant damage and lead to dozens of fatalities every year (ESSL, 2009; Dotzek et al., 2009). Forecasting such events in a timely manner can considerably reduce the number of victims they cause, but that requires sound knowledge of the processes occurring in such storms. This knowledge is essential for developers of numerical models who need to verify their model's predictions against reality, and who need to devise realistic parameterizations for processes on scales too small for their model to resolve. Additionally, it is important that weather forecasters know how to interpret the output of the model they use in an operational setting. An example where forecasting has been successful is the success of tornado forecasting in the United States. Since tornado forecasting started in the 1950's, the number of (avoidable) tornado fatalities has dropped by about a factor of 10 relative to the (nearly unavoidable) wealth-adjusted damage that they cause (Brooks and Doswell, 2001).

The difficulty of forecasting such events is ultimately due to their relatively small scale and the non-linearity of the physics by which they are produced. This work deals with three aspects of severe convective storms. The first is the definition of the actual physical instability that produces them. In Chapter 2, a comparison will be made between the several concepts used in the meteorological literature, and it will be pointed out that one particular concept, that of *latent instability*, is the best concept for use in the forecasting of atmospheric convection. The chapter also briefly addresses the variability of thermodynamic parameters relevant to atmospheric convection.

The second aspect of storms that is discussed is that of *convective storm initiation*, i.e. the question where and when convective storms develop. This is a topic of intensive research by several groups of scientists who have recognized that numerical atmospheric models, that are intensively used for weather forecasts, have great difficulty simulating convective storm initiation. A number of field campaigns have recently been carried out to collect data to study the convective initiation process. Among them are IHOP_2002 (*International H₂O Project*) (Weckwerth et al., 2004) in the United States, CSIP (*Convective Storm Initiation Project*) (Browning et al., 2007) in southern England, PRINCE (*Prediction, identification and tracking of convective cells*) (Groenemeijer et al., 2009) in southwest Germany's

northern Black Forest, and COPS (*Convective and Orographically-induced Precipitation Study*) (Wulfmeyer et al., 2008; Kottmeier et al., 2008) in southwest Germany and eastern France. Until recently, numerical models used in operational weather forecasting could not resolve atmospheric convection explicitly. Although this has become possible in recent years through an increase in computational power, this has had little effect on the quality of quantitative precipitation forecasts (QPF) (Hense et al., 2003) for which, among others, nonlinear aspects of the moist dynamics on the convective scale appear to be responsible (Walser et al., 2004). One non-linear effect is storm initiation that is forced by the effects of an earlier storm, or *secondary initiation*. Chapter 3 of this work includes a case study of the influence of a storm upon its near environment and its consequences for subsequent *secondary initiation*. The case study uses data collected during the short but intensive PRINCE field campaign, and includes data collected using a wind lidar, a radar, radiosondes, and with airborne measurements.

The third aspect of convective storms dealt with here, is their evolution after initiation. In Chapter 3, it is shown how compensating subsidence, caused by an earlier storm system, can suppress the initiation of new storms. The reasons for the formation of the subsidence will be discussed. Storm evolution strongly depends on the vertical distributions of wind, temperature, and moisture in the storm's environment. The ratio of the resulting instability to the squared magnitude of vertical wind shear, a Bulk Richardson Number, is a particularly important metric in this respect. Wind shear strongly influences the location and intensity of pressure perturbations around an initial storm, and induce generation of secondary updraughts along the storm's periphery. If the formation of new updraughts is continuously forced on a particular flank of the storm system, a long-lived convective system may evolve with an enhanced potential of producing hazardous weather.

Based on a review of relevant literature, Chapter 4 introduces a theoretical framework for understanding the effects of wind shear on pressure perturbations. In Chapter 5, a case study of a strongly sheared storm that occurred during the CSIP field campaign is presented. In this particular case, a small but well-organized storm occurred that produced a tornado in downtown Birmingham. Based on surface observations, radar and visible satellite imagery, an analysis is presented of the environment in which the storm developed. Additionally, numerical simulations using the COSMO model (*Consortium for Small-scale Modeling*) (Schättler et al., 2007) will be discussed. These were successful in initiating a storm with characteristics similar to the one that was observed. Analysis of the data shows that the simulated storm also exhibited a rotating updraught caused by the tilting of horizontal vorticity into the storm's updraught. It is shown that the particular configuration of the storm was associated with its interaction with strong vertical wind shear. Moreover, it is demonstrated that the existence of a narrow band of high moisture in the boundary layer and strong low-level wind shear were crucial to the development of this storm into one capable of producing a strong tornado. Chapter 6 discusses the relevance of the results to severe weather forecasting by addressing the relation between wind shear and storm severity. Finally, Chapter 7 summarizes the conclusions of this work.

Chapter 2

Convective instability

Strong vertical movements of air in the atmosphere often directly result from density differences: less dense air moves upward while denser air moves downward. Such motions are called *free gravitational convection*. This type of flow may, or may not have, characteristics of a true *convective flow instability*: an initially small flow perturbation that grows over time by positive feedback on itself. A true flow instability develops for example when an air parcel, after being pushed away slightly from its initial position, experiences a force pushing it away even further. This force gets stronger the further the parcel moves away from its initial position. Such situations are common in the atmosphere. However, convection does not always have to involve an instability. An example of this is a situation in which two air masses with different densities are located next to each other. A direct circulation will develop with a downward branch in the denser air, and an upward branch in the warmer air, but this situation does not necessarily involve any positive feedback. By some definitions, e.g. that of the Glossary of Meteorology (Glickman, 2000), this phenomenon must be considered free convection as well. The opposite of free convection is *forced convection*. In that case, motions occur to which density differences do not contribute, or which are even counteracted by such differences. Besides free gravitational convection that is forced purely by density differences, there is *slantwise convection*. Slantwise convection is caused by a combination of density differences and a marginally stable distribution of horizontal geostrophic momentum (Schultz et al., 2000). This type of convection will not be discussed here. Rather, the focus will be mostly on free convection, more precisely on the type that involves an instability.

In meteorology, the term instability is usually preceded by adjectives like *potential*, *conditional*, or *latent*. Such concepts refer to a vertical distribution of temperature and moisture that under certain conditions supports a true flow instability. They will be discussed here, because they are a common source of confusion and, even within the scientific literature, names are used loosely for different types of instability.

In order to assess whether gravitational instability may ensue, and how intense it may become, a plethora of methods has been proposed in the meteorological literature. Most methods are based upon a single vertical profile of temperature and moisture in (what is assumed to be) an unperturbed environment in which convection is not yet occurring. Such profiles are traditionally obtained by radiosondes that, being attached to a balloon, rise through the atmosphere and transmit measured temperature, moisture and pressure

data to a receiving station on the ground. The discussion of instabilities will be started by considering the vertical profiles of temperature and moisture that may be retrieved this way. In order to accustom the reader to appreciating the differences between the various types of instabilities, their discussion will start off from a fairly basic level.

2.1 One-dimensional assessments of instability

2.1.1 Absolute instability

The most basic measure of instability is the vertical derivative of temperature, or *lapse rate*. Air parcels in which no phase changes of the contained water vapour occur, and in which heat exchange with their environment can be neglected (i.e. the adiabatic assumption is made), have a nearly constant warming and cooling rate with altitude during vertical displacements in the middle and lower parts of the earth's atmosphere. For air parcels that do not contain water vapour at all, this is called the *dry-adiabatic lapse rate* Γ_d . If the air contains water vapour that does not condense, its lapse rate is close to the dry-adiabatic lapse rate. The lapse rate of a parcel's environment is a measure of stability: if an air parcel cools less rapidly with increasing altitude than its environment, an upward (downward) displacement would render it warmer (colder) than its environment and, hence, less dense (denser). As a result, it would accelerate even further from its initial position, which constitutes a flow instability.

The dry-adiabatic lapse rate Γ_d for dry air can be derived from the adiabatic form of the first law of thermodynamics and the hydrostatic equation, which yields¹

$$\Gamma_d = \frac{dT}{dz} = -\frac{g}{c_p} \approx -9.8 \times 10^{-3} \text{ Km}^{-1} \quad (2.1)$$

Here, T is temperature, z the vertical ordinate, g the acceleration of gravity, and c_p the specific heat of dry air at constant pressure. Layers of air with a steeper lapse rate than this (i.e. a stronger decrease of temperature with height) are said to be *absolutely unstable*. Such layers do normally not exist for a long time, because convection will immediately ensue within the layer and reduce the lapse rate to the dry-adiabatic lapse rate. A situation of (slight) absolute instability can persist only where a continuous source of diabatic heating is present at the bottom of the layer, or a source of diabatic cooling at its top. Typically, heating occurs at the ground-air interface in the case of strong solar radiation, and cooling may occur at the top of clouds. In that case, the absolute instability is generated at approximately the same rate at which it is consumed.

One can derive a quantity that is conserved during a dry-adiabatic process by defining the temperature that it would have at some standard pressure level p_0 . This can be done by integrating the thermodynamic equation from any pressure p to the standard pressure p_0 , usually 10^5 Pa, and from any temperature $T(p)$ to the temperature this air would obtain at p_0 , which is called the *potential temperature* θ . The following expression for θ then results

¹The expression can be adjusted so that it expresses the dry-adiabatic lapse rate for a mixture of dry air and water vapour. It then reads $\Gamma_d = -(g/c_p)(1 + r_t)/(1 + r(c_p/c_{pv}))$. There, r is the water vapour mixing ratio and c_{pv} is the specific heat of water vapour.

$$\theta = T \left(\frac{p_0}{p} \right)^{\frac{R_d}{c_p}} \quad (2.2)$$

Here, R_d is the specific gas constant for dry air. Because there is, per definition, no heat exchange in a dry-adiabatic process, and the entropy change δS of a system is given by $\delta S = \delta Q/T$, an adiabatic process is also an isentropic process. Hence, lines of equal potential temperature can be called either *dry-adiabats* or *isentropes*.

2.1.2 Conditional instability

In any parcel that is saturated, condensation of water vapour will occur when it cools due to adiabatic expansion. The latent heat of condensation reduces its rate of cooling with increasing altitude compared to the dry-adiabatic lapse rate. Instead, the temperature of the parcel will follow a *moist-adiabatic lapse rate* Γ_m , which typically lies between -9×10^{-3} and $-4 \times 10^{-3} \text{ Km}^{-1}$. Using the Clausius-Clapeyron equation, which expresses the saturation vapour pressure as a function of temperature, an expression for the moist-adiabatic lapse rate can be derived. A version that includes liquid water contained within the parcel is (from Glickman, 2000):

$$\Gamma_m = g(1 + r + r_l) \frac{1 + L_v r / R_d T}{c_p + r c_{pv} + r_l c_l + L_v^2 r (\epsilon + r) / R_d T^2} \quad (2.3)$$

In this expression r is the water vapour mixing ratio, r_l is the liquid water mixing ratio, L_v is the latent heat of vaporization, c_l is the specific heat of liquid water, c_{pv} is the specific heat of water vapour, R_v is the gas constant for water vapour, and $\epsilon = R_d / R_v = 0.6220$. For this calculation of Γ_m , condensed water is assumed to remain inside the parcel. However, one can also assume that the condensed water falls out of the parcel, which means that during ascent, the latent heat of condensation will contribute to the warming of the air in the parcel, but not to the warming of water that condensed earlier. That assumption results in a lapse rate that is slightly less steep, the *pseudo-adiabatic lapse rate*. The difference between moist-adiabatic and pseudo-adiabatic ascent is small in the lower and mid-troposphere. Additionally, there are formulations that incorporate the latent heat of freezing of the condensate in the lapse rate (Manzato and Morgan, 2003). Because it is usually not possible to estimate where the freezing will occur, as this depends on often unknown microphysical parameters, such refinements have little value for most case studies.

When the lapse rate of a layer is between the moist and dry-adiabatic lapse rates an instability only exists when the air is saturated. This situation is therefore called *conditional instability*. Conditionally unstable layers, with depths on the order of a few kilometres, are relatively common. However they are not commonly saturated, because this would, per definition, lead to convective overturning destroying the steep lapse rates.

An analogue to the potential temperature can be defined for a moist-adiabatic process, and is called the *equivalent potential temperature* θ_e . Ignoring the heat capacity of hydrometeors, it can be expressed as

$$\theta_e = \theta \exp \left(\frac{L_v r}{c_p T} \right) H^{-\frac{r R_v}{c_p}} \quad (2.4)$$

Herein H is the relative humidity. A derived quantity that will be used below, is the *saturation equivalent potential temperature*, θ_{es} . It is the θ_e that the air would have in the hypothetical case that it would be saturated with water vapour, i.e. $r = r_{sat}$.

$$\theta_{es} = \theta \exp\left(\frac{L_v r_{sat}}{c_p T}\right) \quad (2.5)$$

Conditional instability can be expressed as the condition that $\partial\theta_{es}/\partial z < 0$ across some layer of air.

2.1.3 Potential instability

A layer in which θ_e decreases with altitude is said to contain *potential instability*. A true flow instability can develop in such a layer when the bottom of the layer becomes saturated during ascent and the lapse rate within the layer becomes steeper than moist adiabatic. However, potential instability may also exist in a layer that is stabler than moist-adiabatic, if the moisture content reduces rapidly with altitude. In that case, the amount of lifting required to let a flow instability develop in the layer, may be unrealistically large. A more fundamental problem though, is that for potential instability to be released, saturation must first occur. Schultz et al. (2000) have noted that "*this layer-lifting process, however, is not typically associated with the development of isolated upright deep moist convection. If it were, layer lifting initially would produce stable stratiform clouds, which would then develop into deep moist convection.*" Because it is not observed that stratiform cloudiness develops before deep convection breaks out, except perhaps in the vicinity of some convective frontal systems, this type of instability is clearly not appropriate for most convective storms. These properties render potential instability a very difficult concept to work with in practice. Nevertheless, it is frequently used in thunderstorm forecasting across Europe, for example in the form of the "KO-index", which is a measure of potential instability. This is surprising as various studies have found that the KO-index does not belong to the best predictors of thunderstorms (Huntrieser et al., 1997; Haklander and Van Delden, 2003; Kunz, 2007). As will be demonstrated, the more restricted condition of *latent instability* will be fulfilled before the actual flow instability develops. All of the cited studies show that parameters based on this concept perform better as thunderstorm predictors.

2.1.4 Thermal buoyancy and latent instability

An interesting situation occurs when a parcel of saturated air penetrates into air with a conditionally unstable stratification. In that case, an upward displacement of the parcel could make the parcel warmer than its environment, either directly, or after some finite displacement (given that the conditionally unstable layer is sufficiently deep). That would make the parcel less dense, and therefore, positively buoyant. When that happens, a flow instability develops. The combination of (i.) a conditionally unstable layer and (ii.) the presence of an air parcel that can become positively buoyant within that layer after an upward displacement, has been coined *latent instability* by Normand (1938). It is sometimes also called *convective instability*. Some even call it potential instability, which naturally causes confusion.

In order to assess the presence of latent instability, one should look whether a parcel of air at some height in the troposphere obtains positive *thermal buoyancy* after being lifted. Thermal buoyancy is a quantity that expresses the vertical volume force on a parcel due to the different density that it has, compared with its environment. The vertical momentum equations can be rewritten in such a way that thermal buoyancy appears explicitly as an individual term.

The momentum equation, neglecting friction and the earth's rotation may be written in vector form as:

$$\frac{\partial \mathbf{v}}{\partial t} + \mathbf{v} \cdot \nabla \mathbf{v} = -\frac{1}{\rho} \nabla p - g \hat{\mathbf{k}} \quad (2.6)$$

Its vertical component is

$$\frac{\partial w}{\partial t} + \mathbf{v} \cdot \nabla w = -\frac{1}{\rho} \frac{\partial p}{\partial z} - g \quad (2.7)$$

In these equations \mathbf{v} is the velocity vector and w its vertical component, ρ is density and p is pressure. For convenience, the term on the left hand side are now condensed into a material derivative, and the equation is multiplied by density, yielding

$$\rho \frac{dw}{dt} = -\frac{\partial p}{\partial z} - \rho g \quad (2.8)$$

Now, perturbations on a hydrostatically-balanced horizontally homogeneous base state will be considered, i.e. a base state in which the terms on the right-hand side of the above equation cancel each other. The hydrostatic pressure and density are denoted with an overbar, and perturbations on this state are primed. Thus, we have $p = \bar{p}(z) + p'(x, y, z, t)$ and $\rho = \bar{\rho}(z) + \rho'(x, y, z, t)$, and $\frac{\partial \bar{p}}{\partial z} = -\bar{\rho}g$. Here \bar{p} will be called the *base-state pressure*, and p' the *perturbation pressure*. Substituting this into the vertical momentum equation gives

$$\rho \frac{dw}{dt} = -\frac{\partial \bar{p}}{\partial z} - \frac{\partial p'}{\partial z} - \bar{\rho}g - \rho'g \quad (2.9)$$

By the definition of the hydrostatic equilibrium, the first and third terms on the right-hand side cancel, which yields

$$\rho \frac{dw}{dt} = -\frac{\partial p'}{\partial z} - \rho'g \quad (2.10)$$

Dividing by ρ gives

$$\frac{dw}{dt} = -\frac{1}{\rho} \frac{\partial p'}{\partial z} - \frac{\rho'}{\rho} g = -\frac{1}{\rho} \frac{\partial p'}{\partial z} + B_T \quad (2.11)$$

Here, the term $B_T = -(\rho'/\rho)g$ is called *thermal buoyancy* or *Archimedean buoyancy*. Whenever a parcel is less dense (denser) than the hydrostatic base state, this term creates an upward (downward) acceleration. Using scaling arguments, it can be shown that for speeds much lower than the speed of sound, temperature fluctuations are the main contributors to density fluctuations in a fluid, rather than pressure fluctuations², so that

²See Emanuel (1994) p. 6–8 for a discussion.

$\rho'/\rho \approx -T'/T$, and $B_T \approx (T'/T)g$, which explains why this is called thermal buoyancy. In the case of air, however, an additional complication occurs, in that it cannot always be assumed that the mixture of atmospheric gases is constant. Although most gases are distributed rather evenly in the troposphere, fluctuations in water vapour concentration are common. Convective updraughts, for example, contain more water vapour than their direct environment. As this affects the density of air, this effect needs to be incorporated into the equations. To that aim, it is customary to use the quantity of *virtual temperature* T_v , which represents the temperature that dry air would need to have in order to be as dense as the dry air/water vapour mixture. An approximate formula for the virtual temperature is $T_v = T(1 + 0.608r)$, where r is the water vapour to dry air mixing ratio. Thus, thermal buoyancy can be expressed as

$$B_T \approx \frac{T'_v}{T_v}g \quad (2.12)$$

The complete three-dimensional momentum equation then becomes

$$\frac{\partial \mathbf{v}}{\partial t} + \mathbf{v} \cdot \nabla \mathbf{v} = -\frac{1}{\rho} \nabla p' + B_T \hat{\mathbf{k}} \quad (2.13)$$

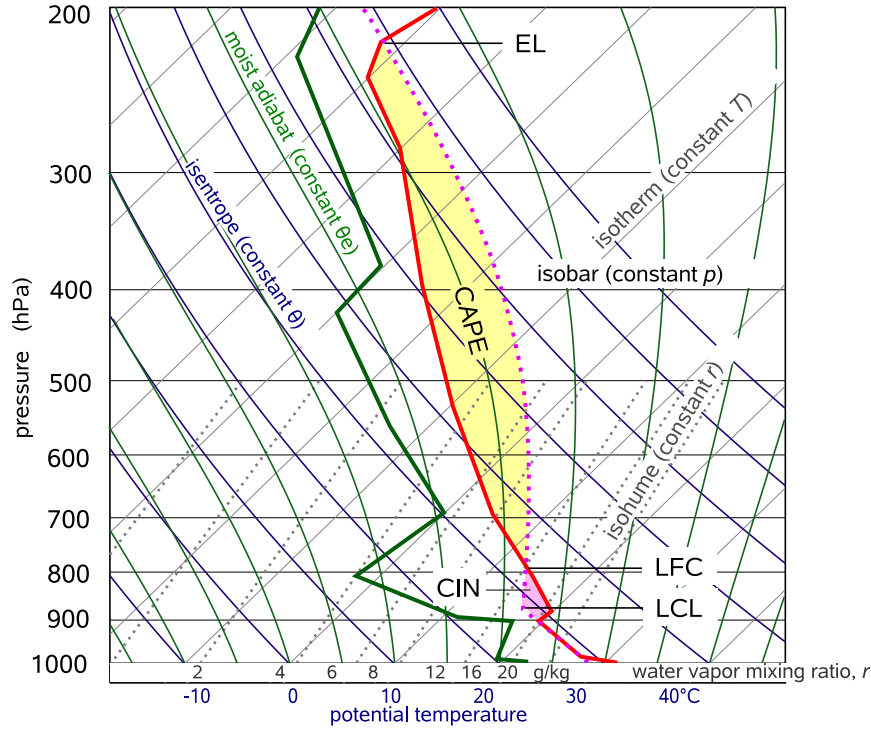


Figure 2.1: Skew- T log p diagram showing a temperature and humidity profile that may be preceding the development of deep, moist convection. An ascent curve is constructed for a parcel having the average properties of the air in the lowest 100 hPa. The parcel follows a dry adiabat along which θ is conserved up to the lifted condensation level (LCL) where condensation commences. Above the LCL, θ_e and θ_w are conserved and the parcel will cool less with height due to the release of latent heat of condensation. The abbreviations in the diagram are explained in the text.

To find out whether a parcel can become buoyant, a thermodynamic diagram can be used. An example is the Skew- T -log- p diagram displayed in Fig. 2.1. The diagram has

horizontal isobars, spaced at equal increments of $\log(p)$, so that the vertical ordinate is roughly proportional to height. Isotherms are lines that – instead of vertical lines used in other diagrams – have been skewed to the right with decreasing pressure. This is to make sure that a troposphere with a typical stratification appears more or less in the centre of the diagram, rather than slope steeply to the left. The diagram shows dry adiabats (blue), or lines of equal potential temperature sloping upward to the left, and moist pseudo-adiabats, i.e. lines of equal equivalent potential temperature, in green. Isohumes, or lines of equal mixing ratio, are plotted as dotted lines up to the 500 hPa isobar. Profiles of temperature and dew point temperature as they could be found in a typical situation of deep, moist convection are plotted as thick red and green lines, respectively.

The temperature and water vapour mixing ratio of an air parcel that rises upward from the earth's surface, starting with an initial temperature and moisture content, can be calculated numerically for each altitude. If the distribution of temperature and water vapour of its environment are known, the parcel's thermal buoyancy can be calculated. In the approach that follows, which is commonly referred to as *parcel theory*, the perturbation pressure force (the first term on the right-hand side in Eq. 2.11), is ignored. The consequences of this will be discussed.

The thermal buoyancy, being a volume force, can be integrated over the distance over which it acts, so that the work done by this force is known. This work can be thought of as being equal to an amount of released potential energy, which is called convective potential available energy (CAPE). CAPE is usually defined as the work done from the point at which a parcel first obtains positive thermal buoyancy, called the *level of free convection (LFC)*, to that where the parcel's buoyancy vanishes, the *equilibrium level (EL)*:

$$CAPE = \int_{LFC}^{EL} B_T dz = \int_{LFC}^{EL} g \frac{T'_v}{T_v} dz. \quad (2.14)$$

In addition to CAPE, another energy can be defined, namely that, which needs to be overcome by an air parcel to reach its level of free convection. This is called *convective inhibition (CIN)*, which is defined as

$$CIN = - \int_{z_0}^{LFC} B_T dz = - \int_{z_0}^{LFC} g \frac{T'_v}{T_v} dz. \quad (2.15)$$

Here, z_0 is the initial height from which the parcel starts its ascent. It is recommended that this altitude is taken to be above a shallow surface layer in which strong vertical gradients of temperature and moisture commonly occur. Both CAPE and CIN can be visualised graphically on a thermodynamic diagram as areas enclosed by the calculated parcel temperature and the environmental temperature. In Fig. 2.1, CAPE and CIN are represented by the yellow and pink areas. The surface areas are proportional to the magnitude of CAPE and CIN, respectively.

2.1.5 Comparison of different instability concepts

The instability concepts that were discussed are summarized in Table 2.1. Comparing the several criteria, the question which of them is the most useful for forecasting convec-

tive storms arises naturally. To answer this question, each of the concepts will now be considered.

	definition	requirement to obtain a real instability
absolute instability	$\frac{\partial\theta}{\partial z} < 0$, or $\frac{\partial T}{\partial z} < \Gamma_d$	none
conditional instability	$\frac{\partial T}{\partial z} < \Gamma_m$, or $\frac{\partial\theta_{es}}{\partial z} < 0$, the condition for absolute instability must not be fulfilled	the air must be saturated
potential instability	$\frac{\partial\theta_e}{\partial z} < 0$	the layer must be lifted to saturation
latent instability	there is a parcel that becomes positively buoyant after being lifted (or equivalently, for which $CAPE > 0$)	a parcel must reach its LFC

Table 2.1: The definitions of four commonly used concepts of instability, and the additional condition required to obtain a flow instability from it. The condition that a small perturbation of vertical velocity be present is required for all four instabilities, and omitted from the table for the sake of brevity.

To begin with, absolute instability does not take into account phase changes of water. As these are obviously relevant to deep, moist convection, absolute instability clearly cannot be the most useful for forecasting convective storms. The other three concepts, however, require more careful scrutiny. A key point is that free convection always involves thermal buoyancy (except in the extended definition of Glickman (2000), referred to in this chapter's introductory paragraph), and only one of the three instability concepts explicitly refers to thermal buoyancy, namely *latent* instability. In contrast, the presence of conditional and potential instability does not necessarily mean that there is a parcel that can become buoyant after a hypothetical vertical displacement. In other words, latent instability is the most strict precondition of the three. It will now be shown that if latent instability exists, both potential and conditional instability must exist as well, but conversely the presence of either potential or conditional instability does not guarantee the presence of latent instability.

Potential instability is present if and only if somewhere in the profile $\frac{\partial\theta_e}{\partial z} < 0$. This implies that there must be a level z_A and a level z_B ($z_A < z_B$), for which $\theta_e(z_A) > \theta_e(z_B)$.

Latent instability is present if and only if in a vertical profile of the atmosphere, a height level z_A and a level z_B ($z_A < z_B$) can be found, for which $\theta_e(z_A) > \theta_{es}(z_B)$. Because $\theta_e \leq \theta_{es}$, if for the two levels z_A and z_B , $\theta_e(z_A) > \theta_{es}(z_B)$ is valid (i.e. there is latent instability), $\theta_e(z_A) > \theta_e(z_B)$ must hold as well (i.e. there is potential instability). The converse, however, may or may not hold: if $\theta_e(z_A) > \theta_e(z_B)$, it is not generally true that $\theta_e(z_A) > \theta_{es}(z_B)$.

Conditional instability is present if and only if $\frac{\partial T}{\partial z} < \Gamma_m$, or alternatively $\frac{\partial\theta_{es}}{\partial z} < 0$. This implies that there must be a lower level z_A and a higher level z_B , for which $\theta_{es}(z_A) >$

$\theta_{es}(z_B)$. Because $\theta_e \leq \theta_{es}$, if for the two levels z_A and z_B , $\theta_e(z_A) > \theta_{es}(z_B)$ is valid (i.e. there is latent instability), $\theta_{es}(z_A) > \theta_{es}(z_B)$ must hold as well (i.e. there is conditional instability). The converse, however, may or may not hold: if $\theta_{es}(z_A) > \theta_{es}(z_B)$, it is not generally true that $\theta_e(z_A) > \theta_{es}(z_B)$.

It is a tempting hypothesis that the set of all profiles that feature latent instability equals the intersection of those that feature potential instability and those that feature conditional instability. This is easily disproved by finding an example exhibiting potential and conditional instability but not latent instability. It turns out that such an example is easy to find, and that the hypothesis does not hold. To summarize, Fig. 2.2 shows how the sets of profiles that feature the respective types of instability, intersect.

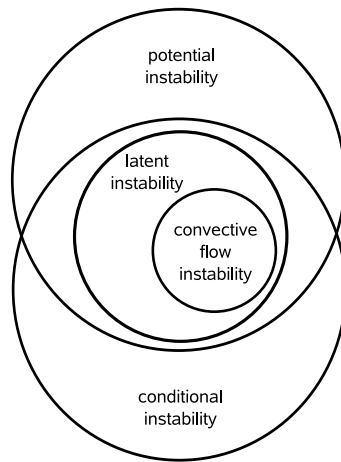


Figure 2.2: Euler diagram, showing several instability concepts.

It can be seen that the most strict precondition for deep, moist convection is latent instability, although even that is not a guarantee to obtain a true flow instability: parcel theory predicts that given the presence of latent instability, no convection will ensue when CIN cannot be overcome by an initial amount of upward motion of the parcel

Even when CIN is absent, deep, moist convection does not necessarily ensue. There are several possible explanations for this, most of which lie outside the realm of parcel theory. A very important one is that realistic convective bubbles are not isolated from their environment, so the adiabatic assumption, that forms the basis of parcel theory, does not hold. Entrainment of drier and/or cooler air into such a bubble can drastically lower its net thermal buoyancy, and ultimately dissolve it. An interesting method for predicting convective initiation that takes this effect into account was proposed by Houston and Niyogi (2007). They consider the effects of mixing between a parcel and its environment on a parcel's buoyancy, which, so the authors argue, would be related to the lapse rate within the zone in which the cloud develops.

2.2 Variability of thermodynamic parameters

Apart from the limitations of parcel theory, the problem of convective initiation is already greatly complicated by the tendency of humidity and temperature to vary on very small

scales. Especially within the planetary boundary layer, such variations tend to develop in response to solar heating. Such variations usually cannot be resolved but by aircraft measurements and state-of-the-art remote sensing devices such as lidars and sodars.

When a certain amount of vertical shear of the horizontal wind is present across the depth of a heated boundary layer, so-called *horizontal convective rolls* or *boundary-layer rolls* will develop (e.g. Asai, 1970; LeMone, 1973; Etling and Brown, 1993; Hartmann et al., 1997). The updraught zones of such rolls are usually visible in visible satellite imagery as streets of convective clouds, that are more or less aligned with the mean wind in the boundary layer. Within such rolls, both moisture and temperature may vary considerably. When calculating parameters like CAPE and CIN from such parameters, this variability introduces very large differences between the air originating from the upward and downward branches of the rolls, as has been demonstrated by Weckwerth et al. (1996), who studied boundary-layer rolls across the Florida peninsula.

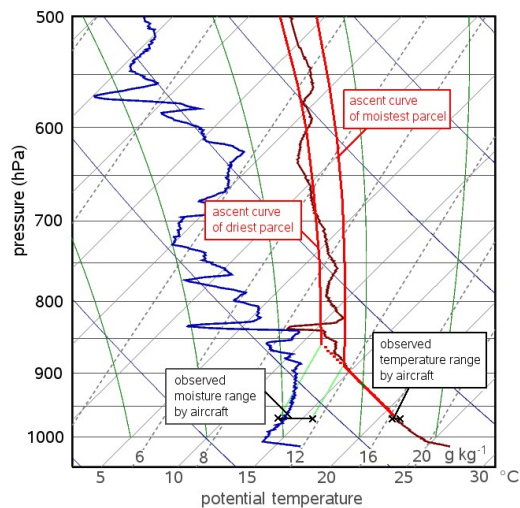


Figure 2.3: Skew-T-log-p thermodynamic diagram showing profiles of temperature (dark red) and moisture (blue) at Chilbolton (U.K.) on 13th July 2005 at 1156 UTC and the range of moisture and temperature values observed by the Do 128 research aircraft, within approximately 30 minutes of the sounding time, and within 50 km of the sounding location. The ascent curves of the driest and the moistest parcel, both for an average temperature, are drawn in red.

An example of a situation of when such differences are significant, will now be shown. The temperature and moisture profiles measured with a radiosonde near the town of Chilbolton at 1156 UTC³ on 13 July 2005 up to the 650 hPa level are shown in Tab. 2.3. Additionally, values of temperature measured with a research aircraft (a Dornier Do 128, see section Tab. 3.3 for a description) are plotted in black. The aircraft was flying at a constant altitude corresponding to a pressure level of 969 hPa (approximately 400 m AGL) and within 50 km of the location of the displayed radiosonde ascent between 1130 and 1230 UTC.

Scrutinizing the profiles, one can detect a rather well-mixed boundary layer with a near dry-adiabatic temperature profile, and little change in mixing ratio in the layer between 1005 and 880 hPa. In the lowest 5 to 10 hPa, a super-adiabatic temperature profile and a very shallow moist layer can be seen. Both are typical of a situation in which strong

³local time = UTC + 1 hour

sensible and latent heat fluxes occur in the surface layer due to solar heating. Above the well-mixed layer, the temperature lapse rate becomes weaker and several moister and drier layers can be seen. The dip in temperature near 835 hPa is thought to be an artifact of the sensor that may have briefly penetrated a cloud.

It can be seen that the aircraft has measured slight temperature variations. The temperature varied only by 0.6 °C whereas the dew point temperature varied between 13.6 and 15.8 °C (or, expressed in mixing ratios, 9.5–10.9 g kg⁻¹). The temperature variations are similar to those found by Weckwerth et al. (1996) in a convective boundary layer in Florida, namely slightly larger moisture variations of 1.5–2.5 g kg⁻¹. The moisture variations are similar in magnitude to those reported by Couvreux et al. (2005) for measurements in northeast Oklahoma.

The CAPE values for the parcels with the lowest and highest equivalent potential temperature θ_e were 79 J kg⁻¹ and 740 J kg⁻¹, respectively. This shows how large variations in CAPE can be due to low-level variations in moisture, and, to a lesser extent, due to variations in temperature. The CIN values associated with these parcels are not very trustworthy because of the unphysical temperature dip around 835 hPa, but it can be seen that the temperature of the most unstable parcel (the right dashed line) was almost nowhere colder than its environment, resulting in negligible CIN. The other parcel, however, was colder than its environment in the 870–700 hPa interval. Thus considerable CIN existed for this parcel⁴.

It has been shown that relatively small fluctuations in temperature and humidity of a boundary-layer parcel have large implications for both the CIN and CAPE. When trying to quantify the effect of boundary-layer moisture and temperature fluctuations on the temperature of a parcel after being lifted, it becomes clear that a 1°C increase in parcel temperature near the surface does not imply a 1°C increase in parcel temperature at higher tropospheric levels.

	1 g kg ⁻¹	2 g kg ⁻¹	4 g kg ⁻¹	7 g kg ⁻¹	10 g kg ⁻¹	16 g kg ⁻¹	24 g kg ⁻¹
0°C	0.80	0.79					
5°C	0.77	0.75	0.73				
10°C	<i>0.90</i>	0.90	0.68	0.63			
15°C	<i>0.90</i>	<i>0.90</i>	0.64	0.59	0.54		
20°C	<i>0.90</i>	<i>0.90</i>	0.60	0.55	0.51		
25°C	<i>0.90</i>	<i>0.90</i>	<i>0.91</i>	0.51	0.47	0.41	
30°C	<i>0.90</i>	<i>0.90</i>	<i>0.91</i>	0.48	0.44	0.38	0.33
35°C	<i>0.90</i>	<i>0.90</i>	<i>0.91</i>	<i>0.91</i>	0.41	0.36	0.31

Table 2.2: Increase in parcel virtual temperature at 700 hPa (°C) in response to a 1 °C increase of its temperature at 1000 hPa. Italic numbers denote where no condensation has yet occurred in the parcel.

The virtual temperature increase of parcels at 700 hPa in response to a 1°C increase at 1000 hPa is listed in Tab. 2.2. The level of 700 hPa is chosen because it is a typical pressure level where convective inhibition occurs. If no condensation occurs in the parcel,

⁴This cannot be determined precisely by comparing the parcel's temperature with that of its environment. Instead *virtual temperature* must be compared. This comparison also shows that CIN was present. An exact value can however not be given because of the measurement error near 835 hPa.

	1 g kg ⁻¹	2 g kg ⁻¹	4 g kg ⁻¹	7 g kg ⁻¹	10 g kg ⁻¹	16 g kg ⁻¹	24 g kg ⁻¹
0°C	2.02	1.93					
5°C	1.97	1.87	1.74				
10°C	<i>0.16</i>	1.80	1.67	1.50			
15°C	<i>0.16</i>	1.73	1.59	1.42	1.29		
20°C	<i>0.16</i>	<i>0.16</i>	1.50	1.35	1.22		
25°C	<i>0.16</i>	<i>0.16</i>	<i>0.16</i>	1.27	1.15	0.97	
30°C	<i>0.17</i>	<i>0.17</i>	<i>0.17</i>	1.21	1.10	0.93	0.78
35°C	<i>0.17</i>	<i>0.17</i>	<i>0.17</i>	<i>0.17</i>	1.04	0.89	0.75

Table 2.3: Increase in parcel virtual temperature at 700 hPa (°C) in response to a 1 g kg⁻¹ increase of its water vapour mixing ratio at 1000 hPa. Italic numbers denote where no condensation has yet occurred in the parcel.

the virtual temperature change at 700 hPa is nearly proportional to the initial temperature change at 1000 hPa. In that case, if the parcel warms by 1°C at 1000 hPa, its temperature at 700 hPa will always increase by about 0.9°C. But if condensation occurs below 700 hPa, which is often the case in the real atmosphere, its temperature at 700 hPa increases much less than its initial temperature increase at 1000 hPa. This can be understood by realizing that for an increase in temperature, a parcel's lifted condensation level increases, so that a smaller fraction of latent heat is released below the fixed pressure level. Especially at higher temperatures, a parcel's temperature in the mid-troposphere is so strongly influenced by latent heating, that temperature variations have a relatively small effect on its ultimate temperature. An increase of 1°C in a parcel's temperature at 1000 hPa, an initial temperature near 35°C, and sufficient moisture for condensation to occur below the 700 hPa level, results in a virtual temperature increase of only 0.3–0.4°C at 700 hPa.

An increase in moisture at 1000 hPa naturally results in an increase in parcel virtual temperature at 700 hPa. These values are shown in Tab. 2.3. For those values where no condensation occurs within the parcel, moisture still has an effect due to the increase in the parcel's virtual temperature. If condensation does occur, the amount of temperature increase is strongly dependent on the temperature and the amount of moisture already present. At low surface temperatures, around 0°C, a 1 g kg⁻¹ increase in water vapour mixing ratio results in an virtual temperature increase of the parcel at 700 hPa of about 2°C, whereas at temperatures over 30°C and moisture over 15 g kg⁻¹, this values dips below 1°C. To summarize the above, both low-level temperature and low-level moisture perturbations of certain magnitudes are much more significant to storm initiation when the overall temperature and moisture are low.

The ratio of the two effects is an interesting quantity as well. For all values of moisture and initial temperature that cause condensation within the parcel in Tab. 2.2 and Tab. 2.3, the ratio between the two effects is such that an increase of 1 g kg⁻¹ in moisture is approximately equal to a temperature increase of 2.5°C. In the case of the measurements above, the observed variability of moisture produces a 1.7°C variability in parcel virtual temperature at 700 hPa while the temperature variations produce a variability of only 0.3°C. It must be concluded that any fluctuations in boundary-layer moisture on this specific day were much more relevant to convective initiation than fluctuations in temperature. The same was found in the study in Florida by Weckwerth et al. (1996).

Not only boundary-layer variability of moisture and temperature influences the spatial distribution of CAPE and CIN. Mesoscale circulations associated with deep, moist convection can also influence the vertical profile of temperature on timescales of tens of minutes and spatial scales of tens of kilometres. An example from the CSIP field campaign is shown without presenting a complete analysis of the meteorological situation.

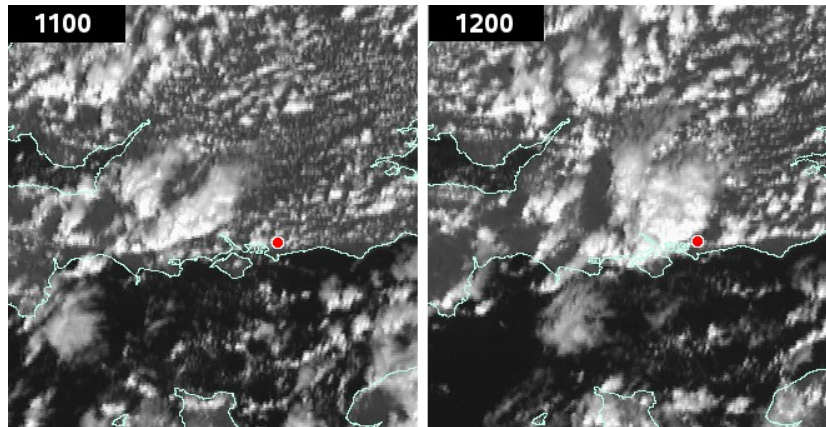


Figure 2.4: Meteosat satellite images (VIS) of the CSIP measurement area at 1100 UTC (left) and 1200 UTC (right) on 25 August 2005. Courtesy U.K. Met. Office/EUMETSAT.

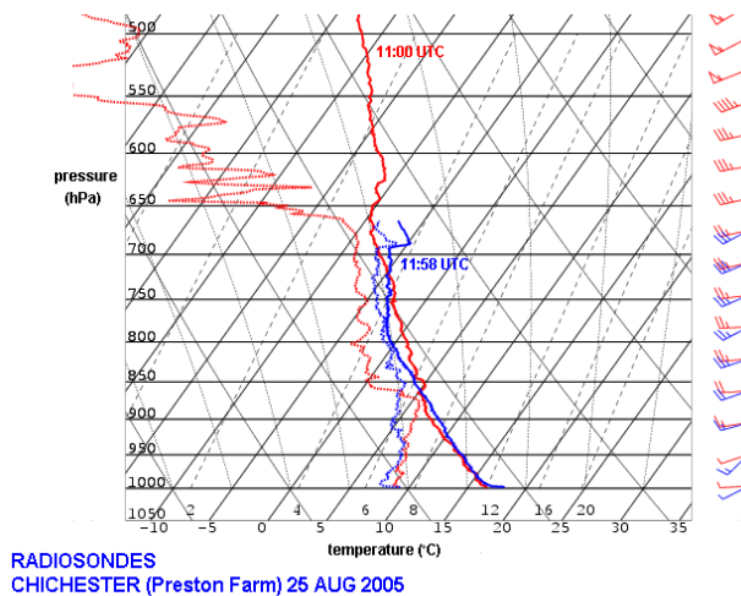


Figure 2.5: Skew-T-log-p thermodynamic diagram showing two soundings performed during CSIP at Preston Farm near Chichester. The location of the sounding site is indicated by a red dot in Fig. 2.4. The barbs are plotted according to the convention that half barbs represent 2.5 m s^{-1} and whole barbs 5 m s^{-1} .

Fig. 2.4 shows a pair of satellite images (VIS) from the Meteosat satellite at 1100 UTC (left) and 1200 UTC (right). The area shown is a part of southwestern England, with the English Channel in the south and the Bristol Channel in the west of the image. A linearly organized convective storm system is located near the centre of the images, which tracks east-southeastward. The storm system can be seen to approach the red dot, which

indicates a radiosonde site at Chichester. Two sondes that were released from this site at 1100 and 1158 UTC, approximately the times of the satellite images, are drawn in the Skew-T-log-p diagram of Fig. 2.5. Two changes between those two radiosonde profiles, i.e. in the hour before the approach of the storm system, are noteworthy. One can see that the layer between 870 hPa and 730 hPa has cooled rather strongly while it has moistened at the same time. A likely cause for this moistening is an area of upward vertical motion ahead of the convective line. Additionally, advection of cool air and moisture may have contributed. In any case, it is obvious that the steep, near dry-adiabatic lapse rates that at 1100 UTC extended from the surface upward to around 870 hPa extends upward to near 800 hPa at 1158 UTC. Within that hour, considerably more thermal buoyancy was created in the layers just above the boundary layer for a parcel rising from near the surface. The main point that is made here is that significant creation of CAPE can take place within an hour and within a zone of perhaps 20–30 km ahead of a convective system.

Chapter 3

Convection in weak vertical wind shear

3.1 Perturbation pressure and flow adjustment to thermal buoyancy

Until now, convective instability was discussed in terms of the thermal buoyancy of an imaginary parcel. This approach, which forms the basis of the quantities CAPE and CIN, has proven to be useful in forecasting practice, but it paints an incomplete picture of reality. Or, as Williams et al. (2005) put it, "Parcel theory is a great convenience, but it is also a widely recognized fiction". Parcel theory namely does not incorporate the effects of pressure perturbations on the storm¹. This is not surprising as it is per definition one-dimensional. In order to understand where pressure perturbations develop within a convective storms and which effects they can have, the inviscid, irrotational three-dimensional momentum equation (Eq. 2.13) can be used as a starting point:

$$\frac{\partial \mathbf{v}}{\partial t} + \mathbf{v} \cdot \nabla \mathbf{v} = -\frac{1}{\rho} \nabla p' + B_T \hat{\mathbf{k}} \quad (3.1)$$

The terms responsible for a parcel's acceleration on the right-hand side of this equation, are perturbation pressure gradient forces and buoyancy.

Following Holton (1992), Emanuel (1994) and Rotunno and Klemp (1982), the Boussinesq approximation will be used for a further development of this equation. The Boussinesq approximation makes the assumption that density variations may be ignored, except where they are coupled with gravity, i.e. in the thermal buoyancy term of the momentum equation. It may be argued that the Boussinesq approximation is not the most suitable for deep, atmospheric convection, because it requires the depth of the convection to be much smaller than the scale height of the atmosphere, which is on the order of 10 km. The aforementioned authors all report that the approximation is in order for a qualitative treatment of convective storms, or as formulated by Emanuel "I know of no case where applying it actually eliminates interesting processes or phenomena" (Emanuel, pers. communication.). Thus,

¹Moreover it does not account for entrainment or detrainment of air.

continuing the development, a constant value ρ_0 will be assumed where the density occurs in the denominator of the factor preceding the perturbation pressure gradient. Thereby the momentum equation becomes

$$\frac{\partial \mathbf{v}}{\partial t} + \mathbf{v} \cdot \nabla \mathbf{v} = -\frac{1}{\rho_0} \nabla p' + B_T \hat{\mathbf{k}} \quad (3.2)$$

Another aspect of the Boussinesq approximation is that the continuity equation reduces to

$$\nabla \cdot \mathbf{v} = 0 \quad (3.3)$$

Now, in order to get an idea about the origin of the perturbation pressure, we take the three-dimensional divergence, $\nabla \cdot = \left(\frac{\partial}{\partial x} + \frac{\partial}{\partial y} + \frac{\partial}{\partial z} \right) \cdot$, of Eq. 3.2. Using Eq. 3.3, considering the fact that $\nabla \rho_0 = \mathbf{0}$, and solving for the perturbation pressure term, we obtain:

$$-\frac{1}{\rho_0} \nabla^2 p' = \frac{\partial u_i}{\partial x_j} \frac{\partial u_j}{\partial x_i} - \frac{\partial B_T}{\partial z} \quad (3.4)$$

In this equation the Einstein summation convention is implied. This is a Poisson equation, which means it is of the form $\nabla^2 p = f$, where f is called a forcing function. A well-known equation of this form is that for an electric field² in absence of a changing magnetic field, where the forcing function represents the charge distribution. In the case of convection, the forcing function consists of two separate terms. The first term on the right-hand side of Eq. 3.4 is one that depends on the velocity field, which will be called the *dynamic* forcing term. The second term depends on a buoyancy field, which may be nonzero even without movement, and may be called the *static* forcing term. The dynamic term may be decomposed, so that it becomes more clear which characteristics of the flow are associated with pressure perturbations. In Appendix A, it is demonstrated that Eq. 3.4 can be written as follows

$$-\frac{1}{\rho_0} \nabla^2 p' = \|\mathbf{D}\|^2 - \frac{1}{2} \|\boldsymbol{\omega}\|^2 - \frac{\partial B_T}{\partial z} \quad (3.5)$$

Here, \mathbf{D} is called the *deformation tensor* (or rate-of-strain tensor) and $\boldsymbol{\omega} = \nabla \times \mathbf{v}$ is the three-dimensional vorticity vector. To obtain a qualitative idea of the role of the dynamic forcing terms, the Laplacian operator may be thought of as a minus sign. This may be done because the Laplacian of a function tends to be maximized near a local minimum of a function. Doing so makes clear that a positive term on the right-hand side has a positive effect on the perturbation pressure:

$$p' \sim \|\mathbf{D}\|^2 - \frac{1}{2} \|\boldsymbol{\omega}\|^2 - \frac{\partial B_T}{\partial z} \quad (3.6)$$

The symbol \sim means 'behaves as'. We see that deformation of the flow is associated with a positive and vorticity with a negative pressure perturbation. An increasing (decreasing)

²in a linear, isotropic, homogeneous medium

thermal buoyancy with height is associated with a negative (positive) pressure perturbation. Because Eq. 3.4 is linear in p' , the perturbation pressure may be split into two components, $p' = p'_d + p'_b$. p'_d is called the *dynamic perturbation pressure*, and can be found by solving $-\frac{1}{\rho_0}\nabla^2 p'_d = \frac{\partial u_i}{\partial x_j} \frac{\partial u_j}{\partial x_i} = \|\mathbf{D}\|^2 - \frac{1}{2}\|\boldsymbol{\omega}\|^2$ with appropriate boundary conditions. p'_b is the *buoyancy-induced perturbation pressure*, which can be found by solving $\frac{1}{\rho_0}\nabla^2 p'_b = \frac{\partial B_T}{\partial z}$ with appropriate boundary conditions. Now, upon returning to the vertical component of the momentum equation, we find that it can be written as

$$\left(\frac{\partial}{\partial t} + \mathbf{v} \cdot \nabla\right)w = -\frac{1}{\rho_0}\frac{\partial p'_d}{\partial z} - \frac{1}{\rho_0}\frac{\partial p'_b}{\partial z} + B_T \quad (3.7)$$

It can be noted that, in this formulation of the vertical momentum equation, buoyancy exerts an influence in two ways: both directly and through its effects on the perturbation pressure. When considering the problem of a warm bubble within a cooler environment which is stationary initially, dynamic perturbation pressure will initially be nonexistent and will only gradually develop. However, buoyancy-induced perturbation pressure already exists as soon as sound and gravity waves have communicated the imbalance. Even in such a case, in which dynamic perturbation pressure may be ignored, buoyancy-induced perturbation pressure may not be ignored. Therefore, it makes sense to develop an expression for a more complete picture of buoyancy, namely the combination of the latter two terms in Eq. 3.7, i.e. $\beta = -\frac{1}{\rho_0}\frac{\partial p'_b}{\partial z} + B_T$, which has been done by Davies-Jones (2003a) who has coined it *effective buoyancy*. It is the solution of the differential equation

$$-\nabla^2\beta = g\hat{\nabla}_H^2\rho_T \quad (3.8)$$

which for the half-space $z > 0$, is

$$\beta(\mathbf{x}) = \int_{-\infty}^{\infty} \int_{-\infty}^{\infty} \int_{-\infty}^{\infty} \frac{g\hat{\nabla}_H^2\rho_T(\hat{\mathbf{x}})}{4\pi(\mathbf{x} - \hat{\mathbf{x}})} d\hat{x}d\hat{y}d\hat{z} \quad (3.9)$$

Here, ρ_T is the density of air (including any hydrometeors that it may contain), $\hat{\mathbf{x}} = (\hat{x}, \hat{y}, \hat{z})$, and $\hat{\nabla}_H = (\frac{\partial}{\partial \hat{x}}, \frac{\partial}{\partial \hat{y}}, 0)$. An interesting point of the derivation by Davies-Jones is that it does not involve the introduction of thermal buoyancy. Being based on a set of equations by Das (1979), the derivation does not involve quantities that are dependent on an arbitrarily chosen base state. Doswell and Markowski (2004) agree with this definition of buoyancy, and argue that it should be seen as *the static part of an unbalanced vertical pressure gradient force*. This means that buoyancy is given by the sum of thermal buoyancy and the vertical buoyancy-induced perturbation pressure gradient.

The buoyancy-induced term in Equation Eq. 3.6 indicates that the perturbation pressure tends to be positive (negative) where buoyancy decreases (increases) with height. So, given a positively buoyant bubble, we can expect positive perturbation pressure along its top boundary, and negative perturbation pressure along its lower boundary. In Fig. 3.1, these areas are shown marked with plus and minus signs. In addition, the figure shows field lines that indicate the local perturbation pressure field. We see that those field lines are oriented downward both inside and outside of the buoyant parcel. The net effect of

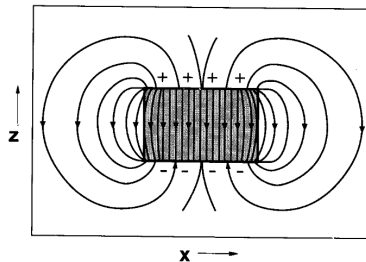


Figure 3.1: Buoyancy-induced pressure perturbation gradient force field, from Yuter and Houze Jr. (1995).

the buoyancy-induced perturbation pressure and buoyancy itself is to create a downward acceleration both outside the parcel and inside the parcel along its lateral boundaries, and an upward acceleration in the central part of the parcel.

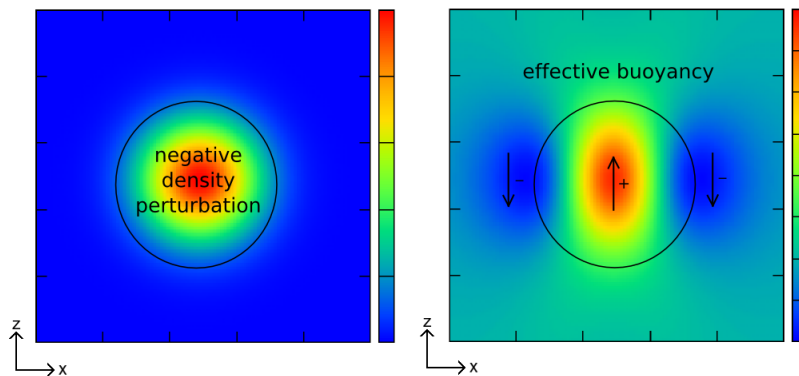


Figure 3.2: Vertical cross-section through a negative density perturbation (left), and the associated effective buoyancy β (right).

The net effect of the buoyancy-induced pressure perturbation can be seen when one solves Eq. 3.9 for an area of positive buoyancy (or a negative density perturbation) with respect to a hydrostatic base-state medium. Fig. 3.2 shows the resulting field of effective buoyancy in and around an area where a negative density perturbation was introduced in an otherwise homogeneous medium. In order to arrive at this image, the integral in Eq. 3.9 was numerically computed for a two-dimensional negative density perturbation $\rho(x, y, z) = \rho_0 - \rho' \exp(-\frac{x^2+z^2}{2\sigma^2})$. The contributions of the density distribution farther away from the parcel's centre than twice the size of the domain were neglected. If the effective buoyancy values correlate positively with the vertical velocity, we can expect a central updraught core flanked by peripheral downdraughts. In three dimensions, this would constitute a so-called vortex ring. This is a common characteristic of cumulus clouds, in which small-scale irregularities along the cloud's periphery can be seen to move downward, even at times when the cloud as a whole grows.

Bretherton and Smolarkiewicz (1989) have investigated the adjustment of the environment to the presence of convective clouds. They have found that circulations develop consisting of a flow away from the cloud at some height levels, and toward the cloud at other levels. The levels where the flow is oriented away from the cloud are those where the thermal

buoyancy of the cloud decreases with height. In an isolated storm, this usually occurs in the upper half of the troposphere and most strongly near the tropopause. Indeed, that is where anvil clouds are observed: large shields of ice particles that are carried away from the updraught by a horizontally divergent flow. Flow directed towards the convective cloud occurs in the lower troposphere, where the thermal buoyancy increases with height. The adjustment of the environment to such local buoyancy perturbations results from pressure perturbations that are communicated by gravity waves and acoustic waves.

A study based on observations of a storm system in weak vertical wind shear will now be presented, and the effects of buoyancy-induced flow in this case will be discussed.

3.2 The PRINCE measurement campaign

The measurement campaign PRINCE (Prediction, identification and tracking of convective cells), was carried out in southwest Germany within the framework of the COSI-TRACKS Virtual Institute of the Helmholtz Society in July 2006.

The goals of PRINCE were to investigate (i) why storm systems develop at the time and location where they are observed; (ii) in what ways its environment influence its development; (iii) in what ways the storm itself influences its environment and (iv) which effects these have on the subsequent convective evolution. The collected data allowed these questions to be partially answered for a case of a thunderstorm cluster that developed on 12 July 2006. It developed in an environment of weak vertical wind shear. It will be shown how the dynamics discussed in the previous chapter play a crucial role in the development of this storm cluster.

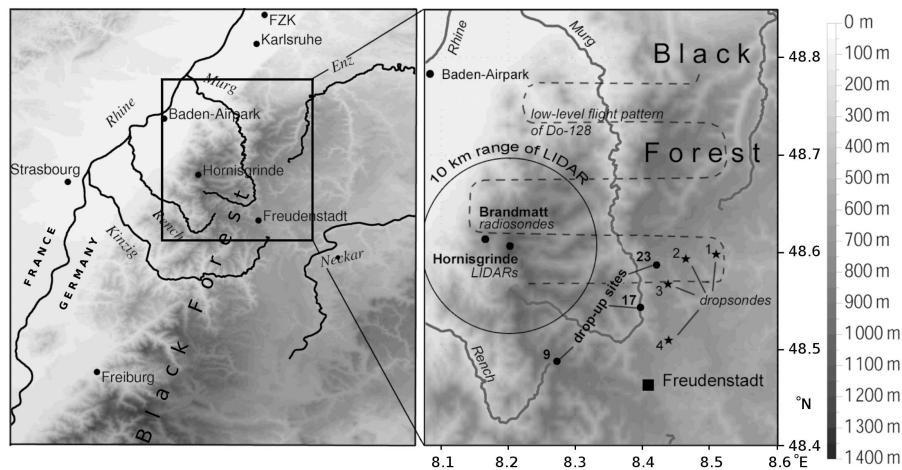


Figure 3.3: The Rhine Valley and Black Forest in southwestern Germany and the PRINCE field campaign area are indicated in the left panel. The relief is shaded. The sites of sensors and radiosonde releases (black dots 9, 17 and 23) are shown in the right panel including a 10 km range ring around the location of the lidars. The locations of dropsonde releases from the Dornier Do 128 (labelled 1 to 4) are shown as stars, and the low-level flight pattern followed twice by the aircraft is shown by a dashed line. The location of the C-band radar of Forschungszentrum Karlsruhe is marked by FZK.

During PRINCE, a number of new measurement strategies were deployed. Firstly, two lidars were positioned on the summit of a mountain. A scanning Doppler lidar measured the wind field, while a scanning rotational Raman lidar measured atmospheric temperature, the particle backscatter coefficient, and the extinction coefficient at a wavelength of 355 nm. Secondly, a research aircraft was equipped to receive near real-time data of meteorological satellites and data from ground-based operational weather radars. This allowed the aircraft to modify the flight track so that data in the vicinity of developing convective cells could be sampled. Finally, mobile teams equipped released radiosondes attached to weather balloons in the spatial and temporal vicinity of the most interesting convective processes.

The PRINCE measurement campaign was carried out in the northern Black Forest in southwestern Germany, a low mountain range flanked by the Rhine Valley to its west and elevated hilly landscape on its east (Fig. 3.3). Its highest peak, Hornisgrinde, is found in its western part and has its summit at 1164 m above mean sea level (AMSL). A number of winding valleys extend from the Rhine Valley (elevation of approx. 200 m AMSL) into the mountain range, including those through which the Murg and Rench rivers flow. In these valleys, pronounced valley and mountain breezes occur on days with strong insolation (Barthlott et al., 2005) as was the case on 12 July 2006, the day discussed here.

3.3 Measurement systems

Various sensors were placed on the summit of Hornisgrinde. The individual ground-based and airborne sensors that were operated will now be described briefly.

A 2 μm Doppler lidar 'WindTracer' was operated by Forschungszentrum Karlsruhe (FZK), which is a commercially available system produced by Lockheed Martin Coherent Technologies. The system sends out laser pulses with a 500 Hz repetition rate through a 2-axes scanner covering the entire upper hemisphere. Line-of-sight wind, signal-to-noise ratio, and aerosol backscatter are calculated by the system's real time data processing unit for 100 range gates selectable between 72 and 96 m length. Averaging 50 laser pulses yields a data rate of 10 Hz, covering at least the boundary layer up to a distance of 6–10 km, depending on the aerosol load present. During PRINCE, a scan pattern consisting of RHI (range-height-indicator, i.e., varying elevation at fixed azimuth) and PPI (plane-polar-indicator, i.e. varying azimuth at fixed elevation) scans have been performed. The system had a high scan speed (6 deg s⁻¹) and repeated its scan pattern every 5 minutes in an unattended continuous operation mode.

A C-band Doppler radar Gematronik Meteor 360 AC is located at the FZK, roughly 60 km north of Hornisgrinde. During PRINCE, it has continuously repeated a 14-elevation volume scan every 5 minutes, recording reflectivity and radial velocity data with a range resolution of 500 m and an azimuthal resolution of 1°.

A scanning rotational Raman lidar was operated by the University of Hohenheim. For the exact technical specifications, the reader is referred to Radlach et al. (2008). The lidar measures temperature, particle backscatter coefficient, and extinction coefficient at a temporal and vertical resolution of 10 s and 3.75 m, respectively.

A two-engine Dornier Do 128-6 research aircraft is operated by the University of Braunschweig and FZK. It has a nose boom designed for meteorological measurements in undisturbed air (Corsmeier et al., 2001) that contains redundant sensors for the measurement

of wind, temperature, and humidity. Using combined INS- (Inertial Navigation System) and GPS- (Global Positioning System) navigation, a sample frequency of 100 Hz is realized. With a mean ground speed of 65 m s^{-1} the spatial resolution of the measurements is less than 1 m. The accuracy of the horizontal wind speed is 0.5 m s^{-1} for the u- and v-component, and 0.1 m s^{-1} for the vertical wind. For temperature, the error is 0.2 K, and the mixing ratio has a relative error of 4.8%. The time required for the temperature sensor to indicate 63.5% of a sudden temperature change is 0.5 s. Precise high-frequency humidity measurements are accomplished by complementary filtering of Lyman-alpha and Humicap data, thus reaching a time constant of 0.04 s. In addition to the on-board sensors, the aircraft is equipped to release up to 30 autonomous operating dropsondes (see below) within a time frame of a few minutes.

A radiosonde site was established on the western slope of Hornisgrinde at Brandmatt, approximately 3 km west of the peak of the mountain. Several Graw DFM97 sondes were released from this site at 3 and 2 hour intervals during the daytime of 11 and 12 July, respectively. Additionally, radiosondes of the type developed by Kottmeier et al. (2001) were released by three mobile teams, and dropped from the Do 128 research aircraft. The mobile teams drove to pre-selected sites that had been identified as being suitable for the release of radiosondes. On each day of the campaign, the PRINCE Operations Centre decided to which of the sites the teams were sent, dependent on the expected weather development. On 12 July, stations 9, 17 and 23 were selected. Their locations are shown in Fig. 3.3. A special characteristic of the sondes is that the measured data is not transmitted via a radio signal, but is stored internally on a flash memory device to be read out after recovery of the sondes. In order to let the sondes be found afterwards, they are equipped with a mobile phone to send the geographical coordinates detected by a GPS receiver as an SMS message.

3.4 Meteorological set-up

For a discussion of the weather on the synoptic scale, analyses of the ECMWF Integrated Forecast System (IFS) of 11 July 2006 at 1200 UTC, and of 12 July 2006 at 0000 and 1200 UTC³ are presented in Fig. 3.4. The potential vorticity (PV) maps show an upper-tropospheric trough, characterized by high PV that moved eastward over southern Scandinavia late on 11 July. At 0000 UTC, 12 July, the southern part of the trough had developed into a thin streak of high PV stretching southwestward from southern Sweden to Belgium. As the northern part of the trough moved on into northeastern Europe, the streak split and a local maximum of upper-level PV cut off over northern France, approaching the PRINCE area at 1200 UTC on 12 July.

On 11 July at 1200 UTC (Fig. 3.4.a.), the surface pressure field shows a ridge extending from the northern Bay of Biscay towards Denmark. Behind the passage of the trough, this ridge elongated a bit further towards the Baltic Sea at 0000 UTC 12 July (Fig. 3.4.c.), before weakening and leaving the PRINCE area within a region of weak surface pressure gradients. In the temperature field, a zone of enhanced gradient can be seen to stretch from southern Scandinavia over via north and west Germany towards the Bay of Biscay. At all times, the PRINCE area was on the warm side of this zone.

³in the PRINCE field campaign area, local time = UTC + 2 hours

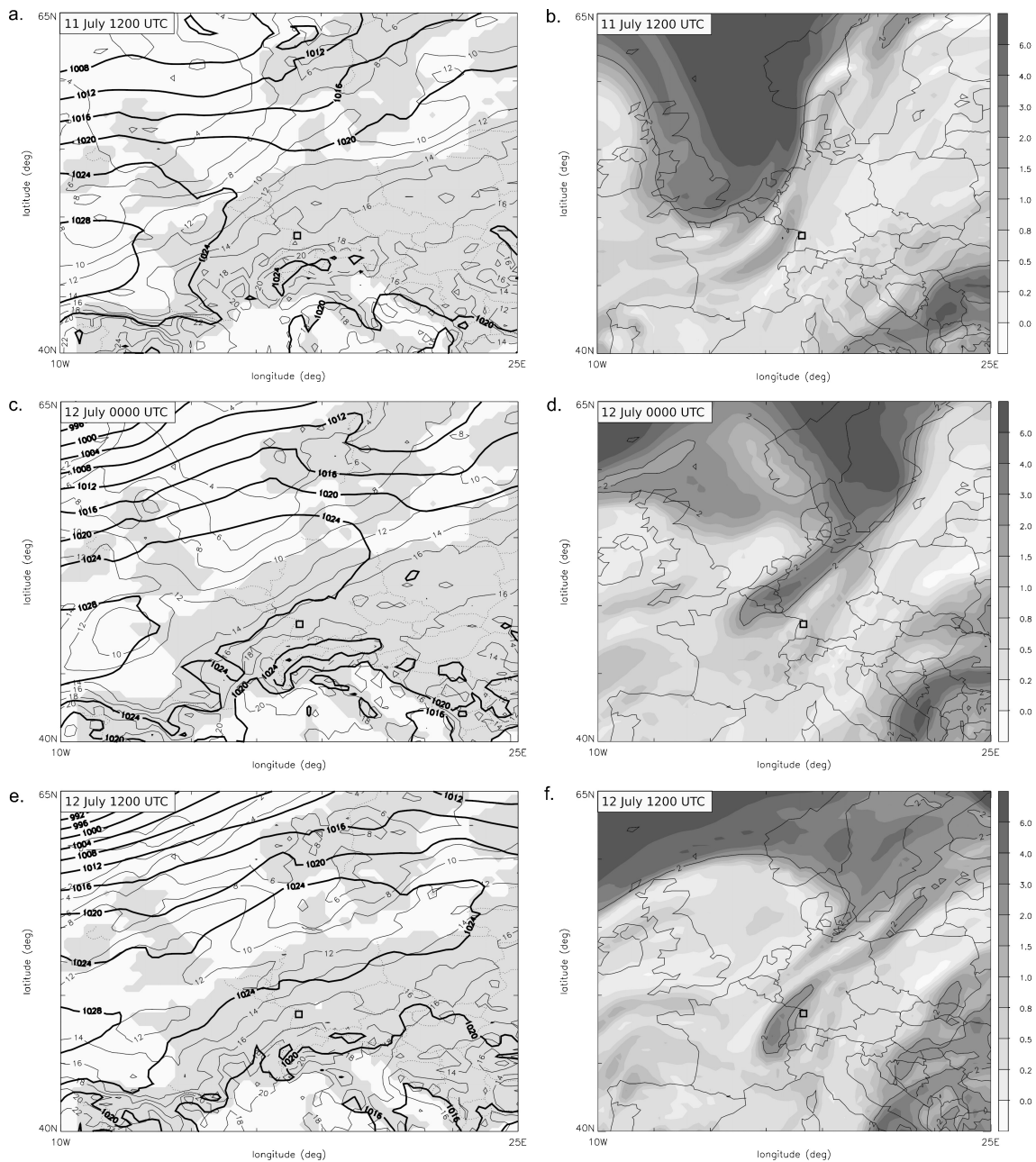


Figure 3.4: Analyses of the operational ECMWF integrated forecast system (IFS). Mean sea level pressure (hPa) and temperature ($^{\circ}\text{C}$) at the 850 hPa level (left), and potential vorticity (gray-scale, in potential vorticity units, i.e. $10^{-6} \text{ m}^2 \text{ s}^{-1} \text{ K kg}^{-1}$) at the 330 K level (right) at 1200 UTC 11 July 2006 (a, b) 0000 UTC 12 July 2006 (c, d) and 1200 UTC 12 July 2006 (e, f). The small square near the centre of each map indicates the PRINCE area (Fig. 3.3).

On the evening of 11 July 2006, isolated thunderstorms formed over the Vosges mountains, the low mountain range to the west of the Rhine Valley. In the early morning of 12 July 2006, storm systems formed over the Rhine Valley about 30 km to the west-northwest of Hornisgründe at around 0330 UTC. In what follows, the focus will be on the development of storms during the daytime of 12 July, when storms developed over the Black Forest.

date and time	CIN	CAPE
1303 UTC 11 July 2006	88	232
1900 UTC 11 July 2006	58	589
0702 UTC 12 July 2006	62	994

Table 3.1: CIN and CAPE for a 50-hPa mixed parcel at Brandmatt calculated from the radiosonde profiles of Fig. 3.5.

The fact that storms did not develop over the Black Forest on 11 July 2006 but did the following day, can be understood when considering the temperature and moisture profiles measured with sondes released at Brandmatt on both days (Fig. 3.5). At 1303 UTC on 11 July, a warm layer around 775 hPa acted as a strong lid preventing thermals from the boundary-layer to penetrate into the free atmosphere. CIN at that moment was 88 J kg^{-1} for a 50 hPa mixed-layer parcel (Tab. 3.1). At 1900 UTC, the air at 775 hPa and above was 1 to 2°C colder so that convective inhibition was reduced despite the formation of a shallow stable surface layer. This is likely to be a result of upward vertical motion induced by the approach of the upper-level vorticity maximum. At 0702 UTC on 12 July 2006, despite nocturnal cooling having reduced near-surface temperatures, CIN still had approximately the same magnitude. It would have been much higher if the air between 850 and 550 hPa had not cooled significantly.

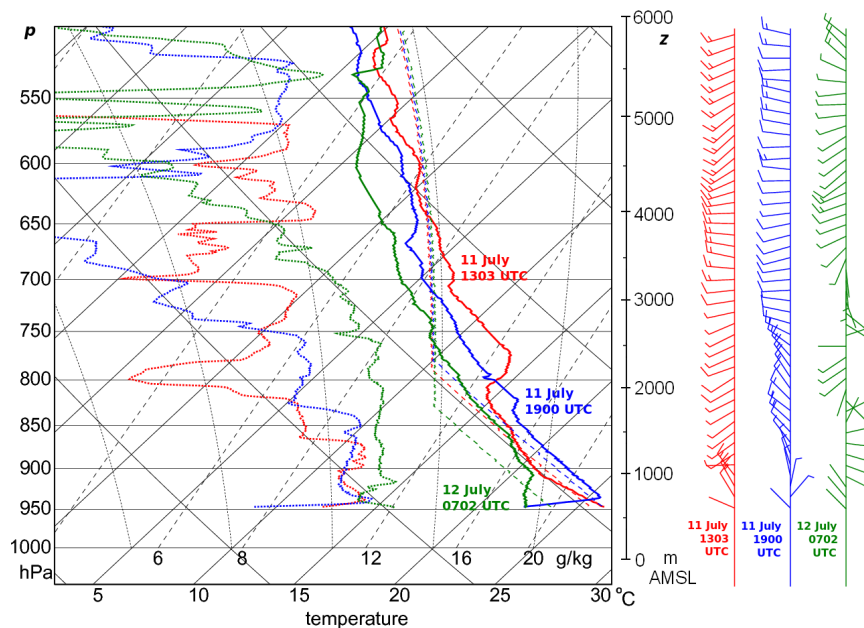


Figure 3.5: Skew-T-log-p diagram showing radiosonde ascents from Brandmatt (48.62°N ; 8.16°E) at 1303 UTC on 11 July 2006 (red) and 1900 UTC on 11 July 2006 (blue), and at 0702 UTC on 12 July 2006 (green). Dotted lines represent the dew point temperature, the continuous line temperature. The dashed coloured lines are temperature curves of lifted parcels originating from a 50 hPa thick mixed-layer right above the surface in Brandmatt. On the right-hand side, an approximate height scale is shown, as well as the horizontal wind direction and velocity. Wind barbs are plotted as shown in Fig. 2.5.

Most CIN appears in the lowest 2 kilometres AGL (above ground level) and can be expected

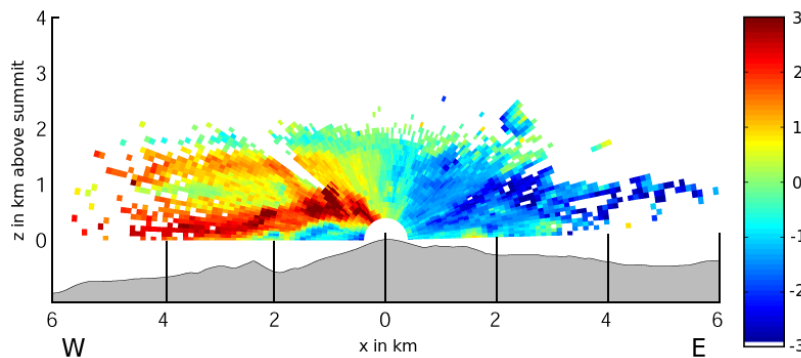


Figure 3.6: Radial wind velocity in m s^{-1} in a west-east transection measured with the Doppler lidar on Hornisgrinde at 0933 UTC (z in km above the lidar). Blue colours represent a velocity component towards, and red colours a component away from the lidar. The velocity to the west of Hornisgrinde summit represents the upslope branch of the mountain breeze system. A return flow (red) can be observed on top of it.

to disappear by diurnal heating. Unlike the profiles of 11 July, no well-defined warm layer that could inhibit deep convective development was present above 2 km AGL, except for an inversion at 530 hPa (about 5.5 km AMSL, i.e. above mean sea level). This inversion, that was evident in later ascents from Brandmatt and in the 12 UTC radiosonde data from nearby Nancy and Stuttgart (not shown), would later indeed influence the development of convective storms.

In the morning of 12 July shortly after 0800 UTC, a well-mixed planetary boundary layer (PBL) was present over the summit of Hornisgrinde. A scan by the Doppler lidar from west (left) through the zenith to the east (right) at 0933 UTC is shown in Fig. 3.6.

It displays several layers with different velocities. To the east of the summit, winds with an easterly component of about 1 to 2 m s^{-1} are observed throughout most of the layer in which data was available. On the western (left) side of the summit, the flow pattern is quite different: a bottom layer of winds with a 1 m s^{-1} westerly component is found, that has a thickness of approximately 700 m, representing the upslope branch of the mountain breeze system. At some distance from Hornisgrinde, this layer disappears below the lowest possible elevation (0 degrees) of the lidar. A 500 to 700 m thick layer above this surface layer has an easterly wind component of 2 to 3 m s^{-1} . Except for a weak flow to the north, no near-surface flow away from the mountain top can be detected in VAD scans of the Doppler lidar (not shown). This supports the idea that the air within the upslope flow out of the Rhine Valley rises near the mountain top and returns towards the valley as part of this elevated easterly flow. The overall easterly flow, that is also detected east of Hornisgrinde, likely contributes to it as well.

3.5 Convective initiation

Moist convection on 12 July starts around 0830 UTC, when the first convective clouds are observed across the slopes of the Murg Valley. At 0924 UTC, the C-band radar detects the first hydrometeors produced by deep convective clouds across the hills east of the Murg Valley (not shown).

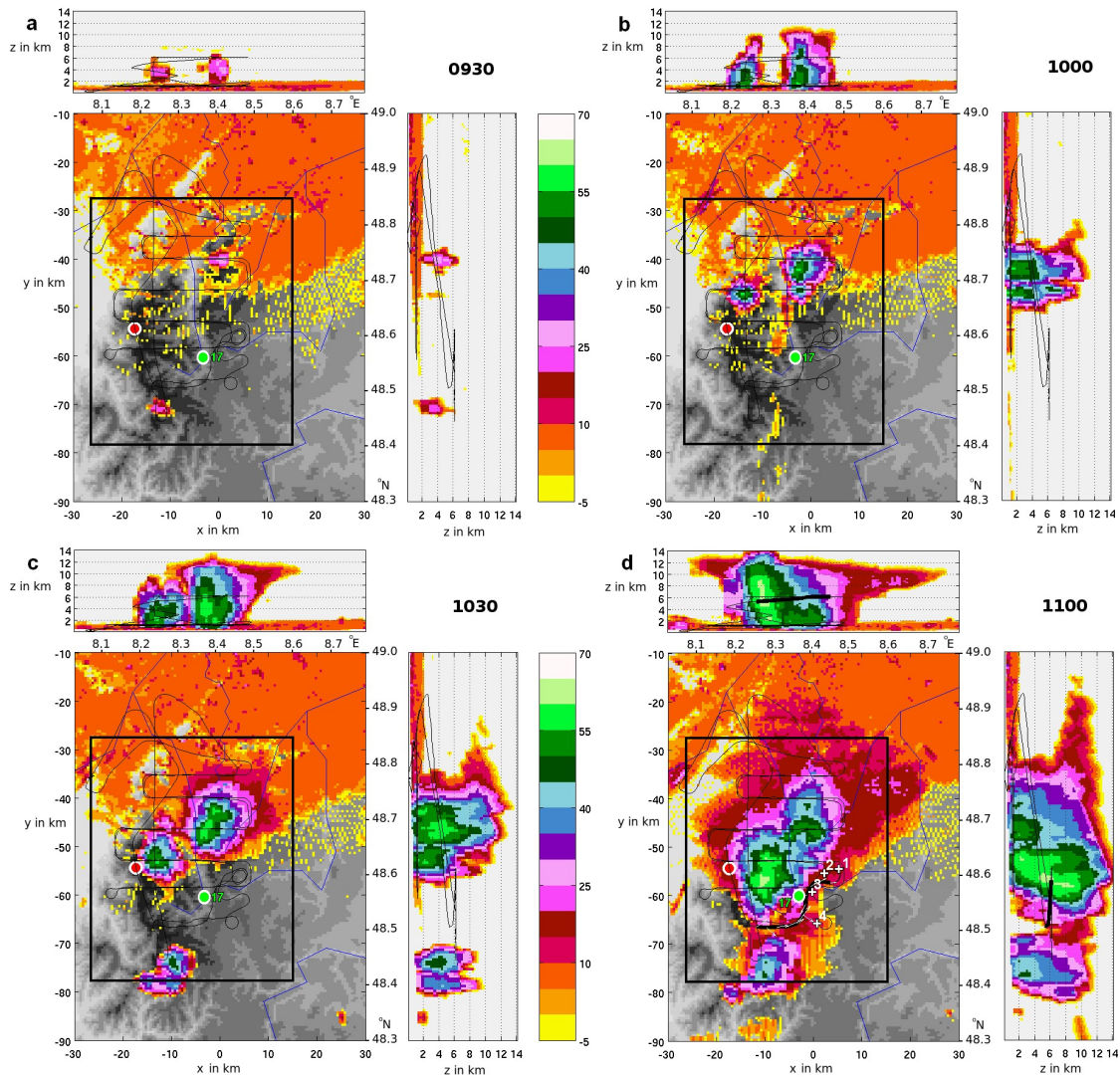
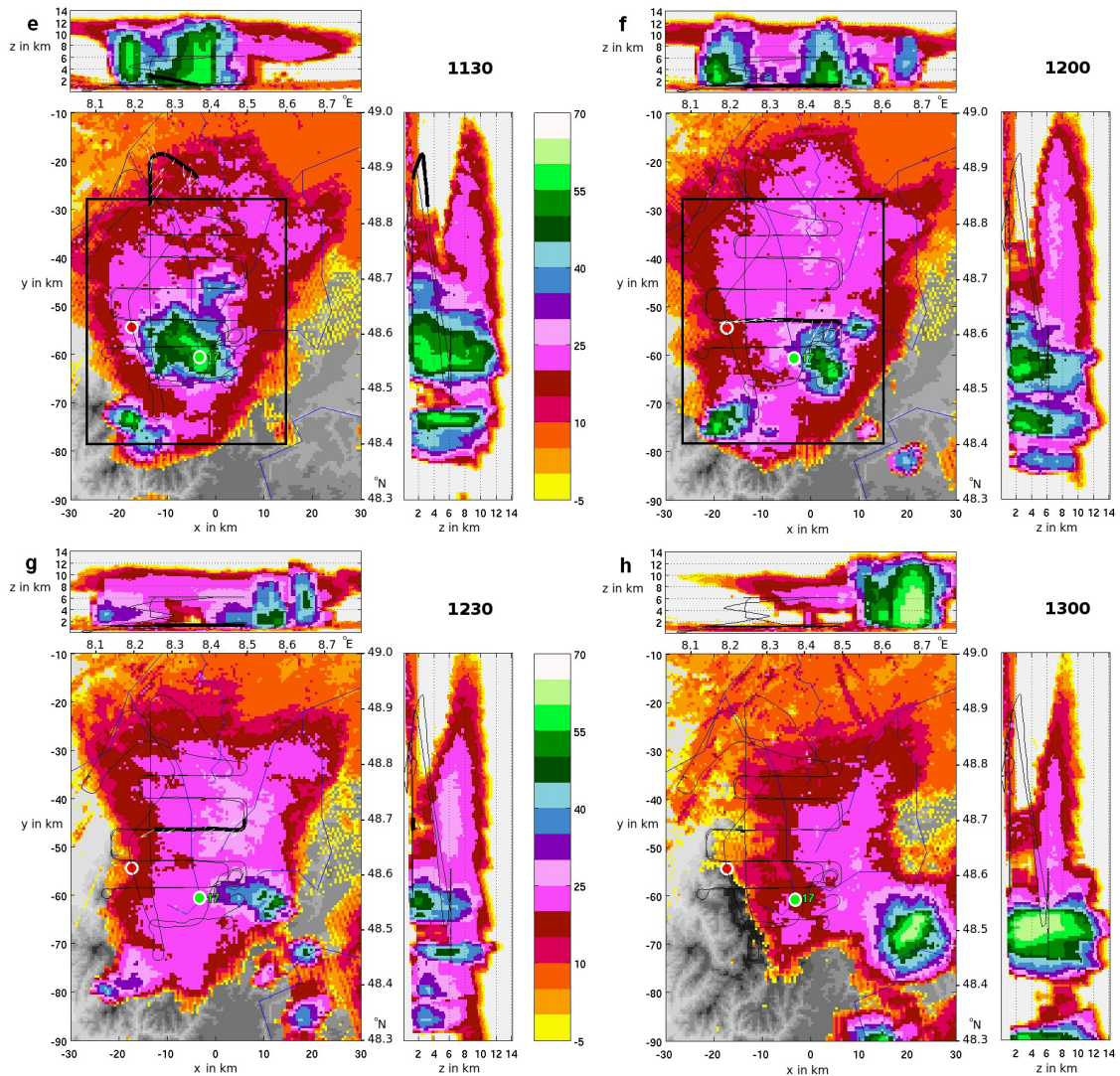


Figure 3.7: Reflectivity (dBZ) measured by the C-band radar located at the FZK (Fig. 3.3) in 30 minute intervals from 0930 to 1300 UTC. The maximum reflectivity observed in a vertical column is projected on the x, y -plane map showing the topography. The maximum reflectivity in a north-south slice is projected on the x, z -plane (top of each sub-figure) and the maximum in an east-west slice projected on the y, z -plane (right of each sub-figure). The z -coordinate is given in km above MSL. The narrow black lines are the projections of the flight pattern of the Do 128 research aircraft on the respective planes. The black rectangles in each sub-figure denote the PRINCE area (Fig. 3.3). The red dot is the summit of Hornisgrinde, the green dot radiosonde station number 17. The white crosses in sub-figure d, labelled 1 to 4, are the locations of dropsondes which are discussed in the text later. The figure continues on the next page.

The evolution of the radar echoes on 12 July are shown in Fig. 3.7. At 1000 UTC, weak echoes are also detected to the north-northeast of Hornisgrinde, i.e. west of the Murg Valley (Fig. 3.7.b). After 1030 UTC, new convection develops on the southeastern flank of the westernmost storm. This storm then merges with the eastern storm and becomes a multi-cell cluster with a large anvil cloud and a net south-southeastward propagation.



The situation at 1010 UTC is depicted in Fig. 3.8. At that moment, the convective storm that has initiated east of the Murg Valley (the one centred near -3 km east and -45 km north in the radar-relative coordinate system) has broken through the inversion at about 5 km altitude, for reflectivity over 40 dBZ can be seen to extend up to 10 km AGL in the vertical projections to the top and to the right of the figure. However, the system west of the Murg Valley (centered near -13 km east and -47 km north) does not grow as quickly. Only weak reflectivity is detected above 5 km AMSL. Photographs taken from the city of Karlsruhe (not shown) suggest that the eastern system rapidly broke through the inversion whereas the western one was significantly hindered by it: its top spread out horizontally in the mid-troposphere.

This can be understood when one realizes that across those height intervals where $\frac{\partial B_T}{\partial z} < 0$, a net detrainment of updraught air is to be expected (Bretherton and Smolarkiewicz, 1989), or in other words, a net horizontal outflow out of the updraught. In this case, the inversion layer that can be identified in Fig. 3.5 at 0702 UTC, and in Fig. 3.11 at 1108 and 1259 UTC, was probably the cause of the spreading out.

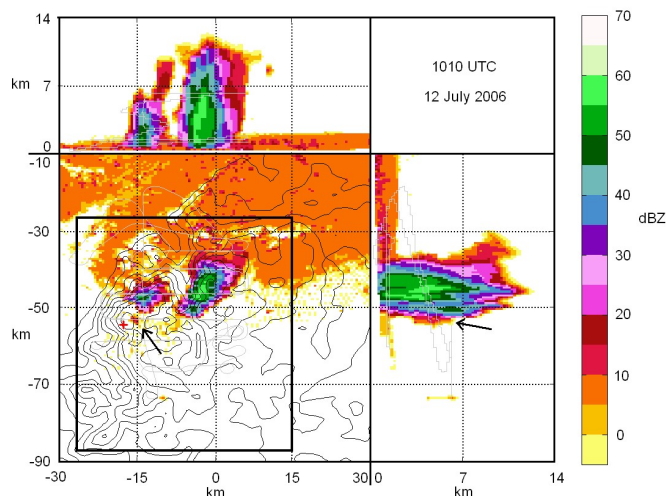


Figure 3.8: Reflectivity (dBZ) as measured by the C-Band radar at 1010 UTC (displayed as in Fig. 3.7, except that the topography is contoured). The arrow indicates the initiating cell discussed in the text, and the small red cross is the summit of Hornisgrinde. The bold rectangle denotes the PRINCE area as defined in Fig. 3.3.

At 1008 UTC, a new small cell, marked with an arrow in Fig. 3.8 both in the x,y and in the y,z projections, developed slightly to the northeast of Hornisgrinde. This cell merged with the existing western convective system during the following half hour. The fact that the cell developed close to the lidars at Hornisgrinde enables us to study the low-level wind field measured by the Doppler lidar. Fig. 3.9 shows the radial wind component in a scan at 4 degrees elevation. Two boundaries of abrupt changes of radial velocity in the radial direction are indicated, labelled A and B. Along boundary A, inward velocities close to the radar change to outward velocities further away from the lidar. This is easily explained by noting that the lidar pointing westward is sampling the upslope branch of the valley breeze system close to the radar and the return branch at greater distances.

To the east of the lidar, the wind field has changed considerably in comparison with that measured at 0933 UTC (Fig. 3.6). Directly to the east of the lidar, winds now have a westerly component. Along boundary B, located at about 5 km from Hornisgrinde, an outbound-to-inbound direction change occurs implying that radial velocities converge along it. Although tangential velocity components are not known, the collocation with the reflectivity core above the same location is striking, and strongly suggests that low-level mass convergence was taking place.

3.6 The mature and decaying storm system

Starting at 1033 UTC, the Doppler lidar scans indicate a shallow outflow from the storm system crossing Hornisgrinde. An RHI scan along the east-west plane at 1103 UTC shows the flow from east to west across Hornisgrinde (Fig. 3.10) at lower altitudes (up to approximately 500 m AGL). A clear westerly velocity component towards the storm was observed above that layer. The interface between the easterly flow away from the storm system and westerly flow towards it, slopes down to the west.

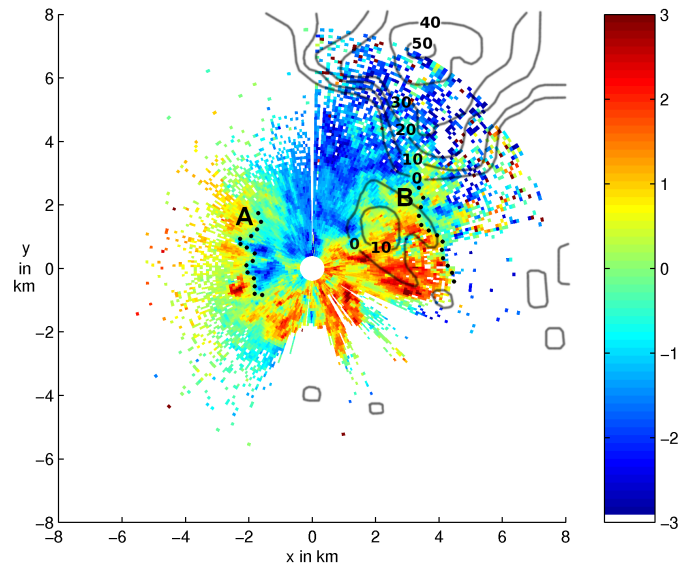


Figure 3.9: Radial velocity (in m s^{-1}) as measured by the Doppler lidar at 1008 UTC during a PPI scan with a 4° elevation (shaded) and maximum column reflectivity (in dBZ) of the C-Band radar at 1010 UTC (contours). Blue colours indicate motion towards the lidar, red colours away from the lidar. Between 0° and 140° azimuth (i.e. between the north and east-southeast) the data has been filtered less than at other azimuths in order to allow for a better contrast across line B at the expense of some noise reduction.

The sonde released at Brandmatt at 1106 UTC (Fig. 3.11, red) shows weak northeasterly winds between 900 and 850 hPa, consistent with the weak outflow of the storm system observed by the Doppler lidar. This layer has a higher potential temperature than the air in the Rhine Valley below 900 hPa that still has a weak component towards the storm, so that it has spread out on top of this layer. The temperature minimum observed near 700 hPa is thought not to represent the actual air temperature, but rather the result of cooling of the temperature sensor owing to the evaporation of cloud droplets that had accumulated on the sensor while crossing a cloud layer near 730 hPa.

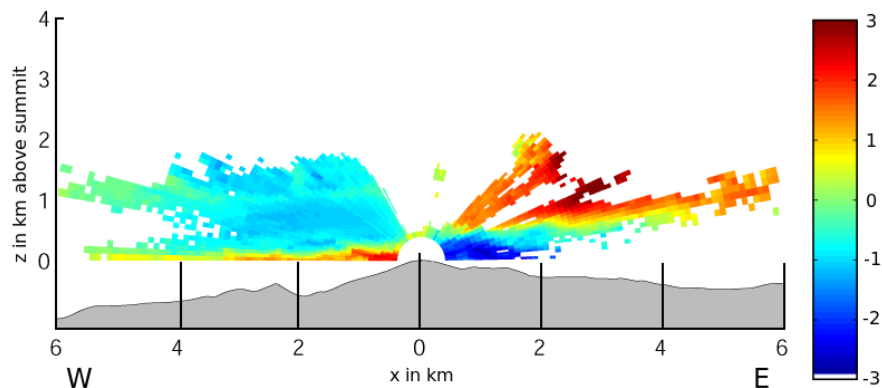


Figure 3.10: As Fig. 3.6, but at 1103 UTC.

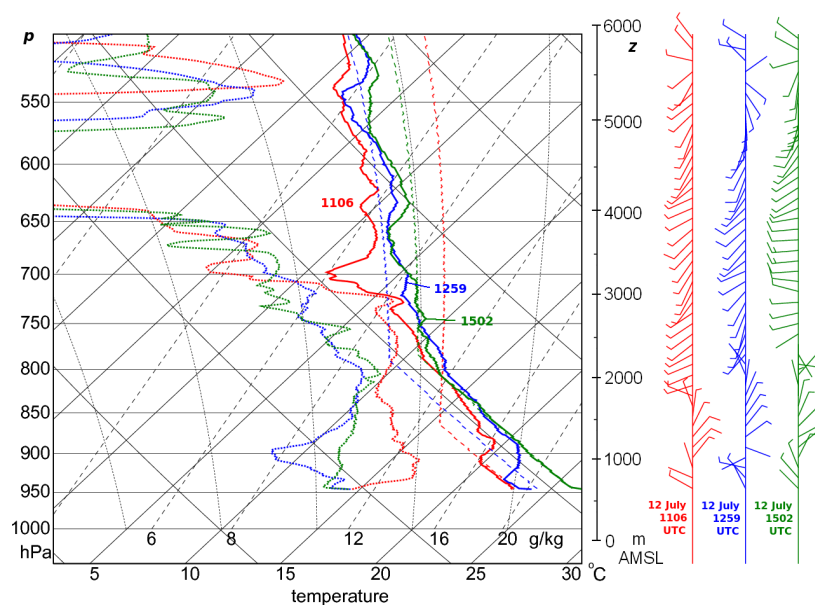


Figure 3.11: Skew-T log-p diagram as in Fig. 3.5, but here showing three radiosonde ascents from Brandmatt on 12 July at 1106 UTC (red), 1259 UTC (blue), and 1502 UTC (green). Wind barbs are plotted as in Fig. 2.5.

Initially, the outflow air between 900 and 850 hPa was rather moist as the 1106 UTC ascent indicates an average specific humidity near 11 g kg^{-1} in that layer. At 1259 UTC, however, the outflow contained much less moisture, on average about 9 g kg^{-1} . The sounding released at 1502 UTC indicates that even hours after the storm system has dissipated, the low-level moisture has not recovered to the level of 1106 UTC.

When the development of the storm system was well underway, the Do 128 research aircraft released six dropsondes from an altitude of about 6300 m AMSL. The sondes sampled both the environment below the anvil cloud of the storm and developing convective updraughts. The location of four of the sondes, numbered 1 to 4, are plotted in Figs. 3.3 and 3.7.d. The profiles of equivalent potential temperature θ_e and the saturated equivalent potential temperature θ_{es} are displayed in Fig. 3.12. The variable θ_e has been selected because of its property to be approximately conserved under both dry and moist adiabatic vertical motions. θ_{es} has been plotted in order to find out where a sonde penetrated a cloud. Moreover, it is a measure of temperature. From the definition of θ_{es} it follows that where both curves overlap the air is saturated, which corresponds to a good approximation with areas containing clouds.

Sonde 1, that was released just to the east of the storm system, shows a layer of warm, unsaturated air (labelled A) above 5600 m, topping a layer of slightly cooler, almost saturated air (B) below. The profile is comparable with that of the pre-convective environment as sampled by the radiosonde released at Brandmatt at 0900 UTC, which is displayed on the right of Fig. 3.12. It can be seen that the air at A is warmer, having a θ_{es} of 68°C , than the air sampled earlier at Brandmatt at the same altitude which had a θ_{es} of 58°C . The high temperature of the air sampled by dropsonde 1 can be explained by adiabatic warming of air that descended out of the storm's anvil region as part of compensating downdraughts of the thunderstorm. The lack of drying that one would expect to see in subsiding air can be

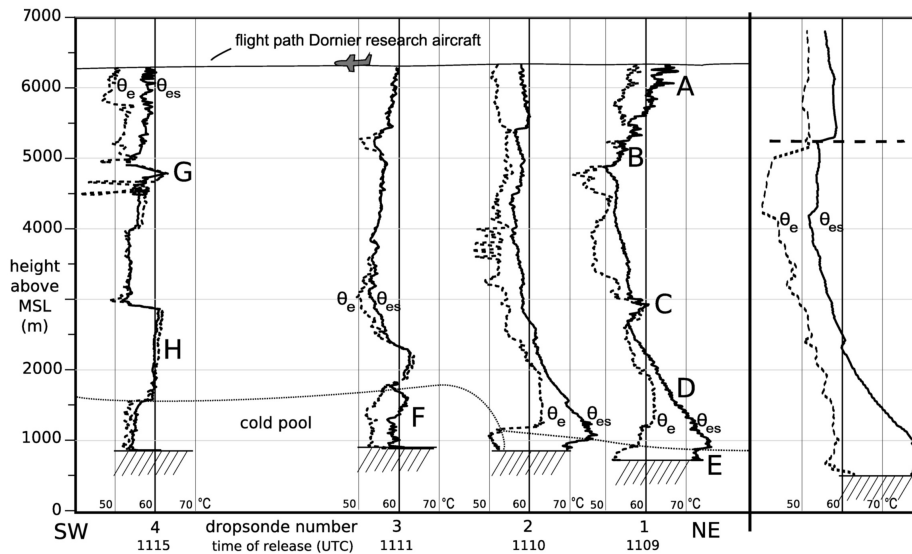


Figure 3.12: Equivalent potential temperature θ_e (continuous lines) and saturated equivalent potential temperature θ_{es} (dotted lines) as measured by the dropsondes released by the Do 128 research aircraft between 1108 and 1114 UTC. On the right, the radiosonde released at Brandmatt at 0900 UTC is shown for comparison. The grey line indicates the upper boundaries of a cold pool in soundings 3 and 4, and of a radiationally-cooled layer (see text) in soundings 1 and 2.

explained by the evaporation of hydrometeors falling out of the anvil cloud into this layer. The saturated layer B between 5600 m and 4800 m probably originates from the spreading out of a part of the convective updraught against the inversion discussed above, which was present in the pre-convective environment. In the Brandmatt sonde, this inversion is visible at 5200 m. A cloud deck like B is visible in the right bottom of Fig. 3.13, which shows a photograph taken from the research aircraft while flying at about 6300 m AGL, a few minutes before sonde 1 was released.



Figure 3.13: Photograph taken by pilot R. Hankers from the Do 128 research aircraft at 1100 UTC looking to the east. It shows a developing convective updraught (left), a cloud deck with stratiform characteristics (right bottom), part of an anvil cloud and storms along the Swabian Jura to the southeast of the PRINCE area in the distance.

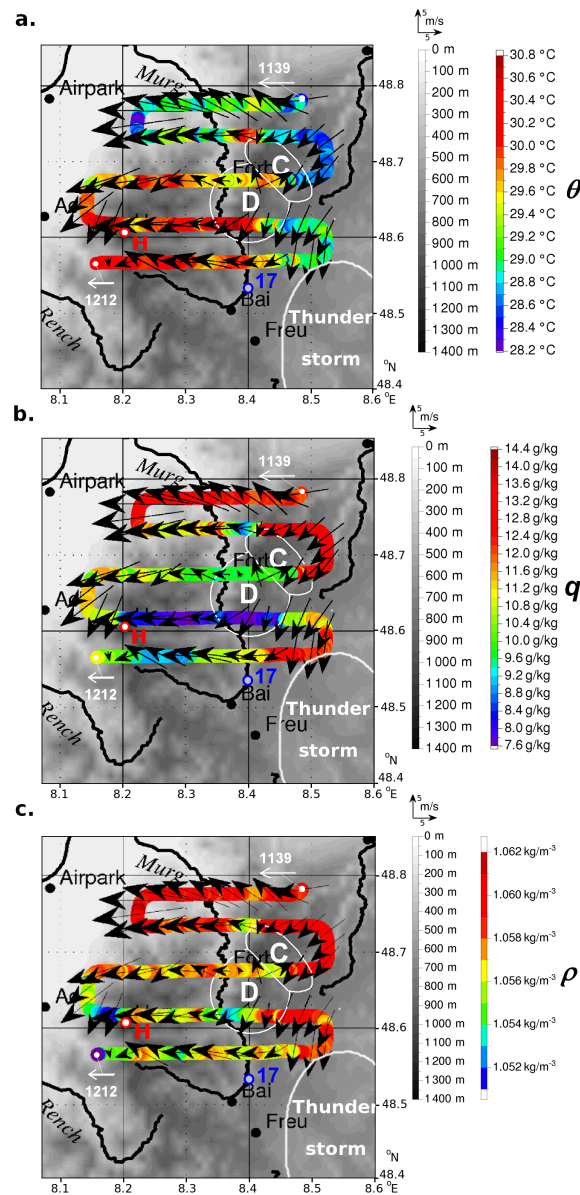


Figure 3.14: Measurements of potential temperature (a), specific humidity (b), and air density (c) taken by the Do 128 research aircraft between 1139 and 1212 UTC at an altitude of 1150 m AMSL. The horizontal wind vector along the flight path is indicated with black arrows in diagrams a–c. Hornisgrinde (H) is indicated by a red circle and the letter H, and radiosonde station 9 by a blue circle. The approximate location of the storm system at 1200 UTC, i.e. to the southeast of the flight pattern, is indicated. The areas labelled C and D, respectively, indicate where confluence and divergence of the horizontal wind field was observed.

Below 4800 m, the profile of sonde 1 has more or less the same properties as the undisturbed environment, with the exception of the feature labelled C. There, the sonde has briefly travelled through a large cumulus cloud containing air originating from the boundary layer. Just below the maximum of θ_e and θ_{es} the former briefly exceeds the latter, which suggests that the air was super-saturated. That, however, has not necessarily been the case, as it probably was an undesired artifact of the instrument caused by the accumulation of drops

of liquid water on the dew-point mirror.

Below the cloud element, the sonde again falls through air having temperatures not too different from those of the pre-convective environment (D), except that the air is slightly moister. In the lowest 200 m above the surface, a shallow layer of somewhat cooler, drier air (E) is observed. The wind within this layer was from north to northeasterly directions and had no component away from the storm, so that the outflow of the storm is an unlikely cause of its dry and cool properties. It can be hypothesized that the lower temperatures of layer (E) are a result of radiational cooling, caused by shading by the anvil cloud, that, at the time of the measurement, had already blocked direct sunshine for about 2 hours.

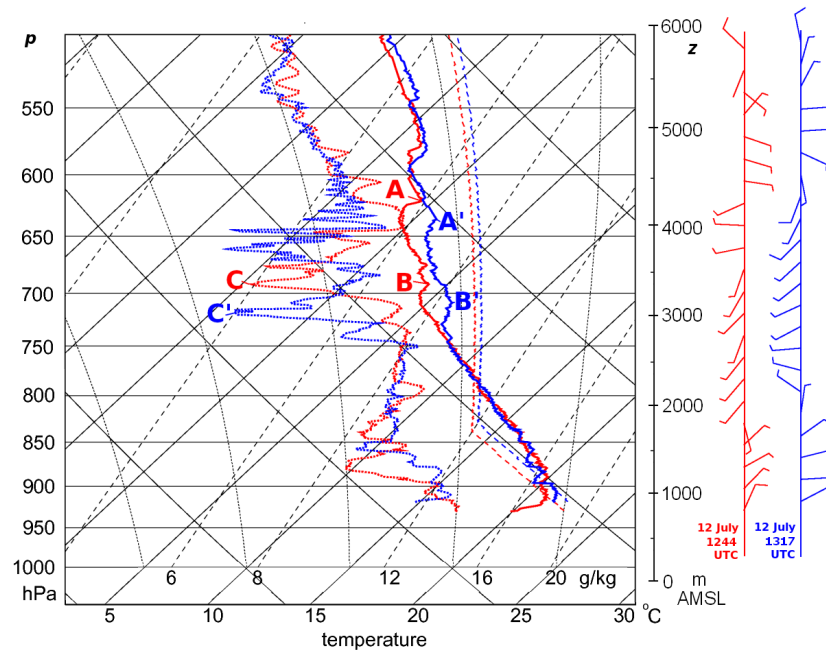


Figure 3.15: Temperature, moisture and wind profile depicted as in Fig. 3.5, as measured by radiosondes released at station 9 at 1141 (red) and 1245 UTC (blue), respectively. Wind bars are plotted as in Fig. 2.5.

The profile measured by sonde 2 that was released about 3 km further westward, has lower temperatures in region A and does not feature regions B and C. Like sonde 1, this sonde also detects cool, dry air near the surface.

Dropsonde 3 has been released within precipitation on the southeast side of the storm system. The profile displays a high relative humidity close to saturation between 6500 m and 3500 m. Below approximately 2300 m, a convective cloud element has likely been sampled. Below the saturated layer that stretches down to 1800 m, a 700 m-thick layer of cool air is observed (F), with much lower values of θ_{es} than the previous two sondes indicated. Cooling by evaporation of hydrometeors is the most likely source of this, and we believe that the cold pool of the storm system has been sampled here. Dropsonde 4 has been released above a developing towering cumulus cloud. The sonde approached the cloud (G) at 4800 m, but was not able to penetrate it because of the large upward velocities associated with it. At some point, the GPS device had detected an upward motion of 5 m s^{-1} . Considering that the typical fall speed of the dropsonde lies between 3 and 5 m s^{-1} , this implies that the air around the sonde was moving upward at 8 to 10 m s^{-1} . Indeed, the

difference of $10.0\text{ }^{\circ}\text{C}$ in θ_{es} between the cloud and the air outside of it corresponds with an actual temperature difference of $4.5\text{ }^{\circ}\text{C}$, indicating that the air within the cloud had a high thermal buoyancy. Below 2800 m , the sonde again encountered a convective updraught (H) that had approximately the same θ_e as the convective cloud element G encountered before. Below 1600 m , sonde 4, like sonde 3 samples cold and moist air associated with the storm system's cold pool. After releasing the dropsondes, the Do 128 research aircraft descended to 1150 m AMSL and started to fly the pattern indicated by dashed lines in Fig. 3.3, starting in the northeast at 1139 UTC and reaching the end of the pattern at 1212 UTC . While doing so, temperature, moisture and three-dimensional wind data – corrected for the motion of the aeroplane – were recorded. The respective temperature, moisture and density data are shown in Figs. 3.14 a, b and c. During this part of the flight, the storm system moved southeastward just quickly enough that it moved out of the planned flight pattern before the aircraft arrived at its most southeastern point. The approximate location of the storm at 1200 UTC is indicated in Figs. 3.14 a, b and c. The pattern of potential temperature shows a relative maximum with temperatures between $30\text{ }^{\circ}\text{C}$ and $31\text{ }^{\circ}\text{C}$ across the southwestern part of the probed area, whereas values are around $29\text{ }^{\circ}\text{C}$ further to the north and east. The moisture shows a similar pattern with the highest moisture being observed where temperatures are lowest. In the northern and eastern parts of the pattern, the specific humidity was generally between 12 and 13 g kg^{-1} , while it drops to below 8 g kg^{-1} in the central and southwestern parts. These data have been used to calculate the density of the air that was sampled using the equation of state.

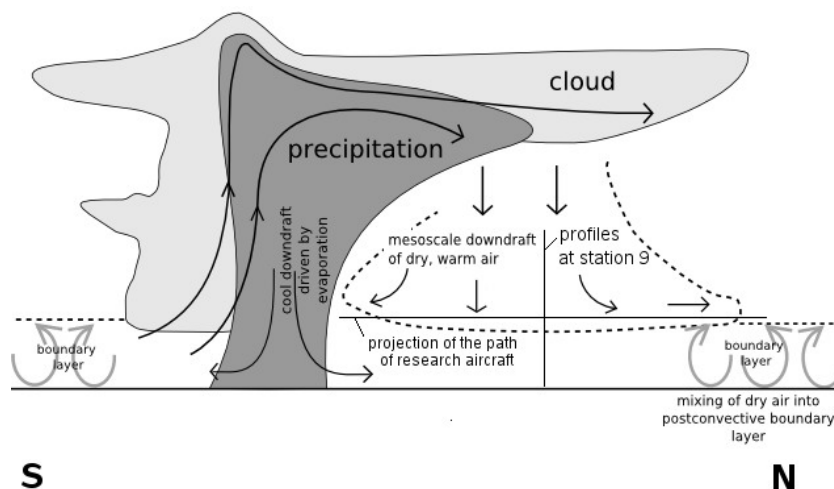


Figure 3.16: Idealized cross-section of the storm system that occurred on 12 July 2006 over the Black Forest and its up- and downdraught regions. The system's propagation was in a south to south-easterly direction. A projection of the flight path and the approximate location of the radiosondes of Fig. 3.15 are indicated.

As the aircraft was at that moment flying through considerably sub-saturated air that did not contain any hydrometeors, the effects of liquid water need not to be included in the equation. The absence of hydrometeors has been confirmed by the aircraft crew and is consistent with the measurements of the C-Band radar. The resulting density data shown in Fig. 3.14 c indicate that the air in the southwest was the least dense. The density difference between the southwest portion of the pattern and the north and east is about 3 g m^{-3} . Such a difference can be caused by a perturbation of 0.6 K in the temperature,

1.0 g kg⁻¹ in mixing ratio or 2.5 hPa in pressure, which is much more than the accuracies of the sensors, which are 0.2 K, 0.5 g kg⁻¹ (at 10 g kg⁻¹) and 0.1 hPa, respectively. Hence, the observed low density cannot be attributed to measurement errors.

The observed winds show a divergent pattern (labelled D) and confluence (C) to the east of the town of Forbach (Forb). Winds in the northern part of the flight pattern have an easterly component, while those to the east have a northerly component. This suggests that the northeasterly flow in the environment of the storm splits into two branches where it is blocked by the diverging dry and warm air over the Murg Valley. The dry and warm air must have descended from higher altitudes as horizontal advection of air within a relatively homogeneous air-mass cannot result in local extrema of temperature or moisture. Moreover, the wind field depicted in Fig. 3.14 does not indicate that the dry air was advected towards the storm system. On the contrary, moist air is advected southwestward towards the storm, until it is blocked by the divergent dry air.

Another indication of downward motion taking place can be obtained from the radiosondes released at station 17. Data of two of the radiosondes, released at 1244 (red) and 1317 (blue) UTC are shown in Fig. 3.15. Both soundings were taken when the storm system was located under the anvil cloud of the storm system located east of the station, just before and just after the radar image of Fig. 3.7h, respectively. The profile at 1244 UTC shows the existence of two warm layers A and B, the latter being very dry (C). At 1317 UTC, both layers have descended about 20 hPa or 200 m. Weak horizontal winds suggest that this is true local subsidence and not caused by horizontal advective effects. The vertical velocity associated with this subsidence can be calculated by dividing the observed altitude differences of A, B and C by the time span between the two detections of each feature. This yields a vertical motion of around -0.4 m s⁻¹ for each feature. As shown by Fig. 3.15, the features A, B and C were present at altitudes between 3000 and 4500 m AMSL or between approximately 2000 and 4200 m AGL. Because in the absence of horizontal winds the vertical wind component must vanish at the surface, it can be understood that the Do 128 research aircraft was not able to detect coherent downward motion when flying the pattern between 100 and 800 m AGL, its measurement error for vertical velocities being 0.1 m s⁻¹.

An idealized cross-section is sketched in Fig. 3.16. It displays the convective updraughts that generally occurred on the southern (left) side of the system as it propagated to the south-southeast. Given the dryness of the mid-troposphere, it is likely that considerable amounts of precipitation from the storm evaporated before reaching the surface, which has likely lead to cooling and localized downdraughts in the vicinity of the strongest radar echoes. The warm, dry lower troposphere as observed by Do 128 between 1139 and 1212 UTC over the Murg Valley region and the warming observed between 1141 and 1241 UTC at station 9 is depicted as a large mesoscale downdraught that occurred under the anvil cloud of the storm between and to the north of the convective updraughts.

An important characteristic of the downdraught was that it did not reach down to the earth's surface except at the top of Hornisgrinde and possibly some other hills and mountains. Indeed, warm and dry downdraughts are not commonly observed at the surface unless they have very high downward momentum, as in so-called heat bursts (e.g. Johnson, 1983), which do not reach the earth's surface.

3.7 Inhibition by compensatory subsidence

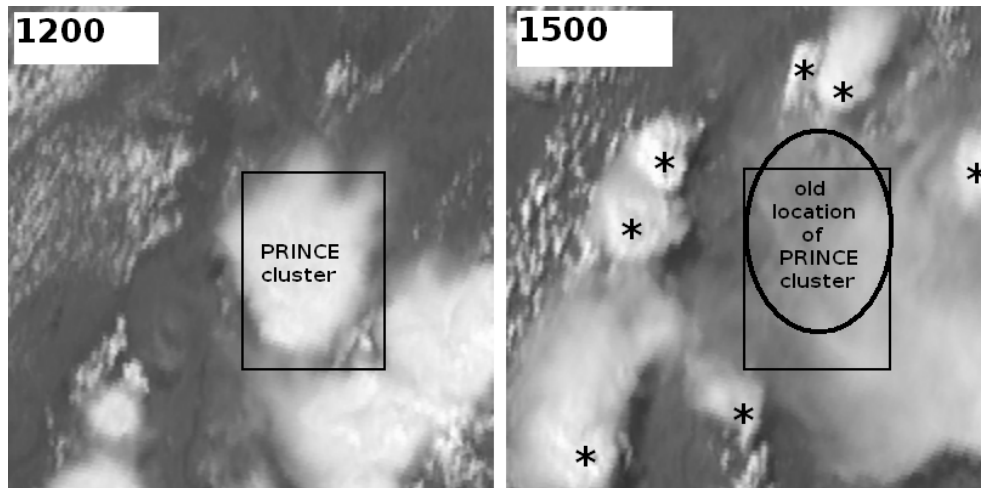


Figure 3.17: The 'PRINCE' convective cluster observed by Meteosat 8 (VIS) at 1200 UTC (left) and the new convective development around the original cluster location at 1500 UTC on 12 July 2006 (right) marked by stars. The rectangle corresponds to the PRINCE region indicated in Fig. 3.3. Courtesy of EUMETSAT.

It turned out that no storms developed within the PRINCE area after the initial storm cluster dissipated, whereas they did at surrounding locations. Fig. 3.17 shows two visible satellite images at 1200 and 1500 UTC. It can be seen that at 1200 UTC, the PRINCE cluster is one of the first storm clusters to develop, together with larger clusters in the southeast of the picture that develop over the Swabian Jura. Three hours later, the storm cluster has dissipated leaving some remnant cirrus fields over the Black Forest. At that moment, many new storms are initiating to the south, southwest, west, north and northeast of the dissipating cluster. One may be tempted to attribute the suppression of convective initiation near the PRINCE cluster to the presence of a cold pool under the dissipating thunderstorm caused by evaporation of hydrometeors or reduced insolation. However, the soundings at Brandmatt (Fig. 3.11) do not indicate any cooling of the boundary layer between 1200 and 1500 UTC. Insolation through the thin cirrus after the system's decay has apparently been sufficiently strong to compensate any prior cooling, which leads to the conclusion that shading by cirrus clouds has not been a dominant effect near Hornisgrinde. The sounding released at Brandmatt at 1502 UTC indicates that the moisture content of the boundary layer did not recover from the moisture drop that resulted from the downward flux of dry air. Additionally, the temperatures of the air directly above the boundary layer remained higher than before the convective cycle started. Both effects strongly reduced the buoyancy of a surface parcel in the first few kilometres above the boundary layer, compared with the pre-convective situation. The satellite picture at 1500 UTC shows that convective development did occur at greater distances from the original storm cluster that were unaffected by the effects of its warm, dry downdraught.

3.8 Discussion and conclusions

During PRINCE, the coordinated deployment of remote sensing systems with in-situ measurements was effective in revealing processes taking place during the life-cycle of a convective storm cluster. The question of why convection ensued where it did can be answered only partially. Data from the ECMWF IFS and radiosondes suggest that the approach of an upper-tropospheric potential vorticity anomaly caused upward vertical motion that cooled the warm air capping the boundary layer the day before. The Doppler lidar shows that a weak, but well-developed local circulation existed over the western slope of Hornsgrinde. High-resolution aerosol and cloud data by the Raman lidar in the pre-convective environment revealed the existence of lower tropospheric undulations, whose exact influence on convective initiation remains unclear at this time. Mass convergence was observed to the east of the summit in association with the initiation of a convective updraught in which hydrometeors developed that were detected by the C-band radar. An example of the influence the environment of the storms has had on the storm evolution is the interaction with the stable layer at around 5 km altitude, which constrained the depth of the western storm for a short time. The spreading out of a cloud deck at this altitude can be explained by the finding that where the thermal buoyancy of a convective updraught decreases with height, detrainment, i.e. horizontal divergence of the flow is to be expected.

More importantly, however, the study has shown how a storm changed its low-level environment. The analysis of the various measurements indicates that a warm downdraught, with a diameter on the order of 10 km, formed under the decaying parts of the storm system. Its relative dryness, high temperature, and positive thermal buoyancy imply that cooling by evaporation of hydrometeors can be ruled out as the major forcing of the downward motion. Instead, it has primarily been a manifestation of the compensation of the upward mass flux in nearby convective updraughts. Although most convective parameterization schemes take the warming and drying influence of such downdraughts into account (e.g. Kain and Fritsch, 1990), observations of warming and drying in the lower troposphere have, to our knowledge, not yet been documented. Observations of warm downdraughts in the vicinity of convective storms at higher altitudes are presented by Fritsch, 1975, who discusses observations made in the vicinity of severe storms at altitudes between 9 and 10 km AGL. The downward velocity within those was up to 5 m s^{-1} , and the entire downdraught had a horizontal extent of 13 km distance from the edge of the storm cloud. Yuter and Houze Jr., 1995, in a study of (sub-)tropical thunderstorms across Florida, make a distinction between upper-level and lower-level downdraughts, that have distinct dynamical origins. The upper-level downdraughts are caused by pressure gradient forces required to maintain mass continuity in the vicinity of updraughts, and lower-level downdraughts are caused by evaporation of precipitation. This paper complements these observations by demonstrating that such downdraughts may extend into the lower troposphere above the boundary layer, where they spread out and can cause significant inhibition to new convective initiation.

Chapter 4

Convection in strong vertical wind shear

Vertical wind shear has an important influence on convection. Its effects can best be understood by considering the perturbations in the pressure field that result from it. In a vertically-sheared flow, horizontal velocities are, per definition, different at each altitude. When air within a convective up- or downdraught changes altitude, the air will gradually adjust its horizontal velocity to that present at its new altitude. In order to accomplish that, horizontal pressure forces will develop, which induce the required horizontal acceleration.

It is reiterated that the dynamic perturbation pressure is the solution of

$$-\frac{1}{\rho_0} \nabla^2 p'_d = \frac{\partial u_i}{\partial x_j} \frac{\partial u_j}{\partial x_i} \quad (4.1)$$

Writing out this rather compact notation yields

$$-\frac{1}{\rho_0} \nabla^2 p'_d = \left(\frac{\partial u}{\partial x} \right)^2 + \left(\frac{\partial v}{\partial y} \right)^2 + \left(\frac{\partial w}{\partial z} \right)^2 + 2 \frac{\partial u}{\partial y} \frac{\partial v}{\partial x} + 2 \frac{\partial u}{\partial z} \frac{\partial w}{\partial x} + 2 \frac{\partial v}{\partial z} \frac{\partial w}{\partial y} \quad (4.2)$$

One can study the behaviour of these dynamic pressure perturbation terms of convection in a sheared flow, by considering the effects of small perturbations on a vertically sheared background flow without vertical motion (Rotunno and Klemp, 1982; Klemp, 1987; Bluestein, 1993), viz.

$$\mathbf{v} = \begin{pmatrix} U(z) + u' \\ V(z) + v' \\ w' \end{pmatrix} \quad (4.3)$$

which upon substitution yields

$$\begin{aligned} -\frac{1}{\rho_0} \nabla^2 p'_d = & \left(\frac{\partial u'}{\partial x} \right)^2 + \left(\frac{\partial v'}{\partial y} \right)^2 + \left(\frac{\partial w'}{\partial z} \right)^2 + 2 \frac{\partial U}{\partial z} \frac{\partial w'}{\partial x} + 2 \frac{\partial V}{\partial z} \frac{\partial w'}{\partial y} + \\ & 2 \frac{\partial u'}{\partial y} \frac{\partial v'}{\partial x} + 2 \frac{\partial u'}{\partial z} \frac{\partial w'}{\partial x} + 2 \frac{\partial v'}{\partial z} \frac{\partial w'}{\partial y} \end{aligned} \quad (4.4)$$

If we consider $u' \ll U$ and $v' \ll V$, which will be the case when the flow perturbation is small, we can assume that two terms in 4.4, that are linear in the primed variables, rather than quadratic, will dominate, viz.

$$-\frac{1}{\rho_0} \nabla^2 p'_d = 2 \frac{\partial U}{\partial z} \frac{\partial w'}{\partial x} + 2 \frac{\partial V}{\partial z} \frac{\partial w'}{\partial y} \quad (4.5)$$

or in a perhaps more insightful way, where we make the assumption that the effect of the Laplacian is similar to that of a minus sign

$$p'_{d,linear} \sim \frac{\partial \mathbf{V}}{\partial z} \cdot \nabla_H w' \quad (4.6)$$

where $\mathbf{V} = (U(z), V(z), 0)$ and $\nabla_H = (\frac{\partial}{\partial x}, \frac{\partial}{\partial y}, 0)$. One can see that where the vertical shear vector $\frac{\partial \mathbf{V}}{\partial z}$ is directed in the direction of increasing upward motion, i.e. towards the core of an updraught or away from the core of a downdraught, a positive pressure perturbation can be expected. Down-shear of an updraught (or up-shear of a downdraught) a negative perturbation pressure can be expected.

4.1 Convection in unidirectional shear

The effects of pressure perturbations are different in different vertical profiles of the horizontal wind, and wind shear. In order to visualize the wind shear, a hodograph can be used, which is a parameter curve $u(z), v(z)$ projected on the x, y -plane. One can think of it as being a line swept out by the tip of the wind vector, as one moves vertically through the atmosphere. The shear vector $(\frac{\partial u}{\partial z}(z), \frac{\partial v}{\partial z}(z))$ at an altitude z is always parallel to the line tangent to the hodograph at that altitude.

An example of a straight-line hodograph is displayed in Fig. 4.1. In this case, the shear vector is west-southwesterly at every height, so that the shear is said to be *unidirectional*.

Linear pressure perturbations

The development of linear pressure perturbations with convection in unidirectional shear can be understood as follows. As air rises within an updraught in, for example westerly shear, as in Fig. 4.1, it will adjust to the increase in westerly momentum of the air in its environment, by increasing its own westerly momentum. This is brought about by a volume force which works in the direction of the shear vector. This force is a non-hydrostatic pressure gradient force between a local area of high perturbation pressure at the up-shear (here: western) side of the updraught, and an area of low perturbation at its down-shear (here: eastern) side. In Fig. 4.2, these two extrema of perturbation pressure are indicated by an H and L, respectively, and denoted by p'_L . In contrast, the force on a downdraught within this flow will experience a force pushing it westward, consistent with a local area perturbation pressure maximum at the down-shear (here: eastern) side, and a minimum on its up-shear (here: western) side. This prediction follows directly from the forcing term in Eq. 4.6. Typically, vertical velocity w' is greatest in the mid-troposphere so that the right-hand side of Eq. 4.6 can be expected to be largest somewhere in the mid-troposphere. This implies that vertical gradients of perturbation pressure must exist

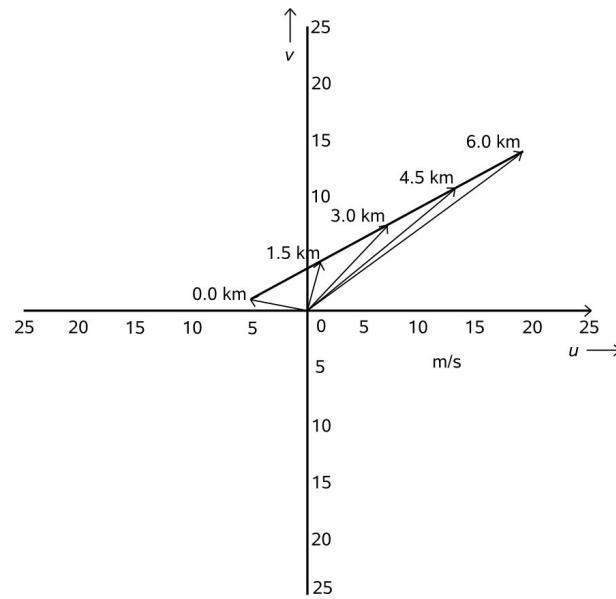


Figure 4.1: Hodograph showing a case of unidirectional wind shear with altitude. The wind vectors at 10 m (0.0 km), 1.5 km, 3.0 km, 4.5 km, and 6.0 km AGL are shown as arrows starting at the origin. The shear vector is tangent to the hodograph, and in this example west-southwesterly at all heights.

above and below this level. The volume forces that result from these gradients are called vertical perturbation pressure gradient forces (VPPGF). These induce vertical motions in the convective system, that are not induced by buoyancy, and have an impact on the evolution of a convective system. In the absence of low-level thermodynamic changes like cooling of low-level air by hydrometeor evaporation, updraughts tend to propagate in those directions where VPPGFs induce upward motion.

In the case of unidirectional shear, an upward VPPGF can be expected in the lower troposphere below the perturbation pressure minimum down-shear of a convective updraught. This area coincides with the location where most rain will normally occur, because of the down-shear transport of hydrometeors formed within the storm's updraught. The hydrometeors induce negative buoyancy both by their added weight ('water loading'), and especially by the cooling resulting from their evaporation into the unsaturated air through which they fall. As a result, the described linear effects are completely or partially compensated by negative buoyancy.

The linear effects also fail to explain observed and modelled behaviour of convective storms in unidirectional shear profiles, most importantly the splitting of storm updraughts into two separate updraughts that move into different directions.

Non-linear pressure perturbations

In order to explain updraught splitting, we turn to the non-linear terms of Eq. 4.4. To that aim, we write the Boussinesq momentum equation Eq. 3.2 with velocity split into a base state and perturbations upon that state (as done by Rotunno and Klemp, 1982):

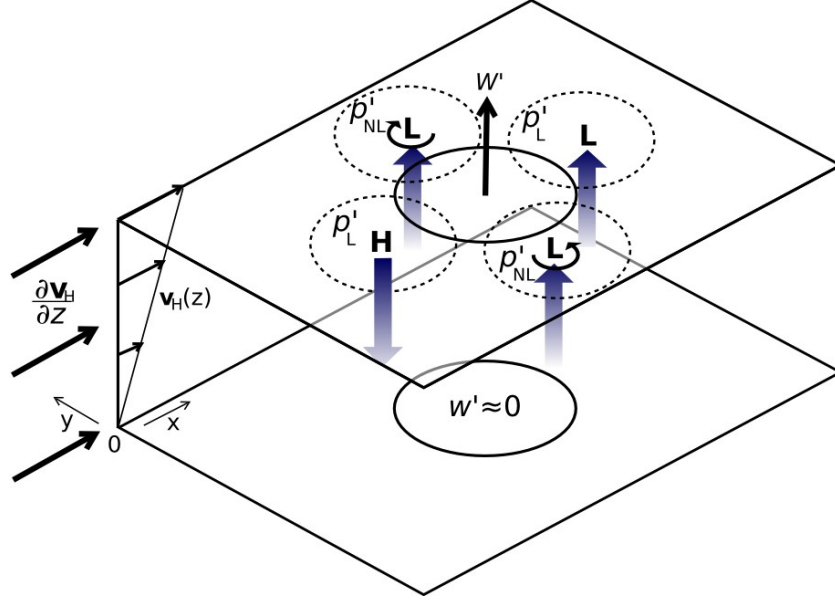


Figure 4.2: Linear and non-linear components of the perturbation pressures around an updraught in uni-directional vertical wind shear (based on a figure by Rotunno and Klemp, 1982). The lowest rectangle represents the earth's surface, and the top one represents an altitude at approximately halfway the updraught's depth. Vertical perturbation pressure gradient forces are indicated by vertical blue arrows. The upward vertical motion is maximized near the centre of the updraught area and gradually decreases at larger distances.

$$\frac{d\mathbf{v}'}{dt} + w' \frac{\partial \mathbf{V}}{\partial z} = -\frac{1}{\rho_0} \nabla p' + B_T \hat{\mathbf{k}} \quad (4.7)$$

where again the products of primed variables have been ignored, and $\mathbf{v}' = (u', v', w')$. From this equation, which is linear in the velocity perturbations, the non-linear effects in the pressure equation can be understood. When the operator $\hat{\mathbf{k}} \cdot \nabla \times$ is used on this equation, we obtain an expression for the rate of change of the vertical component of vorticity, $\zeta = \boldsymbol{\omega} \cdot \hat{\mathbf{k}} = \frac{\partial v'}{\partial x} - \frac{\partial u'}{\partial y}$:

$$\frac{d\zeta'}{dt} = \hat{\mathbf{k}} \cdot \left(\frac{\partial \mathbf{V}}{\partial z} \times \nabla w' \right) \quad (4.8)$$

This equation predicts that, when looking at an updraught along the environmental vertical shear vector, positive vorticity will develop on the updraught's right flank, and negative vorticity on its left flank, see Fig. 4.2. One can also infer that the vorticity will be largest where the product of the horizontal velocity gradient and the environmental shear is strongest, which is most likely the case somewhere in the mid-troposphere. Now, indeed such vorticity extrema have been observed in reality and in modelling studies as two counter-rotating vortices. It turns out that after a time, these vortices become strongly correlated with vertical velocity, at least in the lower half of the storm's depth.

This can be explained as a result of the tendency of pressure to be low wherever vorticity is high, as expressed by Eq. 3.6. In a horizontal cross-section through such a vortex cyclostrophic balance exists, i.e. a balance between inertia and a centripetal horizontal

pressure gradient force. However, in the vertical direction no such balance exists, and an upward-directed VPPGF exists below the perturbation pressure minimum that causes an upward acceleration of the flow. Conversely, above the level of the perturbation pressure minimum, a downward directed VPPGF acts to slow down the upward motion. In this way, upward vertical velocity is enhanced below a mid-level vortex.

It must be noted that the above does not follow from the linearized perturbation pressure in Eq. 4.6, and, hence, is a non-linear effect. The effect of vorticity around a vertical axis is in fact represented by the fourth term in 4.2 and in 4.4. It must be concluded that the assumption that $u' \ll U$ and $v' \ll V$ apparently loses its validity rather soon after the initial introduction of a buoyancy perturbation. The above interpretation was developed by Rotunno and Klemp, 1982, who have compared the contributions of the pressure perturbations due to linear effects and to non-linear terms in 4.4.

The enhancement of updraughts on the two lateral flanks usually leads to the splitting of storms. This effect is further enhanced by the development of negative buoyancy in the centre of the former updraught as a result of precipitation loading, and cooling of the air due to its evaporation below cloud base (e.g. Klemp, 1987). As a result of the enhancements of updraughts to the left and right of the shear vector, the two storms have a component of propagation perpendicular to the the mean shear vector. Their total propagation vector \mathbf{c} can be estimated by adding an across-shear propagation component to a vertically averaged mean wind across approximately the lower half of the storm. This has been the basis for a relatively successful method to predict the propagation vector of rotating storms, the internal-dynamics or ID-method by Bunkers et al. (2000).

4.2 Convection in shear turning with height

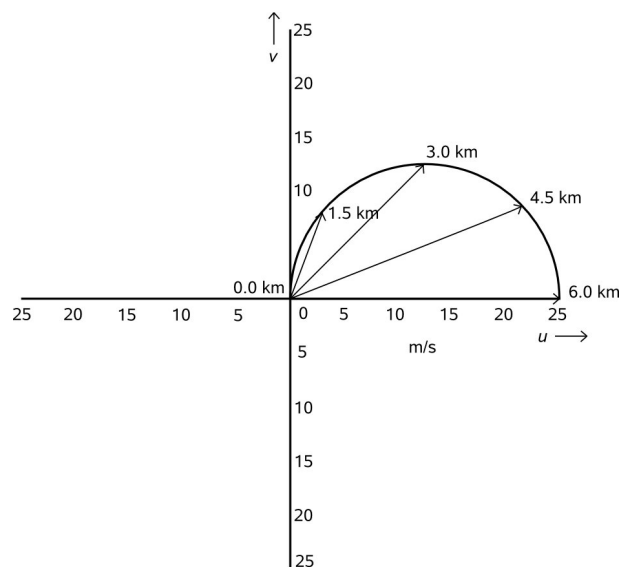


Figure 4.3: Hodograph showing a case of turning wind shear (and wind direction) with altitude. The wind vectors at 10 m (0.0 km, zero vector), 1.5 km, 3.0 km, 4.5 km, and 6.0 km AGL are shown as arrows starting at the origin. The shear vector is tangent to the hodograph, and turns from southerly via westerly to northerly in this example.

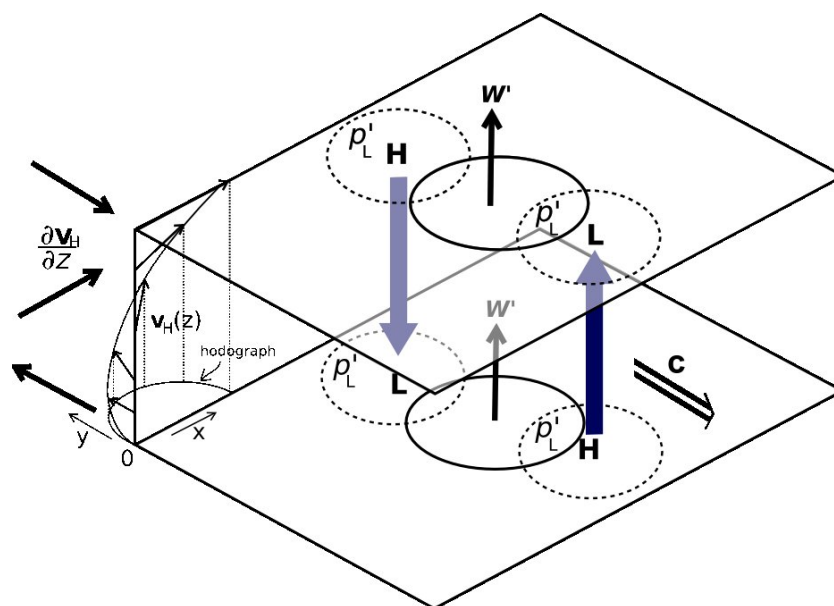


Figure 4.4: Linear perturbation pressures around an updraught in shear (and wind) turning with height (based on a figure by Rotunno and Klemp, 1982). The lowest rectangle represents the earth's surface and the top one represents an altitude at approximately halfway the updraught's depth. The hodograph is the projection of the tips of the wind vectors onto the x, y -plane, and is drawn in the left of the figure. The picture shows a case in which the hodograph has the shape of a half circle, starting in the origin.

In contrast to the unidirectional shear situation discussed above, *linear* perturbation pressure plays a major role in storm propagation in the case of curved hodographs. It has been explained that linear perturbation pressure causes a couplet of positive and negative perturbation pressure to develop up-shear and down-shear of an updraught, respectively. When wind shear turns with height, so will the locations of the linear perturbation pressure extrema relative to the updraught. An example of a hodograph representing such a situation is given in Fig. 4.3. In this particular case, the shear vector veers from southerly via westerly to a northerly direction as one moves up through the troposphere. When, as is the case here, the shear vector turns by 180° , a low-level perturbation pressure maximum can become situated under a perturbation pressure minimum or vice versa. This is visualized in Fig. 4.4. The southerly shear at low levels induces high perturbation pressure to the south of the updraft, and low perturbation pressure to its north. Higher up, where the shear is northerly, the locations of the perturbation pressure extrema are reversed. In that case, relatively strong vertical gradients of perturbation pressure develop on the northern and southern flanks of the updraught. The effect of these vertical gradients is to enhance upward motion on the updraught's southern flank, and to counteract upward motion on its northern flank. These effects combined result in a propagation of the updraught towards the upward directed vertical perturbation pressure gradient force, i.e. the south. As a result, the storm system will develop a component of propagation \mathbf{c} in this direction.

As the updraught propagates into the direction of \mathbf{c} , it ingests a sheared flow. The vorticity associated with this sheared flow can be divided into a component perpendicular to the storm inflow, and a component parallel to the inflow. These are called *crosswise vorticity* and *streamwise vorticity*, respectively (Davies-Jones, 1984). Only the streamwise

component contributes to net updraught rotation. If we write the storm-relative flow as $\mathbf{v} - \mathbf{c}$, the streamwise component of vorticity is written as:

$$\omega_{streamwise} = \omega \cdot \frac{\mathbf{v} - \mathbf{c}}{\|\mathbf{v} - \mathbf{c}\|} \quad (4.9)$$

Upon multiplying this with the magnitude of the storm-relative flow $\|\mathbf{v} - \mathbf{c}\|$ we obtain a quantity coined storm-relative helicity (SRH), or, by some, storm-relative helicity density, which can be interpreted as the rate at which streamwise vorticity enters the updraught:

$$SRH = \omega \cdot (\mathbf{v} - \mathbf{c}) \quad (4.10)$$

This parameter has shown to be a relatively good predictor of *supercell* storm formation (e.g. Rasmussen, 2003; Thompson et al., 2003), where a *supercell* is defined as *a storm with a deep, persistent mesocyclone* (i.e. a mesoscale vortex with low pressure at its centre) (Doswell and Burgess, 1993).

For the curved-shear case we have now discussed the effects of the linear pressure perturbations. The non-linear effects are, however, not necessarily smaller or less important. Weisman and Rotunno (2000) have argued that analysis of their simulations revealed that the non-linear effects dominate not only for unidirectional shear profiles, but also for somewhat curved profiles. The observation that splitting updraughts also occur for curved hodographs indeed supports the notion that non-linear effects still plays a role. Davies-Jones (2002) demonstrates however that "for a storm in shear that turns markedly clockwise with height (...) linear shear-induced propagation (...) becomes the dominant mechanism". To this Rotunno and Weisman (2003) reiterate that their numerical simulations indicated that "the nonlinear contribution to the maintenance and propagation tendencies of the vertical pressure gradient is important for simulated storms under all hodograph curvatures". The statements of both parties in this discussion are not in contradiction with each other, as they both reflect that the non-linear terms are important for all hodographs, but that for strongly-curved hodographs the linear effects become bigger.

The discussion is relevant here, because it also addressed the importance of storm-relative helicity as a predictor of supercell dynamics. Weisman and Rotunno (2000) had several objections against this, because they regarded this parameter as an exponent of an analytical model of storm dynamics based on a Beltrami flow solution, in which linear terms are the ones responsible for storm propagation. Davies-Jones (2003b) argues, however, that this is a misunderstanding and that storm-relative helicity is not a characteristic number of Beltrami flow, nor that its applicability is limited to those storms that propagate through the linear perturbation pressure term effects. From now on it will be assumed that, indeed, the storm-relative helicity is a good metric for the potential of storm rotation. The strong relation between tornado occurrence and high values of storm-relative helicity found by e.g. Rasmussen (2003) and Thompson et al. (2003) clearly support this.

4.3 A Richardson Number

It has now been discussed what the role of wind shear, that exerts influence on the convection through dynamically induced pressure perturbations are. In order to quantify the

importance of dynamically induced pressure perturbations relative to buoyancy-induced pressure perturbations, a dimensionless number will be derived. The result is a formulation of the Bulk-Richardson number very similar to that defined by (Weisman and Klemp, 1982). The present new derivation however shows explicitly that the number represents the ratio of these two quantities.

To arrive at this point, the vertical momentum equation (Eq. 3.7) is reiterated:

$$\left(\frac{\partial}{\partial t} + \mathbf{v} \cdot \nabla\right)w = -\frac{1}{\rho_0} \frac{\partial p'_d}{\partial z} - \frac{1}{\rho_0} \frac{\partial p'_b}{\partial z} + B_T \quad (4.11)$$

On the left side, the total derivative of vertical velocity is found and on the right side terms that represent the acceleration. Now it is interesting to know the ratio between the magnitudes of the dynamic term $-\frac{1}{\rho_0} \frac{\partial p'_d}{\partial z}$ relative to the buoyancy terms $-\frac{1}{\rho_0} \frac{\partial p'_b}{\partial z} + B_T$. To that aim, a characteristic magnitude of each of the terms is looked for. To find the characteristic magnitude of p'_d , we refer to Eq. 4.1

$$-\frac{1}{\rho_0} \nabla^2 p'_d = \frac{\partial u_i}{\partial x_j} \frac{\partial u_j}{\partial x_i} \quad (4.12)$$

For a convective storm, horizontal and vertical length scales are of an equal order of magnitude. By the continuity equation, the horizontal and vertical components of velocity must also be of equal magnitude. If L is taken to be a characteristic length scale (10^4 m) and U a characteristic velocity scale (10 m s $^{-1}$), we can write

$$\begin{aligned} u_i &= u_i^* U \\ x_i &= x_i^* L \end{aligned}$$

where u_i^* and x_i^* are dimensionless and have an order of magnitude 1. The Laplacian can be decomposed in a similar way, viz.

$$\nabla^2 = \sum \frac{\partial^2}{\partial x_i^2} = \frac{1}{L^2} \sum \frac{\partial^2}{\partial x_i^{*2}} = \frac{1}{L^2} \nabla^{*2} \quad (4.13)$$

Upon substituting this the following relation is found

$$-\frac{1}{\rho_0} \frac{1}{L^2} \nabla^{*2} p'_d = \left(\frac{U^2}{L^2}\right) \frac{\partial u_i^*}{\partial x_j^*} \frac{\partial u_j^*}{\partial x_i^*} \quad (4.14)$$

Solving for p'_d , and taking all starred parameters as being unity, shows that p'_d scales as

$$p'_d \sim \rho_0 U^2 \quad (4.15)$$

In a similar way, to find the characteristic magnitude of p'_b ,

$$-\frac{1}{\rho_0} \nabla^2 p'_b = -\frac{\partial B_T}{\partial z} \quad (4.16)$$

and decomposing the buoyancy as $B_T = B^*B$, it is found that

$$p'_b \sim \rho_0 BL \quad (4.17)$$

where B is a characteristic thermal buoyancy. Applying these results, the characteristic magnitudes of the terms on the right-hand side of Eq. 4.11 can be found. For the first term

$$-\frac{1}{\rho_0} \frac{\partial p'_d}{\partial z} \sim \frac{U^2}{L} \quad (4.18)$$

and for the second and third terms combined

$$-\frac{1}{\rho_0} \frac{\partial p'_b}{\partial z} + B_T \sim B \quad (4.19)$$

The ratio between the magnitude of the buoyancy terms (the latter) and the dynamic term (the former) is therefore BL/U^2 .

Knowing that CAPE is a vertical integral of thermal buoyancy (cf. Eq. 2.14) and, therefore, scales as BL , we may also express the derived ratio in terms of CAPE. This ratio is a Richardson Number (Ri)

$$\text{Ri} = \frac{\text{CAPE}}{U^2} \quad (4.20)$$

The ratio also represents the amount of potential energy divided by the kinetic energy of the flow and is dimensionless (both the numerator and denominator have units of m^2s^{-2}). Taking the wind difference across approximately half of the sheared convective layer (estimated to be about 12 km deep), and introducing a factor $\frac{1}{2}$ in the denominator to arrive at the true expression of kinetic energy per mass $T = \frac{1}{2}v^2$, Weisman and Klemp (1982) arrived at a qualitatively similar quantity, the Bulk Richardson Number:

$$\text{BRN}_{WK} = \frac{\text{CAPE}}{\frac{1}{2} \|\mathbf{v}_{6km} - \mathbf{v}_{500m}\|^2} \quad (4.21)$$

The interpretation of denominator is that it represents kinetic energy viewed from a storm-relative reference frame. In the framework of a storm that moves with the tropospheric wind in the mid-troposphere, which is typically found around 6 km above the surface, the kinetic energy (per unit mass) of the low-level air is the difference between the storm's horizontal motion vector and that of the inflow air, squared.

Modelling studies show that for $\text{BRN}_{WK} > 50$, buoyancy dominates over shear and the influence of vertical wind shear is rather limited. Still, storm clusters will preferentially propagate into the direction where shear-induced pressure gradients enhance upward motion. For $\text{BRN}_{WK} < 50$, shear effects are relatively important, and long-lived rotating storms may result, that propagate in a relatively continuous manner. For $\text{BRN}_{WK} < 10$, shear-induced forces become even more important and may often dominate buoyancy-induced forces to such an extent that an organized convection updraught does not easily

develop. If it does, however, supercells are the likely convective mode. McCaul Jr and Weisman (1996) have found that in such shear-dominated supercells, the upward dynamic pressure gradient force may contribute three times as much to the maximum updraught speed as buoyancy.

The two cases presented in this work (the PRINCE case of Chapter 3, and the CSIP case that will follow in Chapter 5) have very different Bulk Richardson numbers. The PRINCE case had $\|\mathbf{v}_{6km} - \mathbf{v}_{500m}\| \approx 6 \text{ m s}^{-1}$ and $CAPE \approx 2000 \text{ m}^2 \text{ s}^{-2}$, yielding a BRN_{WK} of 110. The CSIP case had $\|\mathbf{v}_{6km} - \mathbf{v}_{500m}\| \approx 25 \text{ m s}^{-1}$ and $CAPE \approx 400 \text{ m}^2 \text{ s}^{-2}$ which gives a BRN_{WK} of 1.3.

Chapter 5

Observations and modelling of a storm in strong vertical wind shear



Figure 5.1: Map of England and Wales. Indicated are the cities and geographic features referred to in the text. The radiosonde observations used in the for the interpolation at 1200 UTC on 28 July 2006 are indicated by small black crosses, and surface stations by small grey squares.

Here, an analysis of observational data will be presented based on observations made during the field campaign of the Convective Storms Initiation Project (Browning et al., 2007), which includes data from the U.K. Met Office operational synoptic station network. On the day that will be discussed, several storms developed near and to the south of a zonally oriented warm front that moved northward across England during the day. One of those storms became rather intense upon crossing the frontal zone from the south and produced strong low-level rotation which resulted in a tornado that tracked across the city of Birmingham between 1300 and 1330 UTC, (Fig. 5.1). The tornado was rated F2 on the Fujita-scale (Fujita et al., 1972) and produced severe damage as it removed roofs from houses, and inflicting between 30 and 50 million pounds of damage (Marshall and

Robinson, 2006). Two additional weaker tornadoes occurred later that day near the city of Peterborough and the village of Moulton (ESSL, 2009). After discussing the observations, numerical simulations with the COSMO model (Schättler et al., 2007) at 1.1 km grid spacing will be presented. Specifically, an attempt will be made to identify the role of the warm frontal boundary and the origins of updraught rotation.

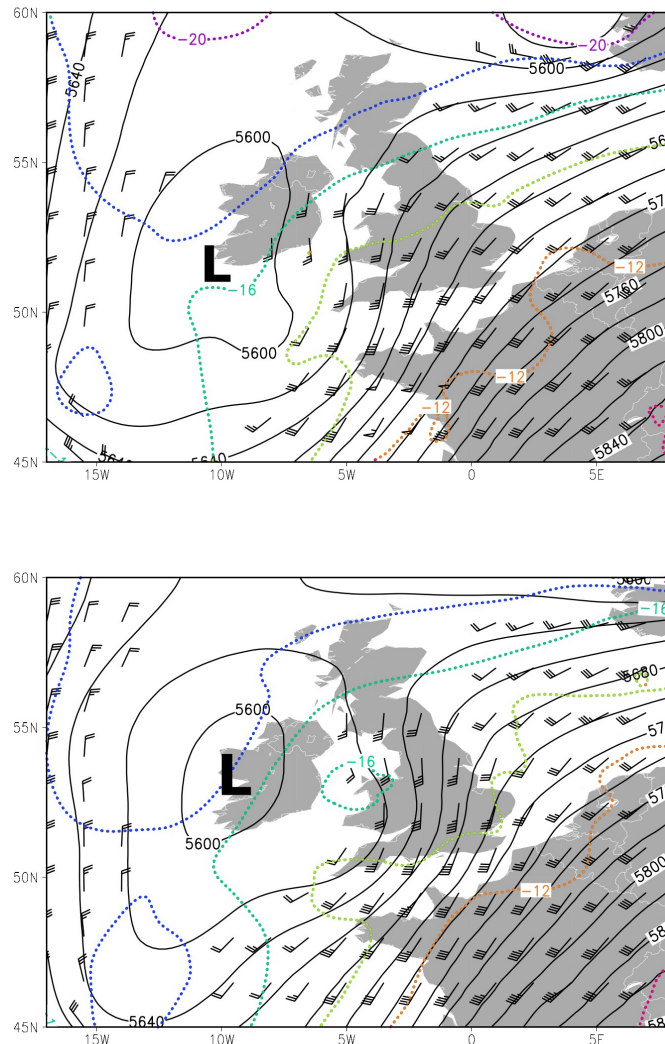


Figure 5.2: Operational analysis of the ECMWF model at 500 hPa, valid for 28 July 2005 at 0600 UTC (top) and 1200 UTC (bottom). Geopotential height (in geopotential metres) is shown with continuous contours, temperature ($^{\circ}\text{C}$) by dotted contours. Winds are plotted as conventional wind barbs were stronger than 10 m s^{-1} . Wind barbs are plotted as in Fig. 2.5.

5.1 Synoptic-scale introduction

On 28 July 2005, a moderately strong (around 20 m s^{-1}) southwesterly flow was present in the mid troposphere across western Europe. The ECMWF analysis presented in Fig. 5.2

shows that a short-wave trough at 0600 UTC was located from a point south of Ireland to Brittany. It moved into Britain during the subsequent 6 hours. At 1200 UTC it stretched from the Irish Sea across southern Wales into southern England. In the same period, a closed mid-level low over western Ireland moved little and became slightly less intense. Across the area of overall southwesterly flow, a temperature gradient was present, with the mid-level temperatures of near -10°C across the Alps and temperatures below -18°C to the west and southwest of Ireland.

A low at 850 hPa was located just west of Land's End and moved slowly northward into the southern Irish Sea between 0600 and 1200 UTC. The temperature gradients at this pressure level are stronger than at 500 hPa. One area with a particularly strong gradient can be identified, stretching in an east-westerly direction across central and later northern England, eastward across the North Sea into the German Bight. This gradient can be interpreted as the location of a warm frontal zone intersecting the 850 hPa pressure level. Winds with speeds around 10 m s^{-1} blow cyclonically around the low's centre, an exception being the English Channel region and southern England, where the south-southwesterly winds increase to near 20 m s^{-1} at 1200 UTC.

5.2 Analysis of the observations

Several observational data sets have been used for this case study. These include surface observations from the CSIP field campaign and operationally collected surface observations from the U.K. Met Office. Additionally, a large number of radiosondes, released both operationally and in the framework of CSIP, were available for analysis. The surface stations that were available for the analyses are plotted in Fig. 5.1. In addition to these data, the U.K. radar composite and visual satellite imagery have been used.

An overlay of satellite, radar and surface data at 0600 UTC is presented in Fig. 5.4. It shows an area of moderate to heavy rain located across the British Midlands, and more patchy areas of rain further west into Wales. The patchy appearance with spots of high local rainfall rates suggests that this rain was, in part, associated with convection. An intense convective rain shower (A) is located south of the city of Bath. A low boundary layer temperature with values in the 11 to 14°C range measured at 2 m across central England, did not allow for surface-based convection. Across southern England, the temperature was slightly higher with 2 m values between 16 and 18°C . The transition between those two areas is where the warm frontal zone that was identified in the 850 hPa ECMWF analysis, connects with the earth's surface.

During the morning, the warm frontal zone gradually became better defined and developed into a well-defined boundary between warm, moist air in the south and cool, nearly saturated air in the north (Fig. 5.5). Shower A becomes larger as it moves northeastward into the colder low-level air. The winds north of the boundary remain easterly, while the winds south of it veer to southerly directions. At 0900 UTC, an area with relatively little mid- and high-level cloudiness overspreads southern England from the southwest. In response, boundary layer convection intensifies and horizontal convective rolls aligned with the boundary-layer wind shear, develop. These rolls can be identified by the pattern of convective clouds that identify the updraught zones of the rolls (indicated by "HCR" in

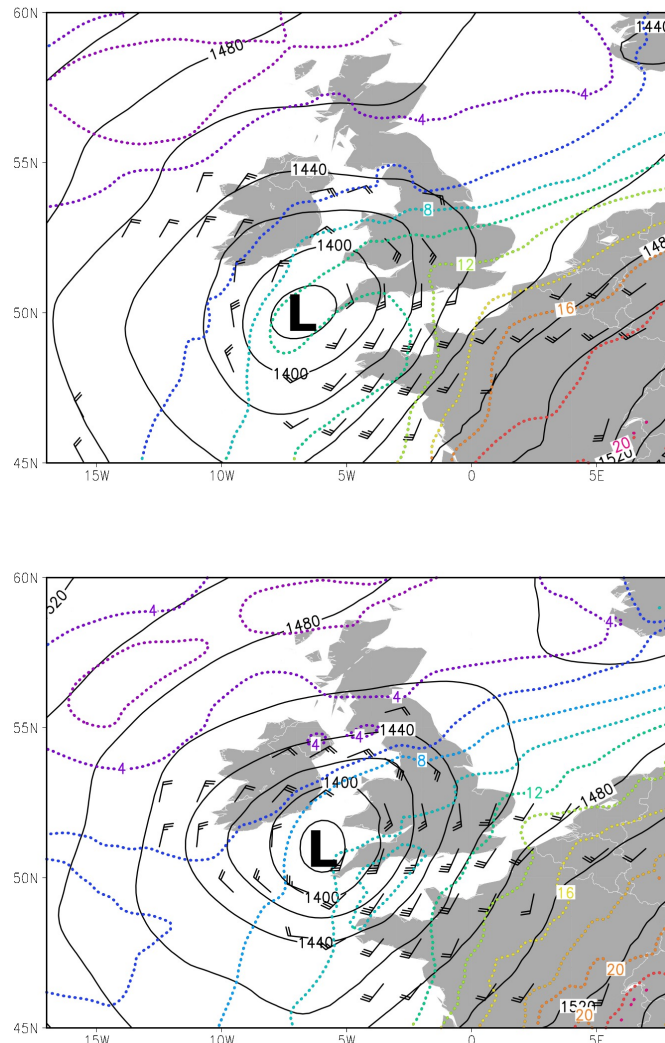


Figure 5.3: As in 5.2, but for 850 hPa.

Fig. 5.5). The radar composite indicates weak rainfall rates from parts of these cloud bands.

Around 1100 UTC (Fig. 5.6), showers start to develop more rapidly, both from the roll-induced convective clouds east of the Bristol Channel (these have been labelled B) and across southern Wales (these showers are labelled C). Two factors play a role in this development, one being the general warming of the boundary layer and the other being the approach of the mid- and upper-level trough, inducing upward vertical motion.

At 1200 UTC (Fig. 5.7), the cluster C has intensified further and moved northward. At the same time, the showers labelled B have clustered into a single storm, which is not extraordinarily intense.

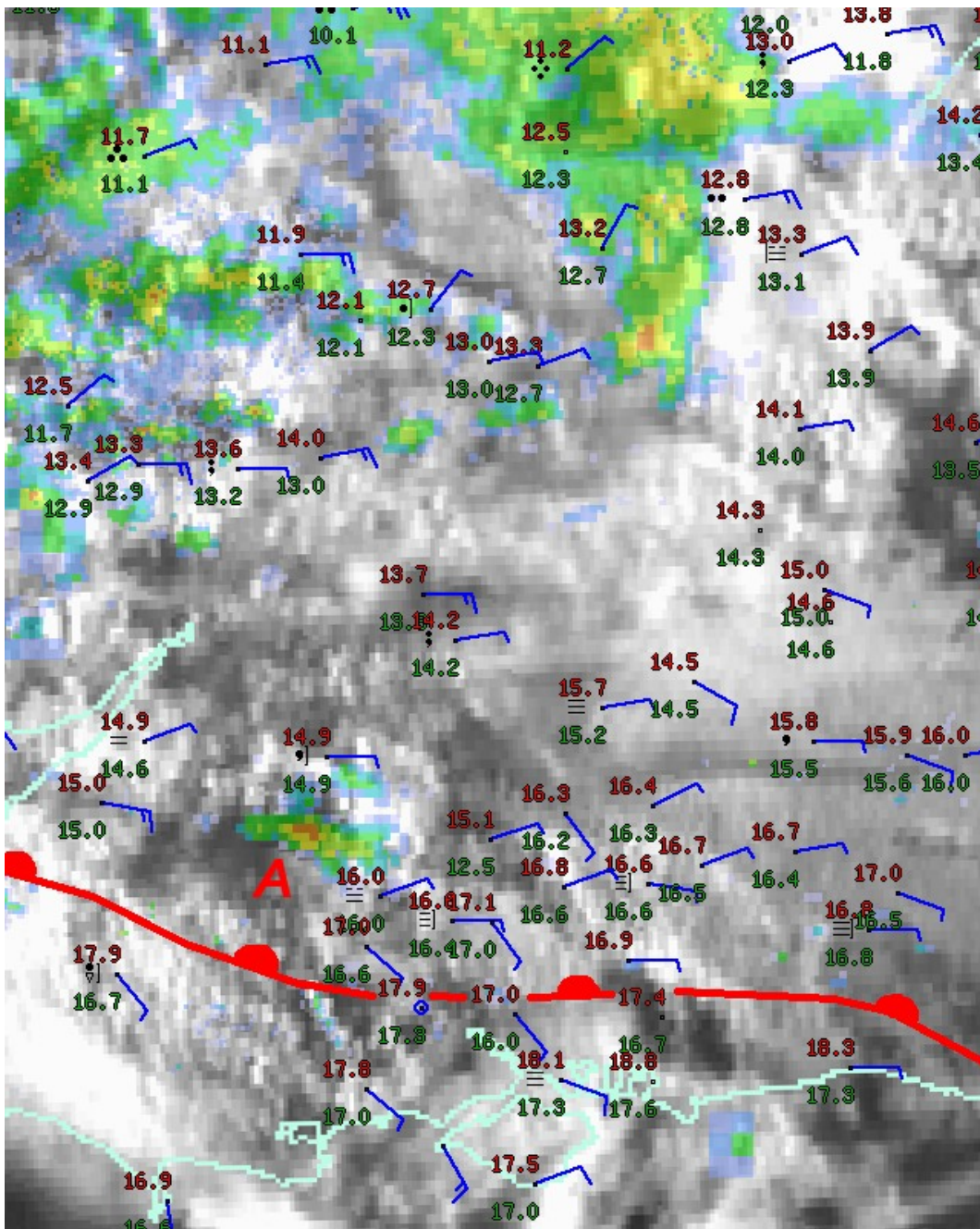


Figure 5.4: Surface data, radar and satellite image (VIS) at 0600 UTC, 28 July 2005 across southern England. Temperature measurements at 2 m AGL are given in red, dew point temperatures in green. Winds at 10 m AGL are plotted as described in Fig. 2.5. Current weather is plotted to the left of each station in conventional notation. The location of a warm front (line with half circles) is indicated.

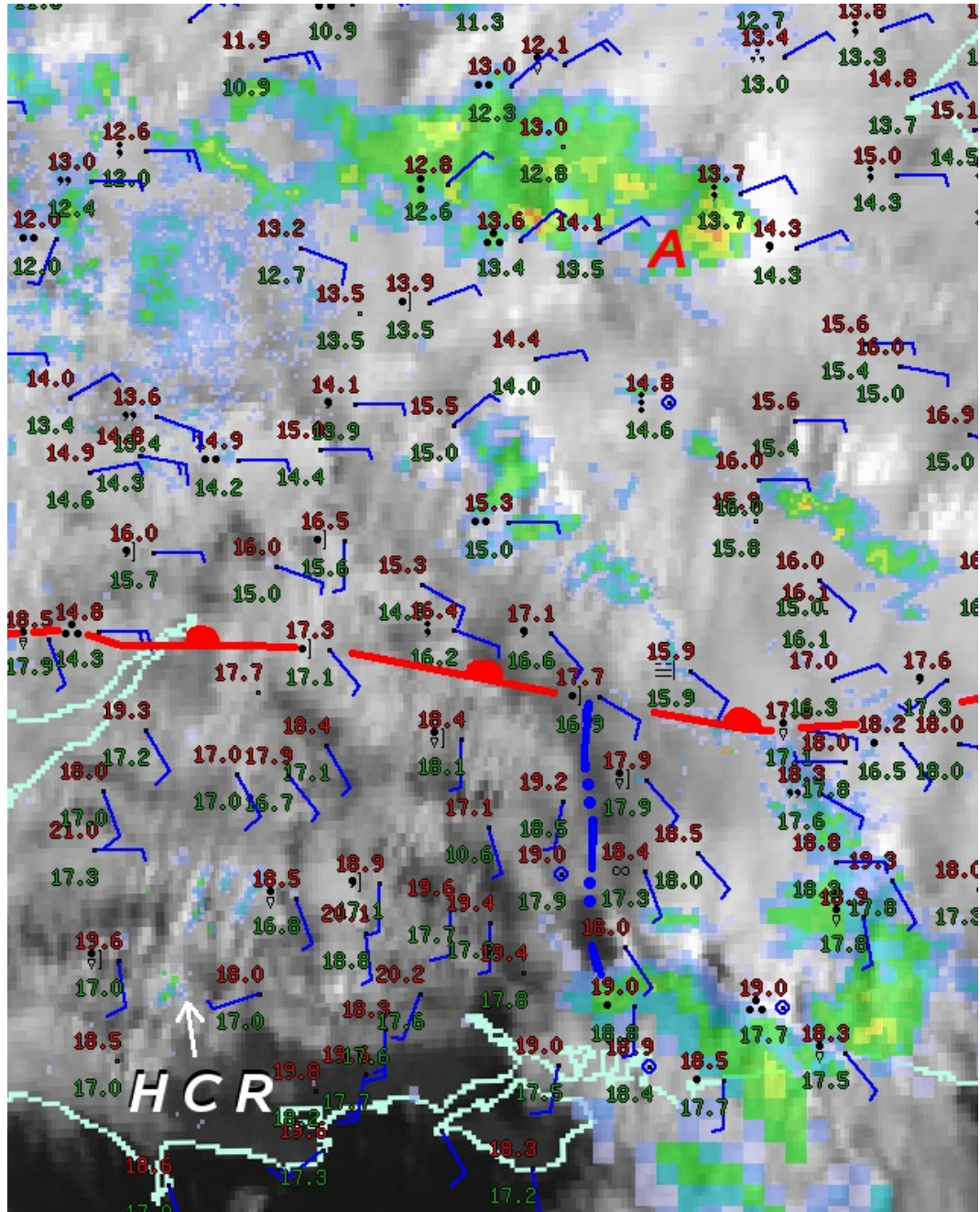


Figure 5.5: As Fig. 5.4, but for 0900 UTC.

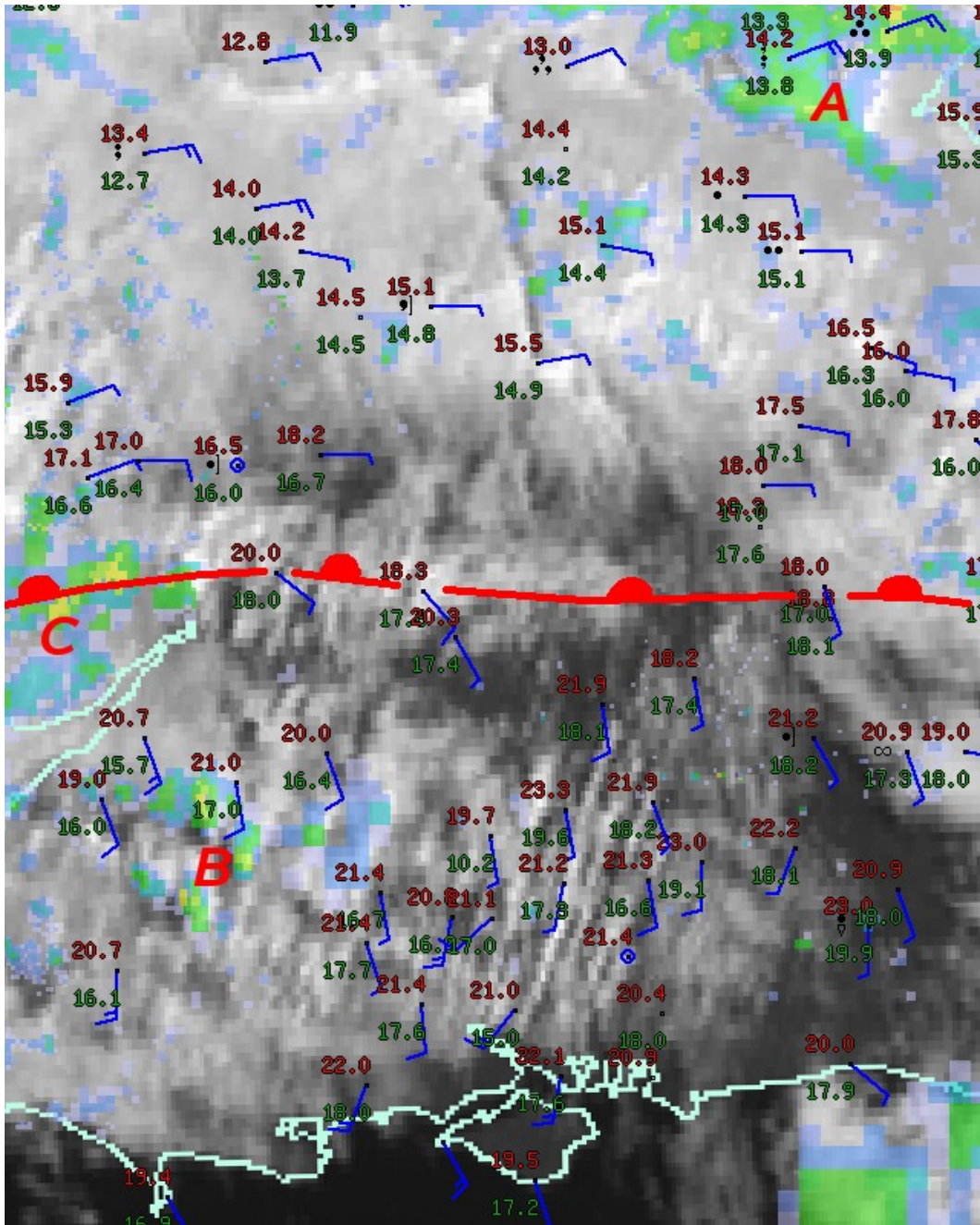


Figure 5.6: As Fig. 5.4, but for 1100 UTC. B refers to a cluster of showers that develops east of the Bristol Channel. C indicates the increased showers across southern Wales.

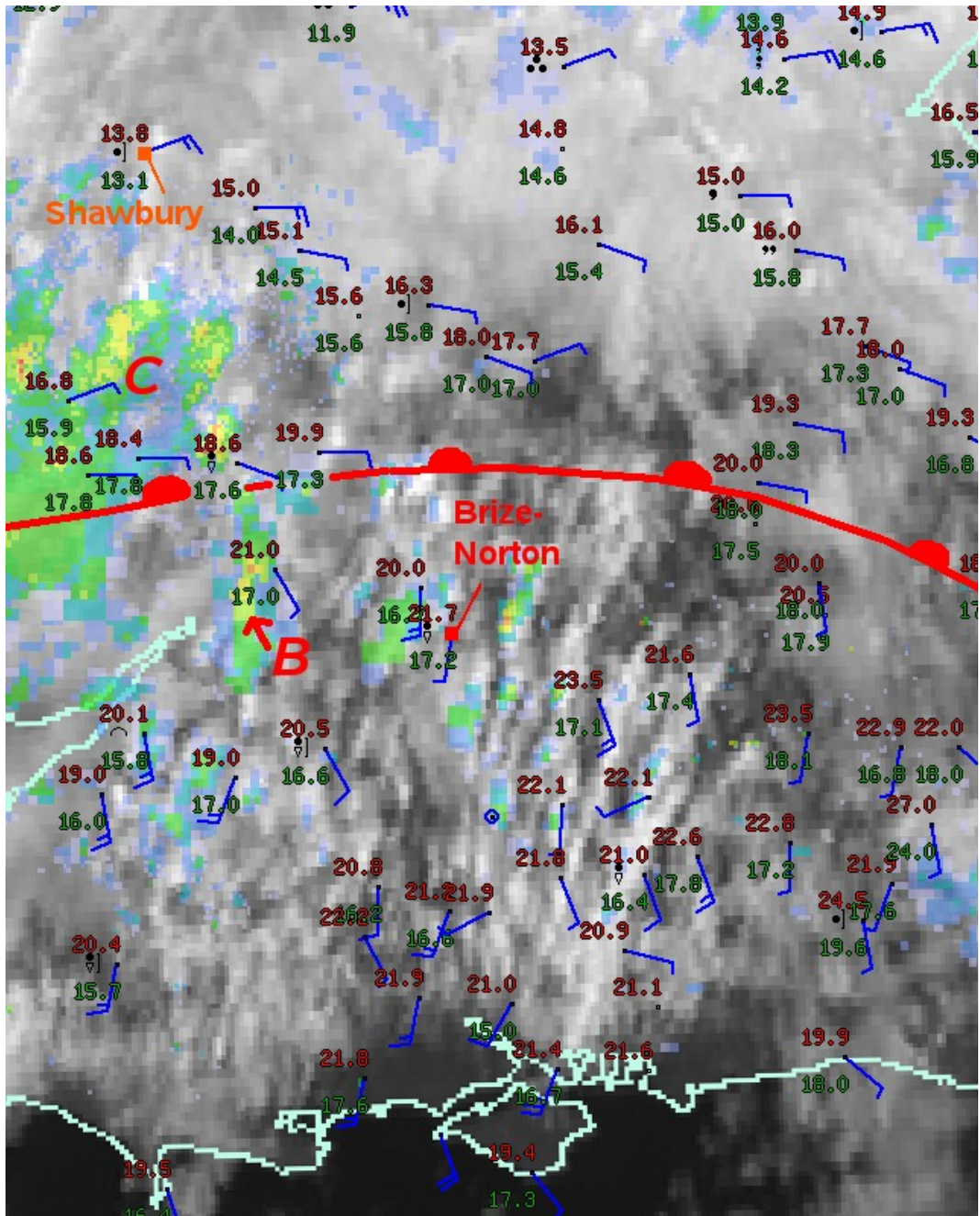


Figure 5.7: As Fig. 5.4, but for 1200 UTC.

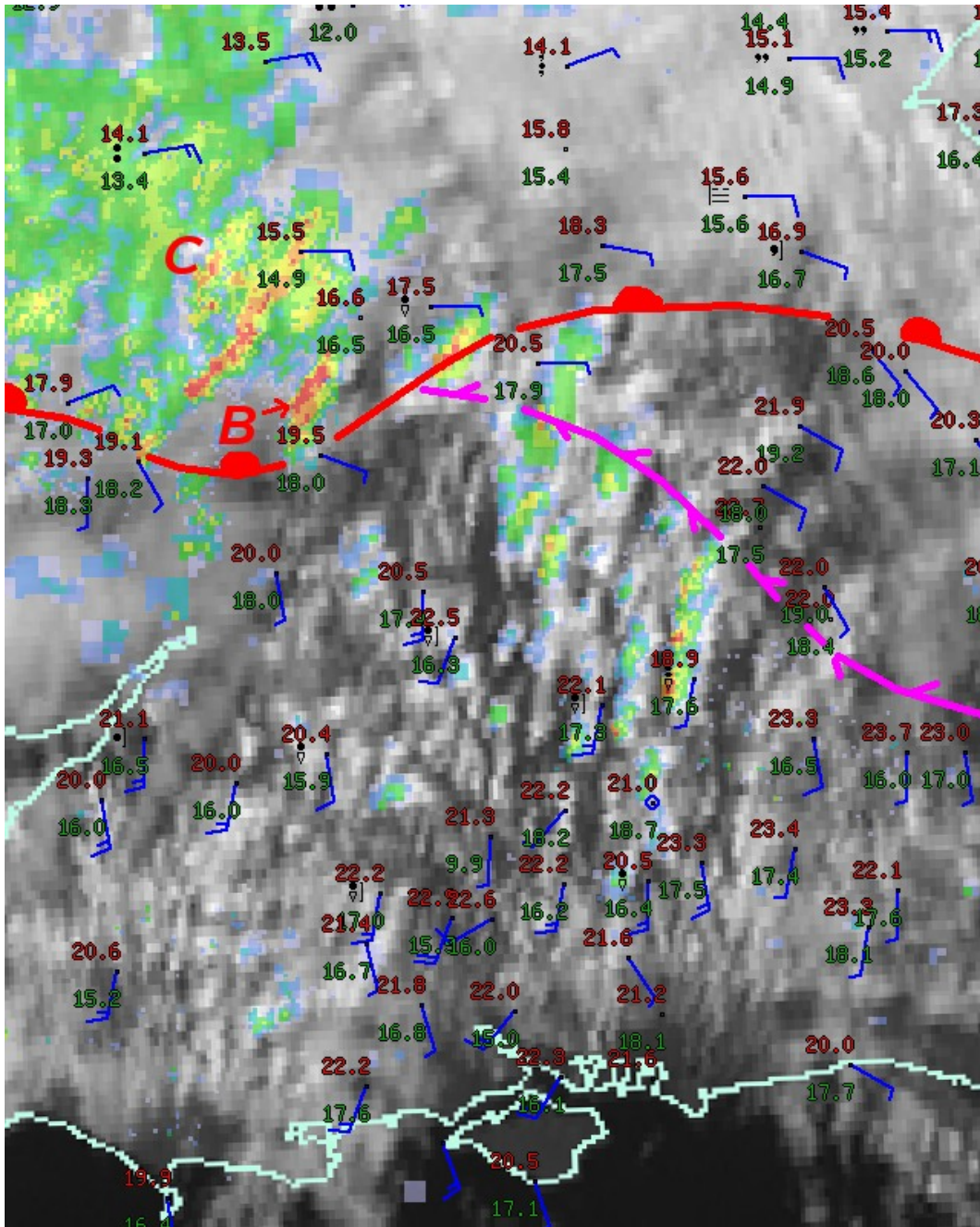


Figure 5.8: As Fig. 5.4, but for 1300 UTC. The figure contains a convergence line (purple).

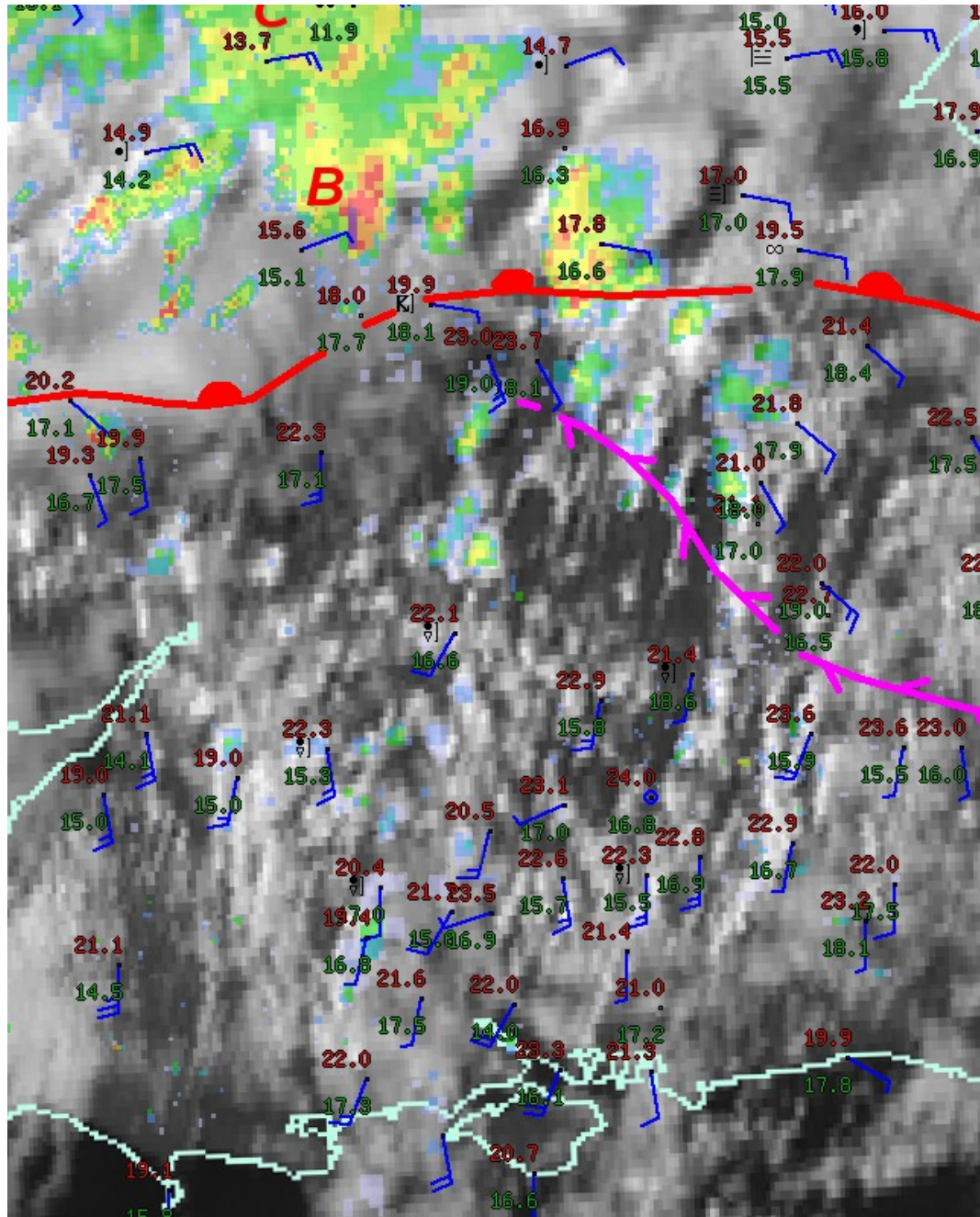


Figure 5.9: As Fig. 5.4, but for 1400 UTC. The figure contains a convergence line (purple).

The observations at 1300 UTC (Fig. 5.8) suggest that the surface warm front accelerates its northward movement except in the wake of storm cluster C, where the front lags a few 10s of kilometres behind. This can be explained by the relatively weak insolation and production of cold low-level air by hydrometeor evaporation in the range of the cluster. Additionally a second zone of surface wind convergence appears to have formed south of the warm front. As a minor temperature discontinuity also exists across this boundary, one could argue that the original warm front has split into two frontal boundaries. The reason why this occurs is unclear.

The storm B and cluster C have intensified considerably. Cluster C is located north of the front where the 2 m temperature is below 16°C , which is too low to allow surface parcels to obtain positive thermal buoyancy. Storm B is crossing the surface warm front and produces the tornado in Birmingham between approximately 1300 and 1330 UTC.

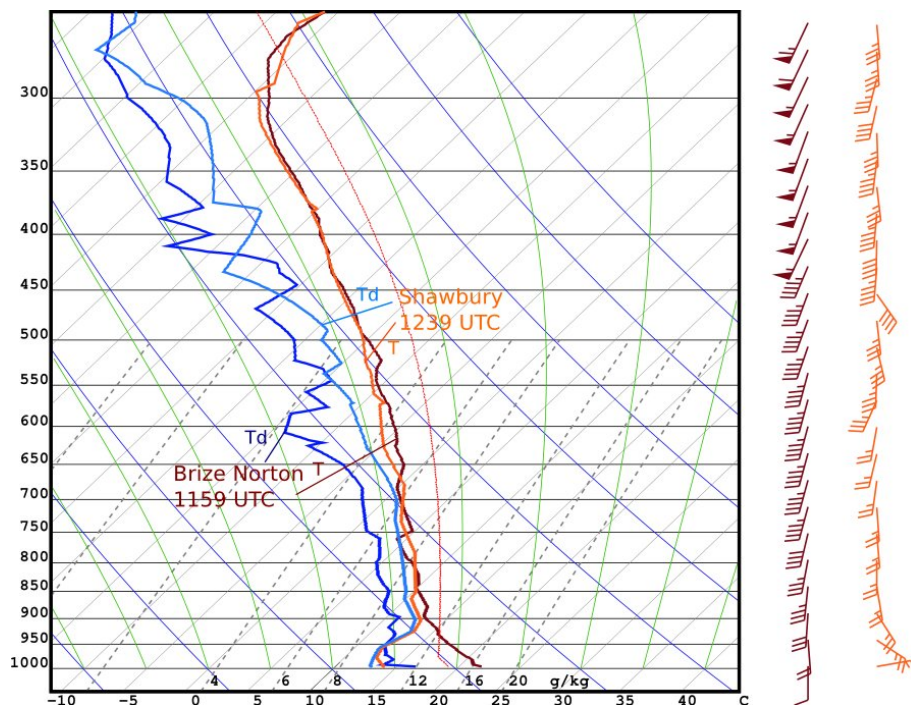


Figure 5.10: Temperature and moisture profiles of Brize-Norton at 1159 UTC and Shawbury at 1239 UTC on 25 July 2005, plotted into a Skew-T-log-p diagram. The red temperature curve is that of a parcel starting at the surface with an initial temperature of 19.5°C and a dew point temperature of 18.0°C , as was observed in the inflow of storm B at 1200 UTC. Wind barbs are plotted as in Fig. 2.5.

Fig. 5.10 shows the temperature and moisture profiles at Brize-Norton at 1159 UTC just south of the front, and Shawbury at 1239 UTC north of the front (see Fig. 5.1 or 5.7 for the respective locations of these stations). The thick dark red (dark blue) and orange (light blue) lines are the observed temperature (dew point temperature) profiles from Brize-Norton, south of the front, and Shawbury, north of the front, respectively. The Shawbury sounding does not exhibit any CAPE for air parcels near the surface for it indicates a stably stratified lowest kilometre, with temperatures of $13\text{--}14^{\circ}\text{C}$ throughout this layer. The Brize-Norton sounding, however, shows an approximately dry-adiabatic lapse rate up to nearly 1 km or 900 hPa. This suggests that a well-mixed convective boundary layer was

in place. Above the lowest kilometre, both soundings are rather similar, following a nearly moist-adiabatic lapse rate.

In the case of the Brize Norton sounding, a parcel rising from the surface with the observed temperature and dew point temperature at 2 m of 21.7°C and 17.2°C, respectively, would become positively buoyant rather soon. However, since the high surface dew point is only present in a very shallow surface layer, it can be speculated that the actual radiosonde was released in or near the downward branch of a horizontal convective roll, as these produce the greatest vertical gradients of moisture in the lower boundary layer.



Figure 5.11: Photograph of the tornado as it tracks through Birmingham on 25 July 2005, some time between 1300 and 1330 UTC. Source: Birmingham City Council.

The direct environment of the developing storm was rather well sampled by an observation made a few kilometres to the east of its representation on radar at 1300 UTC. This station measured weak east-southeasterly winds, a temperature of 19.5°C, and a dew point temperature of 18.0°C (Fig. 5.8). Despite the fact that the temperature is lower here than in Brize Norton, this corresponds to an almost equal equivalent potential temperature (θ_e), because of the slightly richer low-level moisture present here. The ascent curve of a parcel lifted off the earth's surface with these values is plotted in Fig. 5.10. This parcel would have had a CAPE of 832 J kg⁻¹ (using the Brize Norton profile as a background profile above 1 km AGL), and a cloud base at about 200 m AGL. Often, temperature and humidity measurements at 2 m AGL are not thought to be very representative of the properties of a storm inflow. For example, Craven et al. (2002) found that predictions of cloud base height using surface data consistently underestimate cloud base height. Photographs of the storm itself (Fig. 5.11) suggest that the cloud base was likely lower than 200 m AGL rather than higher. Naturally, in and close to the tornadic vortex, the cloud base was much lower and in contact with the ground as a result of the local pressure deficit. Based on this observation, one can assume that the surface-based CAPE value of 832 J kg⁻¹ could be a realistic estimate of the actual energy being released in the storm's updraught. Of that amount, 233 J kg⁻¹ would be released below 3 km AGL. At 1400 UTC (Fig. 5.9), after the tornado disappeared, storm B moves off the frontal boundary northward into cooler air. It

is likely that the storm stopped to ingest near surface air, as this air would gradually need to overcome more and more convective inhibition. For example, a surface parcel with the 2 m temperature and moisture of 15.6°C and 15.1°C, respectively, as measured near the storm at 1400 UTC, would only have 53 J kg⁻¹ of CAPE left.

In order to investigate the observed distribution of instability and wind shear more in detail, the surface and radiosonde data have been interpolated on a 3-dimensional grid with a mesh size of 0.1 degrees of latitude and 0.2 degrees of longitude horizontally, and 10 hPa in the vertical. The surface stations of which the data has been used are shown in Fig. 5.1. The data shown in Figs. 5.12–5.14 all represent the situation at 1200 UTC. For the vertical interpolation, all data from sondes released between 1115 UTC and 1239 UTC have been used. The surface data and radiosonde data have been interpolated separately. From each vertical profile measured by a radiosonde, the data was extracted at a series of pressure levels, namely every 10 hPa. For each pressure level, the data were subsequently interpolated horizontally. For the horizontal interpolation, the Barnes scheme (Barnes, 1964) was used. For details about the interpolation, the reader is referred to Appendix B.

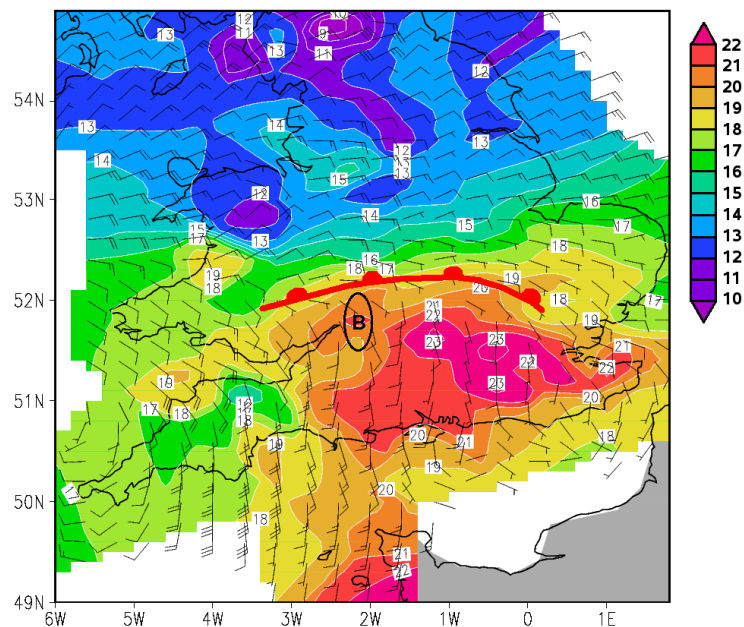


Figure 5.12: Interpolated 2 m temperature and 10 m wind field at 1200 UTC on 28 July 2005. Wind barbs are plotted as in Fig. 2.5. Overlain are the position of storm B and the warm front (red line with half circles towards the cooler air) at 1200 UTC.

The interpolated 2 m temperature and 10 m surface wind at 1200 UTC are depicted in Fig. 5.12. The location of the frontal zone can be recognized very well: it stretches from Wales eastward across central England.

Fig. 5.13 shows the interpolated 2 m dew point temperature and 10 m surface wind at 1200 UTC. A comparison with Fig. 5.12 shows that the largest gradients of moisture are present slightly to the north of where the largest temperature gradient occurs. In other words, within the warmer half of the frontal temperature gradient zone, low-level moisture already attains values similar to those much farther south. In fact, the dew point temperatures are even slightly higher within the frontal zone than further south. A local

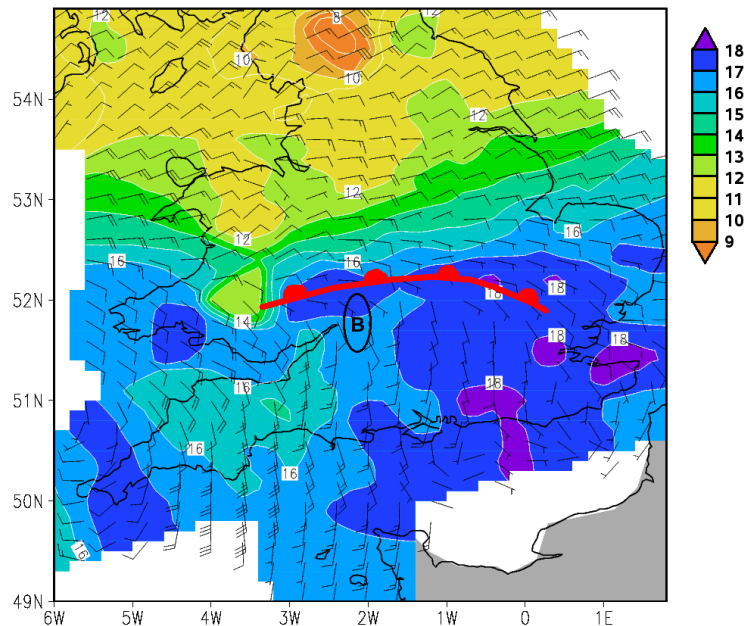


Figure 5.13: Interpolated 2 m dew point temperature and 10 m wind field at 1200 UTC on 28 July 2005. Wind barbs are plotted as in Fig. 2.5. Overlain are the position of storm B and the warm front (red line with half circles towards the cooler air) at 1200 UTC.

maximum of moisture is evident in and slightly to the south of where the storms B and the cluster of showers C were developing (cf. Fig. 5.7).

Now, using the three-dimensional data of the radiosondes, surface-based CAPE and storm-relative helicity have been calculated, and are shown in Fig. 5.14. These fields indicate that 0–3 km surface-based CAPE was maximized to the south of the frontal zone, whereas 0–1 km storm-relative helicity was maximized to the north. Within the frontal zone, an area existed that featured both considerable amounts of storm-relative helicity and surface-based CAPE. At 1200 UTC, this zone stretched from southern Wales across central England into East Anglia. The best overlap of the kinematic parameter storm-relative helicity, and the thermodynamic parameter CAPE was very near the location of storm system B at the time: just to the north and northeast of the Bristol Channel. As there was much less radiosonde data available later in the afternoon, it was, unfortunately, not possible to perform similar three-dimensional interpolations at other times.

5.3 Numerical simulation of the 28 July 2005 case with the COSMO model

In order to elucidate the role of the frontal boundary on the development of the storm, the regional numerical weather prediction model COSMO was run. A key question was whether it could reproduce a zone in which factors that are required for storm rotation overlap. These are strong low-level shear, preferably some storm-relative helicity, and, in any case, sufficient CAPE for storm development. Additionally, the question was raised whether the model was able to reproduce the development of a rotating convective updraught itself.

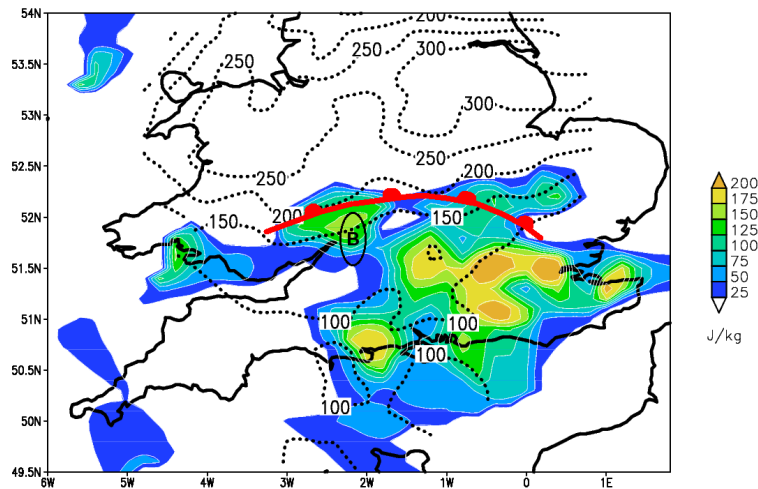


Figure 5.14: Interpolated storm-relative helicity in the 0–1 km layer in 10 m s^{-1} (dotted lines), and 0–3 km surface-based CAPE in J kg^{-1} (shaded) at 1200 UTC on 28 July 2005. Overlain are the position of storm B and the warm front (red line with half circles towards the cooler air) at 1200 UTC.

The simulation that was performed differs quite substantially from most other studies of severe storm development in that no idealized and horizontally homogeneous environment was used in this case. The present simulation was not forced by introducing a warm bubble. Furthermore, few researchers have focused on situations with amounts of CAPE as low as observed in this case, an exception being McCaul Jr and Weisman (1996), who studied storm development in environments characteristic of landfalling hurricanes.

5.3.1 Model description and setup

The numerical simulation was carried out using the COSMO model (Schättler et al., 2007). The model was formerly known as the "Lokal-Modell" (local model), and is a non-hydrostatic fully compressible model, developed and used by the Consortium for Small Scale Modelling (COSMO). It is used for meteorological studies on the mesoscale as well as for operational forecasting, for example at the German Weather Service (*Deutscher Wetterdienst*, DWD). The model uses a terrain-following coordinate system. Its computational grid is an Arakawa C-grid with Lorentz grid staggering vertically. Like similar models, it makes extensive use of parameterizations of sub-grid-scale processes.

It was decided to run the COSMO model (Version 4.0) on a 0.01° (approx. 1.1 km) grid, nested within a 0.05° (approx. 5.5 km) grid. Such a small grid spacing was chosen, because of the small sizes of the storms observed by radar, which was on the order of 5–10 kilometres. It was argued that if any storm-scale features were to be resolved, a grid spacing on the order of one kilometre would be necessary. Initial conditions and hourly boundary conditions for the finest grid were obtained from the 0.05° grid simulation. The configuration of the grid can be seen in Fig. 5.15. This simulation was run using 6-hourly operational ECMWF analyses that provided initial and boundary conditions. The ECMWF data were available on a 0.25° grid.

The choice was made to run the model with a configuration identical to that used in the

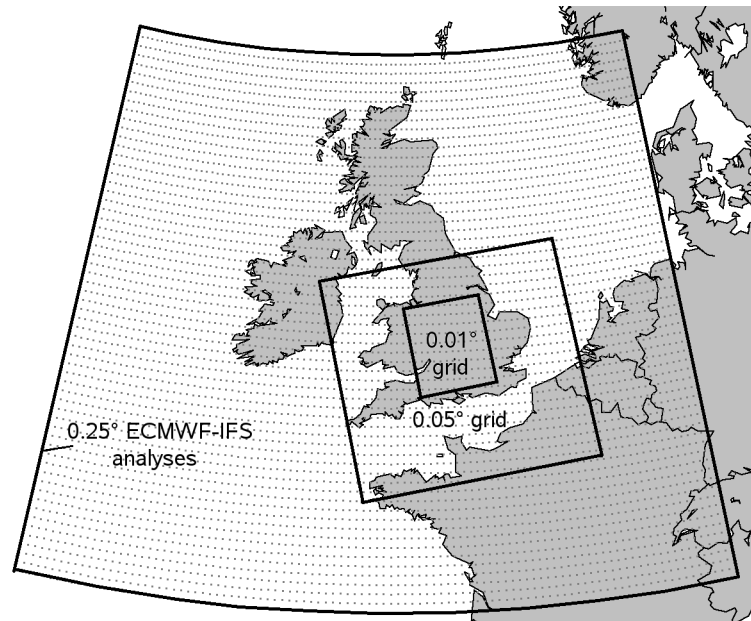


Figure 5.15: Nested model grids for the COSMO simulations. The outer grid shows the size of the available 0.25° ECMWF analyses, and the points of that grid, used to define the boundary conditions for the 0.05° grid, which covered southern Britain, the English Channel and northwest France. The smallest rectangle represents the 0.01° grid initialized with hourly boundary conditions from the 0.05° grid, and covers a large part of southern Great Britain.

DWD's COSMO-DE setup (as of 2009), except for the chosen domain and grid spacing. COSMO-DE is the name of the COSMO model in the configuration used at DWD for modelling on a 0.025° (approx. 2.8 km) grid covering Germany and adjacent regions. The basic settings that were used include

- 3rd order Runge-Kutta horizontally explicit, vertically implicit integration
- prognostic TKE-based turbulence scheme
- radiation parameterization according to Ritter and Geleyn (1992)
- multi-layer soil model (7 layers)
- parameterization for shallow convection only for the 0.01° run and with convective parameterization according to Tiedtke (1989) for the 0.05° run.

A number of recent changes in the COSMO-DE configuration were thus followed here as well. These include the switching off of the contribution of condensation of low clouds to the turbulence. The effect of this was to help mitigate an observed bias of too little and too late convective initiation in response to surface heating (Seifert et al., 2007). To the same aim, following another recommendation of Seifert et al. (2007), the maximum turbulent length scale was set to 150 m on this grid, instead of the 500 m used in the COSMO-DE configuration. The results of the simulation on the finest grid will now be discussed. The simulations on both grids were initiated on 28 July 2006 at 0000 UTC and stopped at 1800 UTC.

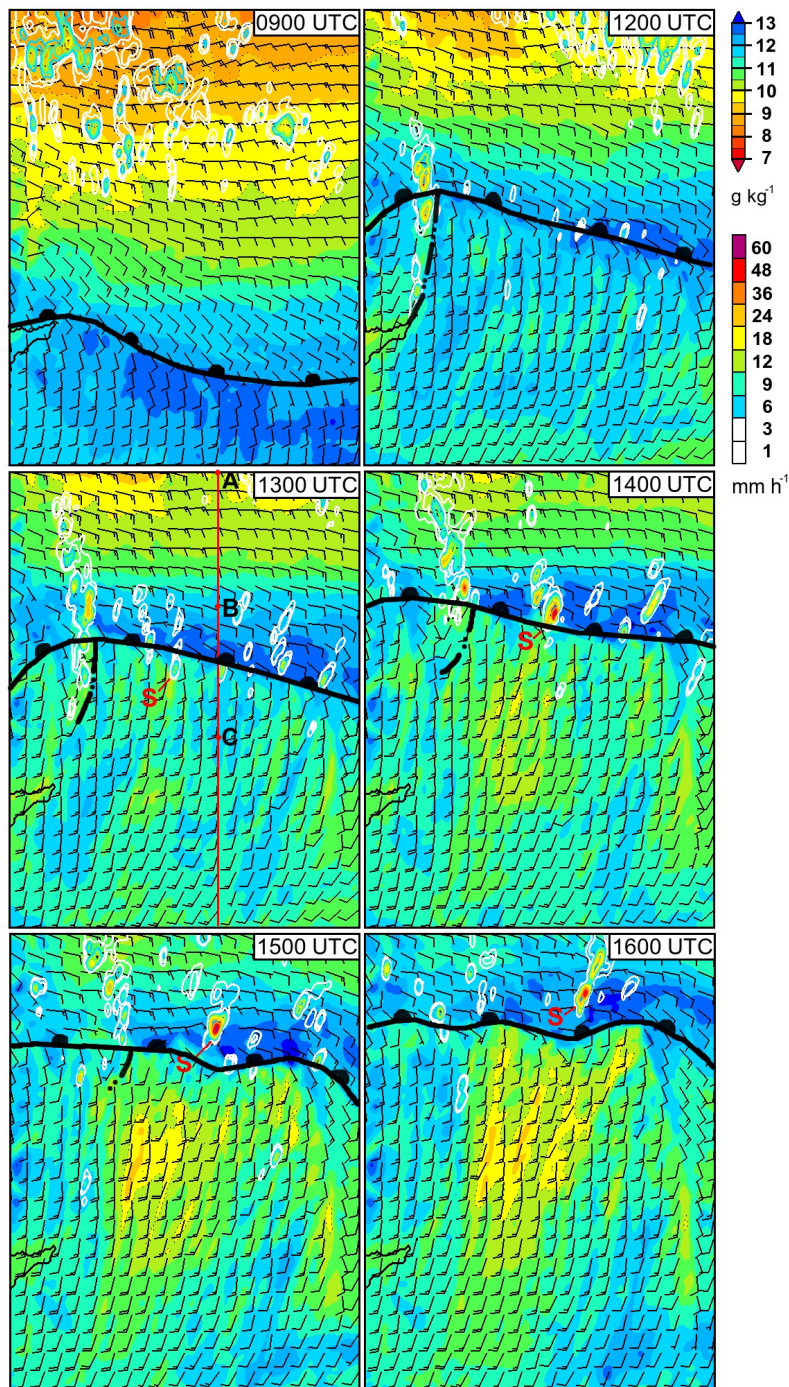


Figure 5.16: Output of the simulation with the COSMO model. Maps of the entire domain are shown for six different times. The following parameters are displayed: mixing ratio at 1000 hPa (shaded, background), 10 m AGL winds (according to the convention of Fig. 2.5.), and average precipitation rate during the 10 min before indicated time (thick contours). The locations of the warm front (line with half circles) and an outflow boundary (dashed-double dotted line) are indicated. The vertical line in the 1300 UTC map corresponds with the cross-section displayed in Fig. 5.18.

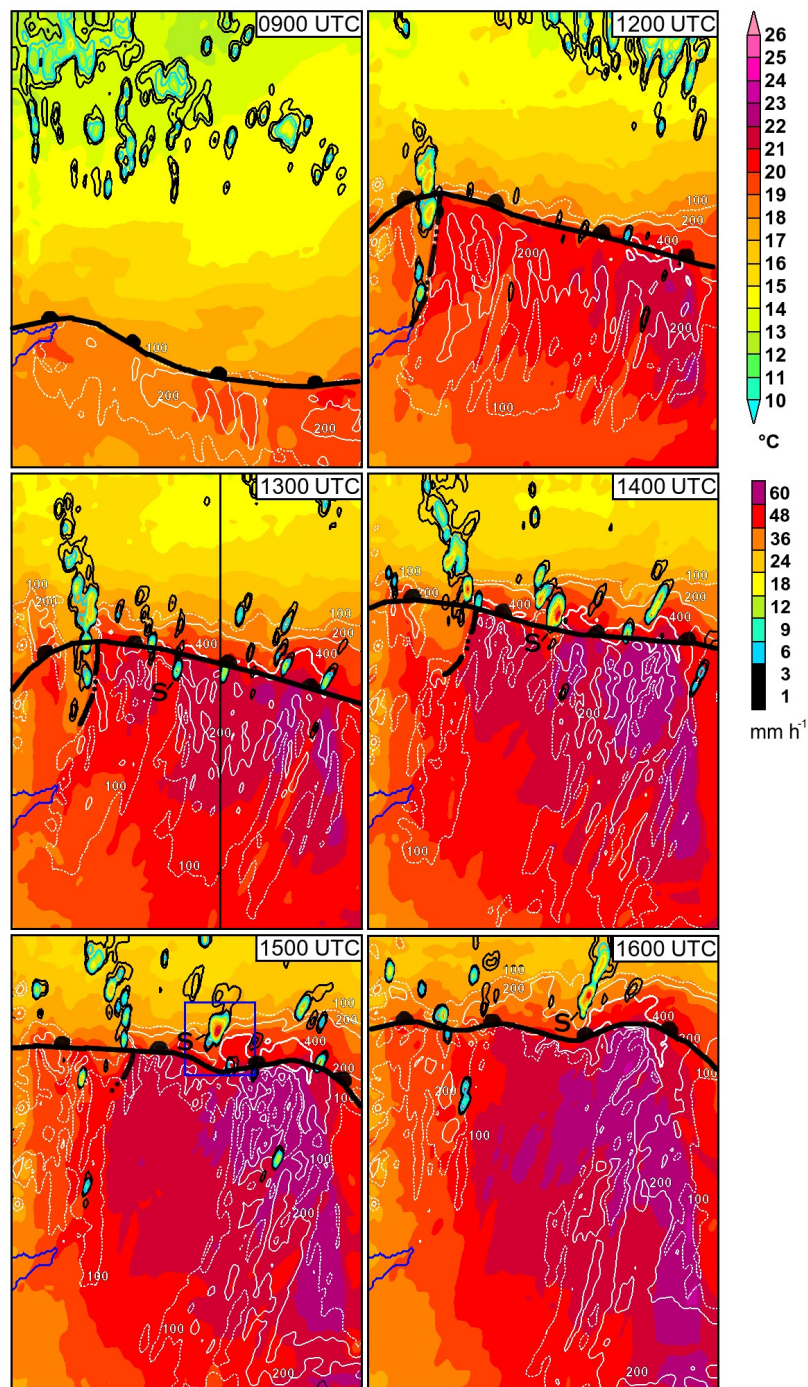


Figure 5.17: Output of the simulation with the COSMO model. Maps of the entire domain are shown for six different times during the integration. The following parameters are displayed: temperature at 1000 hPa (shaded, background), CAPE for a parcel lifted from the 1000 hPa level (in black lines: 100 J kg⁻¹: thin dashed line, 200 J kg⁻¹: thin solid line, 400 J kg⁻¹: thick solid line), and average precipitation rate during the 10 min before indicated time (thick contours). The locations of the warm front (line with half circles) and an outflow boundary (dashed-double dotted line) are indicated. The vertical line in the 1300 UTC map corresponds with the cross-section displayed in Fig. 5.18. The blue square in the 1500 UTC map corresponds with maps in Figs. 5.21 and 5.23.

5.3.2 Results

Fig. 5.16 shows the mixing ratio at 1000 hPa as shaded background colours. The 10 min-averaged precipitation rate is displayed with thick coloured contours. The barbs show the direction and strength of the wind at 10 m AGL. Fig. 5.17 shows the temperature at the 1000 hPa level as colours, the 10-minute averaged precipitation rate as in Fig. 5.16, and CAPE for a parcel lifted from the 1000 hPa in black lines.

At 0900 UTC, winds blow from the southeast to south in the southern third of the domain, whereas they are easterly further north. This appears to be in good agreement with the observations displayed in Fig. 5.5. It can be seen that the air in the southwestern part of the domain is moist with water vapour mixing ratio values around 12 g kg^{-1} at the 1000 hPa level, which is located very near the surface. This indeed is approximately equal to a dew point temperature of around 17°C which corresponds to the surface observations. At the same time, the air further north is considerably drier in an absolute sense, which is in accordance with observations. The model produced patches of rain across the northern half of the domain, which again were observed in reality. However, some radar-observed precipitation in the southeast of Fig. 5.5, was not reproduced by the model. At the same time, Fig. 5.17, shows that the model has produced a clear temperature gradient stretching from the Bristol Channel east-southeastward, consistent with the warm front that was analysed in Fig. 5.5 and the observations. Temperatures are around 18 to 19°C south of the front. Besides being a zone of strong temperature gradient, the front also coincides with a gradient in mixing ratio: the moister air was located to the south of the front. Thus, it seems that the model state at 0900 UTC represents the actual distribution of temperature and moisture reasonably well, and precipitation perhaps slightly less so.

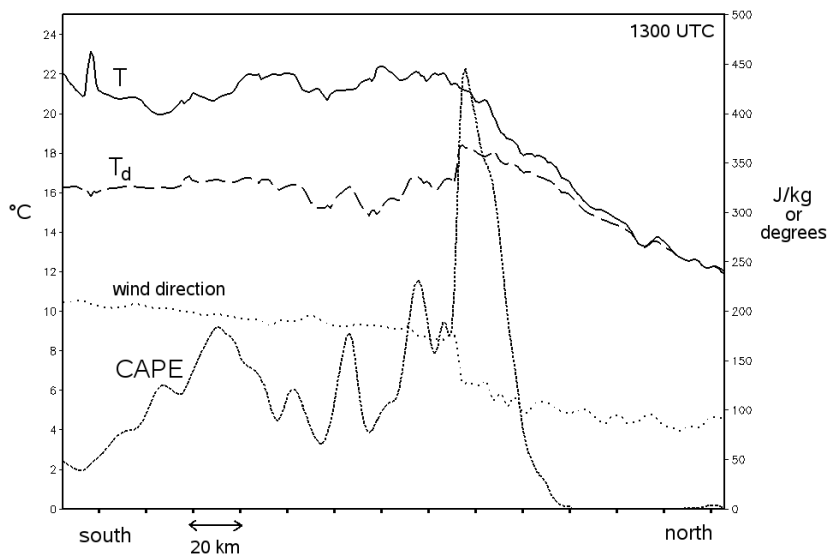


Figure 5.18: North-south cross-section of several parameters at 1300 UTC.

At 1200 UTC (Figs. 5.16 and 5.17, right top panels), the temperature has risen to between 20 and 24°C south of the front as it progressed northward by around 100 km. At that time, showers have initiated in the model north of the Bristol Channel. This is more or

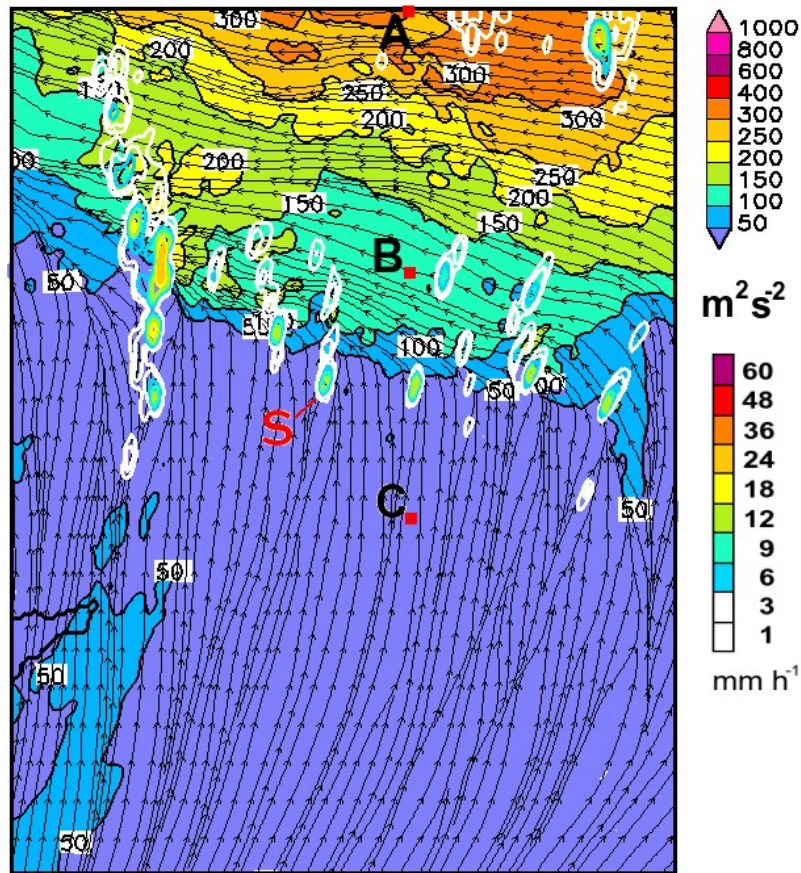


Figure 5.19: 0–1 km storm-relative helicity ($\text{m}^2 \text{s}^{-2}$) at 1300 UTC (shaded), streamlines of the wind at 10 m AGL, and 10 minute average precipitation rate (mm h^{-1}). The storm motion used for the calculation of the storm-relative helicity was estimated from the velocity of the simulated updraught (8.0 m s^{-1} from 210°). The hodographs at points A, B, and C are shown in 5.20.

less in accordance with reality (cf. Fig. 5.7), for the line of showers in the model develops only slightly to the southeast of where showers developed in reality, including the storm labelled "B". Weak showers that in reality developed in the upward branches of horizontal convective rolls, also develop in the model, albeit on a slightly smaller scale.

At 1300 UTC (Figs. 5.16 and 5.17, centre left panels) it can be seen that the nature of the warm front has changed somewhat: the zone of the strongest temperature gradient and that of the strongest moisture gradient do not coincide anymore. Fig. 5.16 (centre left) shows that an axis of enhanced moisture has formed north of the front. The temperature however, per definition, drops off directly to the north of the front. In Fig. 5.18 the behaviour of several parameters in a cross-section through the frontal zone is displayed. This cross-section was taken along the line displayed in the panel on the 1300 UTC maps in Figs. 5.16 and 5.17. Moving from south to north, it can be seen that the 2 m temperature starts to drop off north of the wind shift from south southeast to east southeast. At that same location, the absolute moisture, displayed as the 2 m dew point temperature, can be seen to increase by about 2°C from around 16°C to 18°C . This has a strong effect on the CAPE of a parcel lifted from near the surface, which rises from 200 J kg^{-1} to around

45 J kg^{-1} . If the location of the warm front is defined as the warm side of the temperature gradient (which is conventionally done so), the highest moisture is found on the cool side of the front. As a consequence, it must be concluded that CAPE shown in Figs. 5.17 (centre left) and 5.18 is also highest north of the front, rather than in the warmer air further south. This is not the case in the CAPE field interpolated from surface observations, which was shown in Fig. 5.14. Here, higher values of CAPE are located well south of the front, across southeastern England, partly outside the model domain. However, the model and the observations are insofar consistent in that they both feature an axis of relatively high CAPE, and high low-level moisture stretching along the frontal zone. At 1300 UTC, showers have initiated within and south of this moist zone. In subsequent hours, one of them can be seen to evolve into a particularly strong storm, which has many characteristics of a small supercell storm, as will be shown. On the images from 1300 to 1600 UTC, this storm is labelled "S". The path of the simulated storm S is clearly east of that of the real storm B and about an hour later (Figs. 5.6, 5.7, 5.8 and 5.9), but their evolution is rather similar in that they both develop on the south of the moist zone and move north-northeastward into the zone. In alternative model simulations that were carried out (the model domain was slightly smaller or placed further to the south), one or two storms with similar intensity formed each time, sometimes west and sometimes east of the path of storm S. This indicates that the situation favoured the development of this type of storm. Storm S can be seen to intensify significantly as it encounters the frontal boundary between 1300 and 1400 UTC, and reaches its peak intensity in terms of rainfall rate between 1400 and 1500 UTC. At 1600 UTC, the storm appears to have weakened significantly. Again, this behaviour is very similar to the storm B, that weakened shortly after 1400 UTC after moving out of the zone with highest low-level moisture.

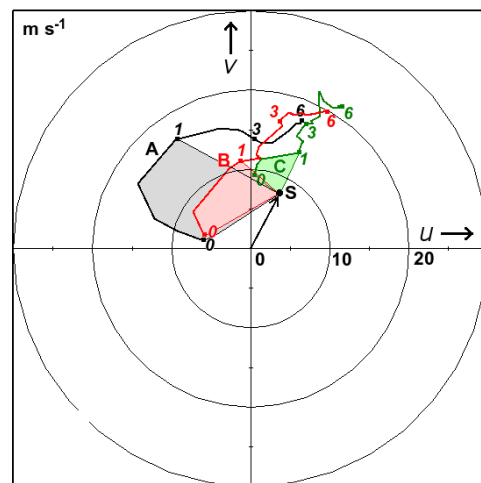


Figure 5.20: Hodographs at 1300 UTC for points A (black), B (red), and C (green) (Figs. 5.16 and 5.19). Along each of the hodographs, labels are provided at 10 m (0), 1 km AGL (1), 3 km AGL (3), and 6 km AGL (6). The thick circle labelled S corresponds with the motion of simulated storm S (8.0 m s^{-1} from 210°). The shaded regions in the respective colours have a surface area proportional to the 0–1 km environmental storm-relative helicity that would have been experienced by a storm moving with the same speed and direction as storm S.

The 0–1 km storm-relative helicity (0–1SRH) at 1300 UTC, shortly before the simulated storm S -then only a small shower- moved into the moist air is displayed in Fig. 5.19.

For the calculation of 0–1SRH, a storm motion vector needs to be assumed. Here, the average motion vector of storm S between 1300 and 1500 UTC was chosen, which was fairly constant over that interval. It can be seen that the 0–1SRH increases directly north of the wind-shift boundary, and further increases towards the north. This is due to the backed low-level winds relative to the air-mass south of the boundary.

Fig. 5.20 displays the hodographs (i.e. parameter curves $\mathbf{v}(z) = (u(z), v(z))$) simulated by the COSMO model at points A (black), B (red), and C (green) that are indicated in Figs. 5.16 and 5.19. The storm-relative helicity is equal to twice the area swept out by the storm-relative wind vector as one moves upward through the layer under consideration. In the figure, the motion vector of the simulated storm S is denoted by an arrow from the origin to a dot labelled S. The 0–1SRH for any of the curves is thus represented by an area bounded by the 10 m wind vector (which connects 'S' with '0'), the hodograph, and the 1 km wind vector (which connects 1 with 's'). These areas are shaded in gray (for point A), pink (for point B) and light green (for point C), respectively.

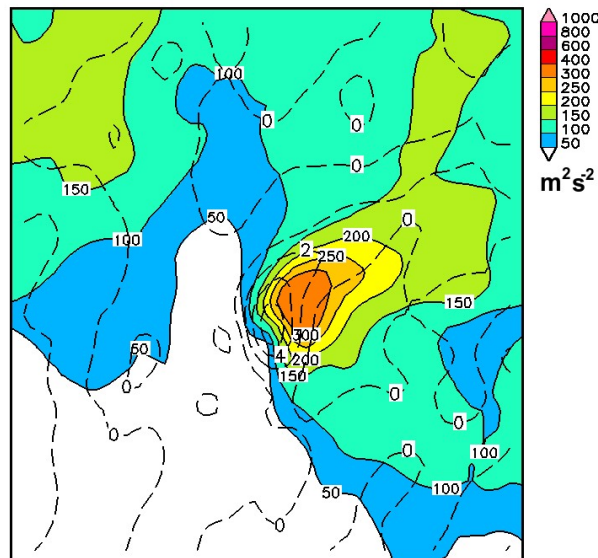


Figure 5.21: 0–1 km storm-relative helicity ($\text{m}^2 \text{s}^{-2}$) in the vicinity of the simulated storm S at 1500 UTC (displayed as shaded colours and with black solid contours), and vertical vorticity at 900 hPa (dashed contours, 10^{-3}s^{-1}). The storm motion used for the calculation of the storm-relative helicity was estimated from the velocity of the simulated updraught (8.0m s^{-1} from 210°). The area covered by the map is indicated by a blue square in Fig. 5.17 (1500 UTC map; left bottom).

One can see that at point A, well into the cold air, the hodograph curves clockwise with height between ground level and 3 km AGL and that the vertical wind shear is particularly large in the lowest kilometre. The veering winds with altitude are likely in part due to warm air advection, which, according to quasi-geostrophic theory, is consistent with veering wind with altitude (e.g. Kurz, 1984), and frictional effects in a stable Ekman layer. The large bulge creates a high 0–1SRH of $300 \text{m}^2 \text{s}^{-2}$. At point B, at approximately 25 km north of the frontal boundary, the cyclonic bulge is significantly smaller, resulting in a reduced but still rather high 0–1SRH of $138 \text{m}^2 \text{s}^{-2}$. Such values are common north of the surface warm front and are, for example, well above the median value ($89 \text{m}^2 \text{s}^{-2}$) for the environment of tornadic storms found by Rasmussen (2003), and comparable with the

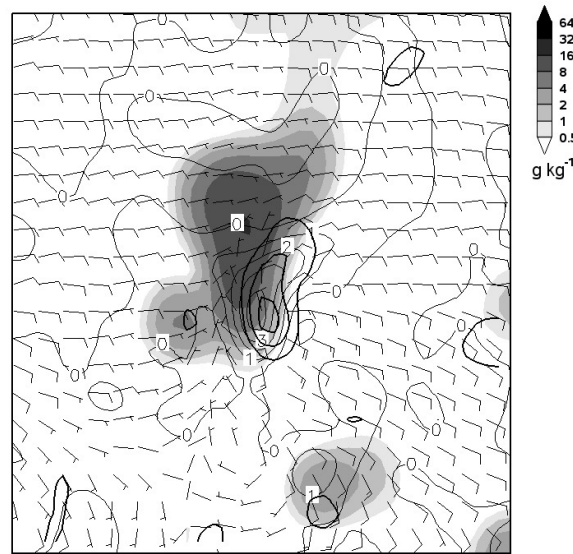


Figure 5.22: Rainwater at 1000 hPa (shaded, g kg^{-1}), vertical motion at 850 hPa (thin lines, contoured at 1, 2 and 3 m s^{-1}), vertical vorticity at 850 hPa (thick lines, contoured at $1 \cdot 10^{-3} \text{ s}^{-1}$, $3 \cdot 10^{-3} \text{ s}^{-1}$, and $5 \cdot 10^{-3} \text{ s}^{-1}$) and winds at 10 m AGL (barbs, according to the convention of Fig. 2.5). The area covered by the map is indicated by a blue square in Fig. 5.17 (1500 UTC map; left bottom).

$137 \text{ m}^2 \text{ s}^{-2}$ median value found by Thompson et al. (2003) in the environment of weak tornadoes (that is F0 or F1 on the Fujita scale; Fujita et al., 1972), and somewhat lower than the value of $165 \text{ m}^2 \text{ s}^{-2}$, that they found in the direct environment of strong tornadoes (F2 and stronger).

The distribution of storm-relative helicity in the closer environment of the storm S is displayed in Fig. 5.21, which depicts the situation at the time that the simulated storm S was the most intense (around 1500 UTC). In the figure, one can see that the helicity field is strongly enhanced to the east of the vertical vorticity maximum, i.e. the sector from which the air flows into the updraught. It thus appears that the storm itself induced a maximum of 0–1SRH in its inflow region, with values well over $300 \text{ m}^2 \text{ s}^{-2}$.

In Fig. 5.22, the correspondence of vertical vorticity with upward motion can be seen: the figure shows that the vertical vorticity (thick lines) and vertical velocity (thin lines) are to a great extent collocated. The vertical vorticity maximum is, however, displaced slightly upstream of the vertical velocity maximum.

Fig. 5.23 displays two vertical cross-sections, N-S (top) and W-E (bottom), respectively, through the simulated storm S. The N-S cross-section clearly shows the considerable tilt of the updraught, which is consistent with the net southerly wind shear seen in the simulation as well as in the observations (Fig. 5.10). It also shows that the maximum updraught speed is rather modest for a convective storm, with maximum values around 6 m s^{-1} . The highest vertical vorticity values that were produced in the simulation occurred very close to the ground; that is, near the 900 hPa pressure level at approximately 1000 m AGL. The highest value was $7.5 \cdot 10^{-3} \text{ s}^{-1}$.

This value may be compared with those of supercell storms in hurricane rain-bands, because these also develop with relatively little CAPE of a few 100s of J kg^{-1} , and shear that is

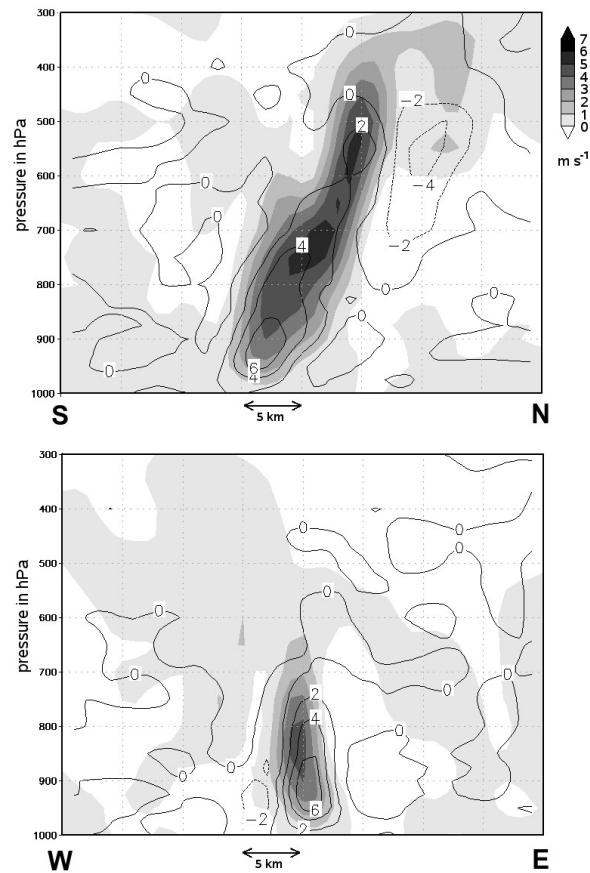


Figure 5.23: North-south vertical cross-section (top) and west-east vertical cross-section (bottom) through the updraught of simulated storm S. The updraught velocity in m s^{-1} (shaded), and vertical vorticity (contours) in 10^{-3} s^{-1} are shown.

strong in the lowest 1 to 2 kilometres. Idealized simulations of McCaul Jr and Weisman (1996), produced cells with vertical vorticity values around $20 \cdot 10^{-3} \text{ s}^{-1}$ at 1.5 km AGL, which is obviously significantly stronger than the values found for storm S. It must be noted, however, that both simulations are not completely comparable because their model had a grid spacing of 500 m, whereas the simulation presented here had a grid spacing of 1.1 km. The structure of their hurricane-environment cells and storm S is, however, very similar. Both have a maximum vertical vorticity very near to the earth's surface that extends upward from the surface only to approximately 3 kilometres (McCaul Jr and Weisman (1996); see their Fig. 7).

The storm intensity is comparable with values of vertical vorticity that Baker et al. (2009) measured with airborne Doppler-radar in small supercells in rain-bands of hurricane Ivan, that upon moving onshore and intensifying further, produced a number of tornadoes. Their measurements of one such cell, revealed a vertical structure in which the highest vertical velocity of 6 m s^{-1} was found at (only) 2.5 km AGL, and the vertical vorticity maximum of $7 \cdot 10^{-3} \text{ s}^{-1}$ at 1.5 km AGL. This structure and its intensity also very much resembles that of the simulated storm S. In agreement with McCaul Jr and Weisman (1996), these storms also exhibit a rather shallow circulation that extends up to only 4 km AGL (Baker

et al. (2009), see their Fig. 5.b).

The fact that the maximum vorticity occurs below the level of maximum velocity suggests that, in addition to vortex tilting, vortex stretching was a contributor to the low-level vertical vorticity.

5.3.3 Forcing terms in the perturbation pressure equation

Finally, the dynamically-induced perturbation will be discussed. Fig. 5.24 shows two west-east vertical cross-sections through the simulated storm updraught at 1500 UTC. The top panel displays the magnitude of the deformation tensor $\|\mathbf{D}\|$ and the magnitude of the spin tensor $\|\mathbf{\Omega}\|$. The spin tensor is proportional to the 3-dimensional vorticity vector, i.e. $\|\mathbf{\Omega}\| = \frac{1}{2}\sqrt{2}\|\boldsymbol{\omega}\|$. One can see that in most places, both fields are equal, except on the eastern flank of the storm's updraught, where the spin tensor is larger than the deformation. This area corresponds with the highest vertical vorticity.

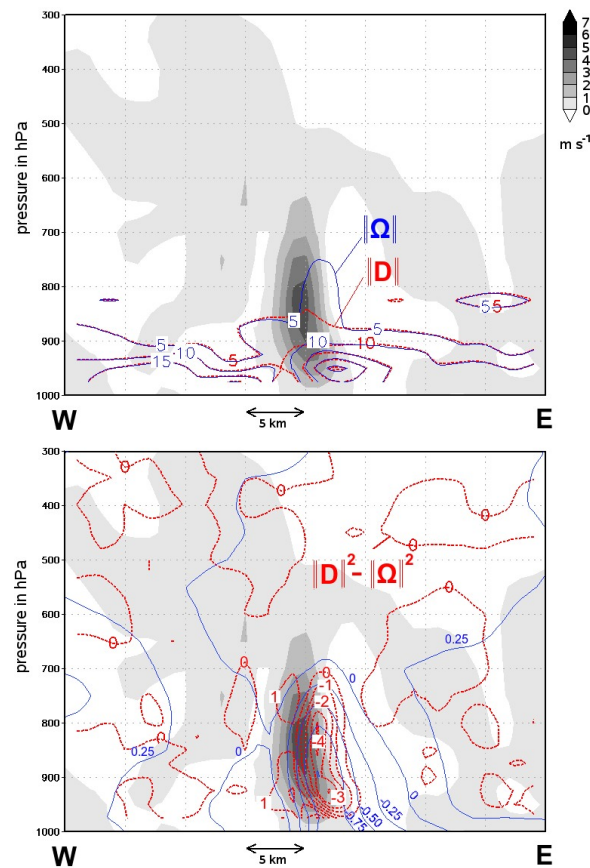


Figure 5.24: West-east vertical cross-section through the updraught of the simulated storm S at 1500 UTC. Displayed are the magnitude of the deformation tensor $\|\mathbf{D}\|$ (red, in 10^{-3} s^{-1}), and the magnitude of the spin tensor $\|\mathbf{\Omega}\| = \frac{1}{2}\sqrt{2}\|\boldsymbol{\omega}\|$ (blue, in 10^{-3} s^{-1}) in the top panel. The bottom panel shows the magnitude of the difference of the squares of both ($\|\mathbf{D}\|^2 - \|\mathbf{\Omega}\|^2$) (red, in 10^{-5} s^{-2}), and the equivalent perturbation pressure (blue; in hPa; for a description, see text.). Additionally the vertical velocity is displayed as gray shaded areas in the background.

Eq. 3.6 predicts that deformation and spin are associated with positive and negative pressure perturbations, respectively. Where both terms cancel, in this case approximately across the lowest 100 hPa in the atmospheric boundary layer, there is no local forcing for pressure perturbations, except from buoyancy. Indeed, this is consistent with what is known about a typical boundary layer: the flow is sheared, which means both deformation and vorticity occur, but there is no pressure perturbation associated with the flow.

Where a difference occurs between the magnitude of the forcing and of deformation, a net dynamic forcing for perturbation pressure occurs. As was noted, this is the case along the eastern flank of the storm updraught, where vorticity exceeds deformation. Where this is the case, Eq. 3.6 predicts a local perturbation pressure minimum. The net forcing of deformation and vorticity is displayed in the bottom panel of Fig. 5.24, which, in red colour shows the magnitude of the combined forcing term $\|\mathbf{D}\|^2 - \|\boldsymbol{\Omega}\|^2$. Indeed, a local minimum occurs. Additionally, the figure shows in blue colour an equivalent perturbation pressure. This is the perturbation pressure on a constant height level that is equivalent to the height perturbation on the corresponding pressure level. The height perturbation was calculated relative to a pseudo-horizontally (i.e. along a pressure surface) averaged mean computed over a box of $0.4 \times 0.4^\circ$ around the storm. The result is a pressure perturbation field that corresponds well with the location and shape of the dynamic forcing term. The minimum value is -1.0 hPa in the centre of the cyclonic updraught. This appears to be a very small perturbation value, but it is consistent with the aforementioned idealized simulations by McCaul Jr and Weisman (1996), who found similar values in their small and shallow supercells.

Chapter 6

Relevance of the results to severe weather threat

In the previous sections, it was shown how storm dynamics differ with varying vertical wind shear. The dynamics are not only of academic interest, but have a strong impact on several aspects of the storms, including their lifetime and the strength of the updraughts and downdraughts, which are key factors in determining their chances to produce severe weather. In this chapter, therefore, the relation between storm type – buoyancy dominated storms vs. storms in which wind shear is important – and severe weather likelihood will be explored by means of a concise literature review. Four different types of severe weather will be addressed: heavy rainfall, straight-line winds, hail, and tornadoes. The relevance of the results of the thesis to these weather hazards are summarized in Tab. 6.1.

Heavy rainfall

A good metric for the threat posed by convectively-produced heavy rainfall is the amount of rain that falls within a number of hours. This amount is the product of the average precipitation rate and the duration of precipitation. The precipitation rate is proportional to the net upward moisture flux within a storm system times the precipitation efficiency of the system (Doswell et al., 1996). Precipitation efficiency E is defined as the ratio of the amount of moisture that was transported upward into the system to the amount that reaches the ground as precipitation. The upward moisture flux itself can roughly be regarded as the moisture content of the updraught air q_{inflow} times the strength of the updraught w . In a formula, one can write

$$amount = rate \times duration$$

$$amount \propto E w q_{inflow} \times duration$$

Precipitation efficiency is found to be dependent on several factors, including updraught width (e.g. Shusse and Tsuboki, 2006), environmental relative moisture, and wind shear (e.g. Market et al., 2003). Wind shear is found to reduce precipitation efficiency, which

	weak shear	strong shear
risk of heavy rainfall	relatively low, because local storm duration is limited by the life time of an individual cell	may be low or high depending on whether the shear induces new cell growth over the same location
risk of straight-line winds	may be low or high depending on forcing by evaporational cooling	may be high even when evaporational cooling is limited, and extreme when evaporational effects combine with vertical transport of horizontal momentum
risk of large hail	relatively low	relatively high, due to higher availability of hail embryo's and stronger updraughts
risk of tornadoes	low, although weak tornadoes may form	may be high when low-level shear and low-level buoyancy are very strong

Table 6.1: Summary of the risk of several types of severe weather in relation to vertical wind shear.

is not surprising when considering that updraughts tend to tilt down-shear, which leads to a greater proportion of rain falling into unsaturated air, not moistened by lower portions of the updraught, so that a relatively large part of the precipitation may evaporate. Another factor affecting precipitation efficiency is updraught speed, hence the notation $E(w, \text{other factors})$ in the equation above. When an updraught is strong, the condensate that forms within it is rapidly transported to the upper levels of the troposphere (Williams et al., 2005). This also means that precipitation forming has a long trajectory through what is probably an unsaturated layer of air, before reaching the ground. This reduces precipitation efficiency. In contrast, a situation in which updraught speeds are more modest, and cloud droplets have sufficient time to coalesce to rain drops would yield a higher precipitation efficiency. An important factor that completeness requires to be mentioned is the depth of the layer that allows for coalescence of droplets, i.e. the warm cloud depth: the deeper it is, the higher precipitation efficiency will be.

Moisture of a storm's inflow q_{inflow} is not a factor that relates to storm type. Buoyancy-dominated storms systems, and storm systems for which buoyancy and shear are both important, may occur in environments with very different low-level moisture flowing into the convective updraughts.

Updraught speed w is to some extent related to the nature of storm dynamics. It is true

that storms interacting with wind shear may have stronger low-level updraughts as they are enhanced by vertical gradients of perturbation pressure, and that these updraughts are more persistent. But, it may well be that the effects of updraught speed on upward moisture flux and on precipitation efficiency approximately compensate in typical circumstances. This is still an unanswered question however.

The *local storm duration* for purely buoyancy-driven storm systems is controlled by the duration of individual updraughts. After an initial updraught disappears, the troposphere is stabilized through local low-level cooling and compensating subsidence, as was described, and further convective activity at that particular location is not to be expected. In contrast, storm systems influenced by wind shear are longer-lived, because the shear usually induces regeneration of new cells along a particular flank of the storm. The duration of precipitation at that point is then much less related to the system's lifetime, but more to the time it takes for the system to move over that point, which may be much longer than the lifetime of an individual updraught. On the other hand, in situations with strong vertical wind shear, relatively fast storm system motion is also a possibility, which means that strong wind shear does by no means indicate a high potential of rain by itself. More rigorous investigation of low-level winds with respect to steering-level winds (Corfidi et al., 1996; Corfidi, 2003) can give a more accurate prediction of heavy rainfall in such cases. Another factor that may, in some cases, influence the local duration of a storm very strongly, is the orography. Orography often has the effect of sustaining low-level convergence in cases of upslope flow, which induces new cell generation over those same slopes time after time. However, a general relation between storm type and orography has not been found, so that this factor will be omitted from consideration here.

The overall conclusion of the above discussion of rainfall threat as a function of storm type is the following: heavy rainfall risk is in cases of very weak shear limited by the lifetime of an individual updraught, whereas in other cases there *may* be an enhanced chance for updraught regeneration over the same location. This leads to a longer local rainfall duration, and, hence, a higher risk of very high rainfall amounts.

Straight-line winds

By straight-line winds all winds related to convective storms are meant that do not occur within a tornado. Usually, these are associated with downdraughts that gain downward vertical momentum as a result of negative thermal buoyancy. This negative buoyancy is primarily due to cooling by the evaporation of hydrometeors, while the weight of the hydrometeors themselves may also contribute to it (Wakimoto, 2001; Srivastava, 1985). Upon reaching the earth's surface, these downdraughts spread out and may occasionally be intense enough to cause damage. Important factors for the creation of evaporatively-driven downdraughts are the presence of a deep dry layer of air in which hydrometeors can evaporate. Such a layer may either be a deep boundary layer or a dry layer just above the boundary layer. Additionally, the availability of small hydrometeors that have a high surface area relative to their volume, is important.

Downdraughts induced by negative buoyancy may occur both with convective storms that are mostly buoyancy-driven and with storms that are in addition strongly interacting with the environmental shear. However, in the latter type of storm, vertical perturbation pressure gradients may also contribute to downward vertical momentum in addition to

negative buoyancy (Klemp and Rotunno, 1983). This occurs, for example, in *occlusion downdraughts* that may form during the lifetime of a supercell storm.

An additional contribution to the ultimate horizontal winds speed in a downdraught at the surface is the downward transport of horizontal momentum (Nakamura et al., 1996). Vertical transport of horizontal momentum will only play a role when vertical wind shear exists. Such vertical wind shear can be caused by the storm system itself, but the presence of environmental wind shear will contribute to it as well. Thus, two arguments have been listed why straight-line winds are likely to be more intense in a strongly-sheared than in a weakly-sheared environment. Finally, it must also be mentioned that the better storm organization in sheared environments, that results from updraught regeneration on a particular flank of a storm system, also aids the formation of large masses of evaporationally cooled air, i.e. *cold pools*. These tend to spread out as a gravity current that may be accompanied by damaging straight-line winds.

It is therefore concluded that straight-line winds may occur with any storm but that pressure perturbation effects, downward horizontal momentum transport, and improved storm organization enhance the risk of damaging winds in sheared convection relative to convection purely driven by buoyancy.

Large hail

Large hail requires a strong updraught that – like heavy precipitation – contains a high amount of moisture. In the case of hail, updraught speed is in fact a critical component, in that it should compensate the downward motion of the hailstone for some time in order for it to reach a considerable diameter.

Moreover, it is favourable for large hail formation if the updraught transports most condensate rapidly above the freezing level, before the small cloud droplets grow into large rain drops by means of coalescence (i.e. the *warm rain process*; Williams et al., 2005). Besides a strong updraught, a small warm cloud depth helps to accomplish this. Another aspect is updraught lifetime, for a longer-lived updraught is also favourable for large hail formation, because it enables a hailstone to grow for longer time before the updraught collapses.

Overall, thus, updraught speed, updraught lifetime and warm cloud depth are the most important predictors of large hail. Updraught speed and updraught lifetime are both related to storm organization. We have noted that updraught speed is likely to be enhanced in rotating updraughts, so that such a storm is more likely to produce large hail. Additionally, such supercell storms, that develop in strong shear usually propagate more or less continuously, so that one can consider the upward branch of the convective circulation as a single long-lived updraught, which should aid large hail formation as well. Storms in more moderate shear will usually consist of more or less discrete updraughts, that nonetheless still propagate in into one favoured direction. In that case, graupel particles or smaller hailstones (called hailstone embryos Ziegler et al., 1983; Knight and Knight, 1970) that develop in older updraughts often serve as the basis of new hailstone growth. For storms in weak vertical shear, the notion of "upstream" is ill-defined, and the chance of older cells depositing hailstone embryos into an active updraught is smaller. Statistical studies support the increased likelihood of large hail with increasing wind shear (e.g. Groenemeijer and van Delden, 2007).

To summarize the hail threat dependence on wind shear, we conclude that it increases with increasing wind shear because storms have tend to have stronger and longer-lived updraughts, and the chance of having a favourable interaction between cells, where older updraughts deposit hailstone embryos into new updraughts, is larger.

Tornadoes

Tornadoes can roughly, and also somewhat arbitrarily, be divided into two categories. Namely those that develop in association with a larger parent circulation (type I), and those that do not (type II) (Davies-Jones et al., 2001). Type I tornadoes are on average stronger and longer-lived than type II tornadoes. The larger parent circulation of type I tornadoes, also known as a *low-level mesocyclone*, is usually tied to a deeper *mesocyclone*, or rotating updraught. As has been discussed, this is, per definition, the distinctive feature of a supercell storm which develops in strong vertical wind shear. Hence, type I tornadoes are a phenomenon almost exclusively tied to situations of strong deep-layer shear. Recent research suggests that type I tornadoes are especially favoured by strong wind shear in the lowest kilometre above ground (Craven et al., 2002; Thompson et al., 2003; Markowski et al., 2003) and high thermal buoyancy for a lifted parcel in the lower part of the troposphere (Davies, 2002).

On the other hand, type II tornadoes are "generally a small and weak vortex that forms along a stationary or slowly moving wind-shift line from the rolling-up of the associated vortex sheet into individual vortices" (Davies-Jones et al., 2001). These tornadoes are, therefore, not exclusive to strong shear formation.

To summarize, one can conclude that although tornadoes may occur in environments of weak and strong shear, the stronger and longer-lived type I tornadoes almost exclusively occur in association with supercells that form in strong vertical wind shear. Hence, stronger shear increases the overall tornado risk.

Chapter 7

Summary and conclusions

Two cases of deep, moist convection have been discussed that took place in very different meteorological and topographical environments. The storms forming over the Black Forest on 12 July 2006 occurred with high CAPE, weak vertical wind shear, and relatively low humidity across a low but pronounced mountain range. On the other hand, the storms that formed on 28th July 2005 across England occurred within a very different regime, characterized by strong vertical wind shear and relatively weak CAPE.

	PRINCE/Black Forest storm 12 July 2006	CSIP/England storm 28 July 2005
CAPE	$\approx 2000 \text{ J kg}^{-1}$	$\approx 400 \text{ J kg}^{-1}$
0–6 km bulk shear	$\approx 6 \text{ m s}^{-1}$	$\approx 25 \text{ m s}^{-1}$
BRN_{WK}	110	1.3
mechanism of initiation	orographically-induced circulations	horizontal convective (boundary-layer) rolls with intensification upon crossing a warm front
updraughts	cluster of powerful vertical updraughts	one tilted long-lived rotating updraught
propagation	discrete and to a high degree random, with down-shear direction preferred	quasi-continuously, with a slight rightward propagation relative to the mean lower tropospheric wind
important dynamics	buoyancy-induced	wind shear-induced and buoyancy-induced

Table 7.1: Comparison of the Black Forest/PRINCE and England/CSIP storm systems.

The dimensionless Bulk Richardson Number quantifies the relative importance of dynamically-induced pressure perturbations relative to buoyancy-induced pressure perturbations. In the presented cases, they were estimated to be near 110 and 1.3 for the Black Forest/PRINCE case and the English/CSIP case, respectively. As a result, the storms developed in very different ways: the Black Forest storm system consisted of vertically-oriented updraughts whose initial locations were to a great extent determined by orographically-induced flows. In contrast, the initiation of the English storm occurred in the upward branch of one of many boundary-layer rolls, a shear-induced effect and obtained a tilted updraught. The Black Forest storm system exhibited the behaviour of a group of discrete convective bubbles rising upward through the troposphere and inducing descent in their vicinity. The propagation of the system was clearly in a discrete manner, rather than continuous which would be likely in a shear-dominated system. New convective updraughts were only slightly favoured on the southeastern flank of the system. The English storm developed out of shear-induced horizontal convective rolls, rather than orographic valley or mountain breezes as was the case in the Black Forest. After slow initial development, probably because of the shear being so strong in comparison with buoyancy, a few relatively small but intensely rotating updraughts developed – the one that affected Birmingham having been discussed rather extensively – which produced tornadoes of which at least one produced significant damage.

The most important findings regarding the buoyancy-forced (i.e. Black Forest/PRINCE) convective system will now be summarized. Firstly, it was shown that orographically-induced flow circulations effects play an important role in the initiation of such storms. The first Doppler-lidar observations of radially convergent flow below an initiating convective updraught have been shown. It has not been determined to what extent orographically-induced flows still play a role with respect to convective initiation in more dynamic and strongly-sheared environments, but this study forms a good reference case for new research to be carried out in the framework of the currently ongoing Convective and Orographically-Induced Precipitation Study (COPS; Wulfmeyer et al., 2008). Secondly, it was shown how the storm dynamics are controlled primarily by buoyancy-induced effects. Local perturbations of buoyancy in a convective updraught are communicated to its environment and induce downward motion in the neighbourhood of convective storms. These downdraughts are thus not forced by negative thermal buoyancy through evaporation of hydrometeors, or by dynamic pressure perturbations, but by the effect of a nearby positive buoyancy perturbation. The net result of such downward motions is to stabilize the storm's environment, as has been shown in a theoretical study by Bretherton and Smolarkiewicz (1989). This work has added observations of this phenomenon in the lower troposphere. Moreover, Bretherton and Smolarkiewicz showed that the dry air spreads out horizontally as it meets the boundary layer and that its effects are an important part of the convective lifecycle. The effect is that the mid- and lower troposphere warms and dries out, which reduces CAPE and increases CIN, thereby preventing subsequent convective initiation near the storm system. This is in contrast with a much better known conceptual model of the convective life cycle in which the spreading out of a cold pool prevents new storm formation behind its leading gust front. In the observed case, however, there was no indication of a cold pool that could prevent new storm initiation in such a large area as was observed.

The most important findings of the partly dynamically, partly buoyancy-forced convective system (England/CSIP) are the following. It was shown that small showers that develop within the upward branches of horizontal convective rolls in the boundary layer can suddenly intensify when they interact with a frontal zone perpendicular to such rolls. The

intensification can be understood as being caused by an increase in both latent instability (CAPE) and low-level wind shear. The remarkable aspect of the storm that was studied in most detail, was that it reached its peak intensity on the cold side of a warm front, i.e. where low-level temperatures were dropping off quickly away from the surface front, and that a rotating updraught developed, powerful enough to produce an F2 tornado. Both analyses based on surface observations and radiosondes, and a simulation with a high-resolution numerical model showed that the area favourable for such development was only about 30–50 km wide. It was characterized by a zone of enhanced CAPE, of which most was released very near to the surface, which enables strong stretching of vorticity tilted from a horizontal axis into the vertical. The enhanced CAPE was primarily due to a maximum of boundary-layer moisture within that zone. The exact conditions under which such zones form remains a topic of further study, but probably include a contribution from the moisture flux convergence along the front in combination with evapotranspiration and a lack of vertical mixing. It has been shown unambiguously that strong (F2) tornadoes do not require large amounts of CAPE to form, or even modest amounts across a large area. Instead, modest amounts of CAPE in a small zone can be sufficient, given that other parameters previously identified to be favourable for tornadogenesis are given, including the presence of strong storm-relative helicity and a low LCL height. It was noted that the mesoscale environment of this small supercell is kinematically and thermodynamically comparable with hurricane rainbands, in which tornado-producing supercells are known to commonly occur.

Finally, returning to Chapter 2, several definitions of instability were discussed. A theoretical argument was given why latent instability – the condition that in a vertical profile of temperature and humidity a parcel can be found that becomes positively buoyant after being lifted – is to be preferred for forecasting convection. The argument is that of three definitions of instability (potential instability, conditional instability, latent instability) latent instability is the most restrictive. Furthermore, from a practical viewpoint, studies assessing the quality of convective indices, indicate that indices based on this concept perform better.

References

- Asai, T., 1970: Three-dimensional features of thermal convection in a plane Couette flow. *J. Meteor. Soc. Japan*, **48**, 18–29.
- Baker, A., M. Parker, and M. Eastin, 2009: Environmental ingredients for supercells and tornadoes within hurricane Ivan. *Wea. Forecasting: In Press*.
- Barnes, S., 1964: A technique for maximizing details in numerical weather map analysis. *J. Appl. Meteor.*, **3**, 396–409.
- Barthlott, C., U. Corsmeier, C. Meißner, F. Braun, and C. Kottmeier, 2005: The influence of mesoscale circulation systems on triggering convective cells over complex terrain. *Atmos. Res.*, **81**, 150–175.
- Bluestein, H., 1993: *Synoptic-Dynamic Meteorology in Midlatitudes. Volume II: Observations and Theory of Weather Systems*. Oxford University Press, 606 pp.
- Bretherton, C. and P. Smolarkiewicz, 1989: Gravity waves, compensating subsidence and detrainment around cumulus clouds. *J. Atmos. Sci.*, **46**, 740–759.
- Brooks, H. and C. Doswell, III, 2001: Normalized damage from major tornadoes in the United States: 1890–1999. *Wea. Forecasting*, **16**, 168–176.
- Browning, K. et al., 2007: The Convective Storm Initiation Project. *Bull. Amer. Meteor. Soc.*, **88**, 1939–1955.
- Bunkers, M., B. Klimowski, J. Zeitler, R. Thompson, and M. Weisman, 2000: Predicting supercell motion using a new hodograph technique. *Wea. Forecasting*, **15**, 61–79.
- Corfidi, S., 2003: Cold pools and MCS propagation: Forecasting the motion of downwind-developing MCSs. *Wea. Forecasting*, **18**, 997–1017.
- Corfidi, S., J. Meritt, and J. Fritsch, 1996: Predicting the movement of mesoscale convective complexes. *Wea. Forecasting*, **11**, 41–46.
- Corsmeier, U., R. Hankers, and A. Wieser, 2001: Airborne turbulence measurements in the lower troposphere onboard the research aircraft Dornier 128-6, D-IBUF. *Meteorol. Z.*, **10**, 315–329.
- Couvreur, F., F. Guichard, J. Redelsperger, C. Kiemle, V. Masson, J. Lafore, and C. Flamant, 2005: Water-vapour variability within a convective boundary-layer assessed by large-eddy simulations and IHOP_2002 observations. *Quart. J. Roy. Met. Soc.*, **131**.

- Craven, J., R. Jewell, and H. Brooks, 2002: Comparison between observed convective cloud-base heights and lifting condensation level for two different lifted parcels. *Wea. Forecasting*, **17**, 885–890.
- Das, P., 1979: A non-archimedean approach to the equations of convection dynamics. *J. Atmos. Sci.*, **36**, 2183–2190.
- Davies, J., 2002: On low-level thermodynamic parameters associated with tornadic and nontornadic supercells. In *Preprints, 21st Conf. on Severe Local Storms, San Antonio, TX, Amer. Meteor. Soc.*, 603–606.
- Davies-Jones, R., 1984: Streamwise vorticity: The origin of updraft rotation in supercell storms. *J. Atmos. Sci.*, **41**, 2991–3006.
- Davies-Jones, R., 2002: Linear and nonlinear propagation of supercell storms. *J. Atmos. Sci.*, **59**, 3178–3205.
- Davies-Jones, R., 2003a: An expression for effective buoyancy in surroundings with horizontal density gradients. *J. Atmos. Sci.*, **60**, 2922–2925.
- Davies-Jones, R., 2003b: Reply. *J. Atmos. Sci.*, **60**, 2420–2426.
- Davies-Jones, R., R. Trapp, and H. Bluestein, 2001: Tornadoes and Tornadic Storms. *Severe Convective Storms, Meteor. Monogr., C.A. Doswell III (ed.)*, **50**, 167–221.
- Doswell, III, C., H. Brooks, and R. Maddox, 1996: Flash flood forecasting: An ingredients-based methodology. *Wea. Forecasting*, **11**, 560–581.
- Doswell, III, C. and D. Burgess, 1993: Tornadoes and tornadic storms: A review of conceptual models, The Tornado: Its structure, dynamics, prediction and hazards. *Geophysical Monograph*, **79**, 161–172.
- Doswell, III, C. and P. Markowski, 2004: Is buoyancy a relative quantity? *Mon. Wea. Rev.*, **132**, 853–863.
- Dotzek, N., P. Groenemeijer, B. Feuerstein, and A. Holzer, 2009: Overview of ESSL’s severe convective storms research using the European Severe Weather Database ESWD. *Atmos. Res. (In Press)*.
- Emanuel, K., 1994: *Atmospheric Convection*. Oxford University Press, USA.
- ESSL, 2009: European Severe Weather Database, <http://www.eswd.eu>.
- Etling, D. and R. Brown, 1993: Roll vortices in the planetary boundary layer: A review. *Boundary-Layer Meteorology*, **65**, 215–248.
- Fritsch, J., 1975: Cumulus dynamics: Local compensating subsidence and its implications for cumulus parameterization. *Pure Appl. Geophys.*, **113**, 851–867.
- Fujita, T., Satellite, M. R. Project, and U. of Chicago Department of the Geophysical Sciences, 1972: *Proposed characterization of tornadoes and hurricanes by area and intensity*. Satellite and Mesometeorology Research Project, Dept. of the Geophysical Sciences, Univ. of Chicago.

- Glickman, T., editor, 2000: *Glossary of Meteorology*. American Meteorological Society, 2nd edition.
- Groenemeijer, P., C. Barthlott, A. Behrendt, U. Corsmeier, J. Handwerker, M. Kohler, C. Kottmeier, H. Mahlke, S. Pal, M. Radlach, J. Trentmann, A. Wieser, and V. Wulfmeyer, 2009: Observations of a convectively-induced downdraft stabilizing the lower troposphere. *Mon. Wea. Rev.*, **137**, 585–602.
- Groenemeijer, P. and A. van Delden, 2007: Sounding-derived parameters associated with large hail and tornadoes in the Netherlands. *Atmos. Res.*, **83**, 473–487.
- Haklander, A. and A. Van Delden, 2003: Thunderstorm predictors and their forecast skill for the Netherlands. *Atmos. Res.*, **67**, 273–299.
- Hartmann, J., C. Kottmeier, and S. Raasch, 1997: Roll vortices and boundary-layer development during a cold air outbreak. *Boundary-Layer Meteorology*, **84**(1), 45–65.
- Hense, A., G. Adrian, C. Kottmeier, C. Simmer, and V. Wulfmeyer, 2003: Quantitative Precipitation Forecast: Priority program of the German Research Foundation.
- Holton, J. R., 1992: An introduction to dynamic meteorology.
- Houston, A. and D. Niyogi, 2007: The sensitivity of convective initiation to the lapse rate of the active cloud-bearing layer. *Mon. Wea. Rev.*, **135**, 3013–3032.
- Huntrieser, H., H. Schiesser, W. Schmid, and A. Waldvogel, 1997: Comparison of traditional and newly developed thunderstorm indices for Switzerland. *Wea. Forecasting*, **12**, 108–125.
- Johnson, B., 1983: The heat burst of 29 May 1976. *Mon. Wea. Rev.*, **111**, 1776–1792.
- Kain, J. and J. Fritsch, 1990: A one-dimensional entraining/detraining plume model and its application in convective parameterization. *J. Atmos. Sci.*, **47**, 2784–2802.
- Klemp, J., 1987: Dynamics of tornadic thunderstorms. *Annu. Rev. Fluid Mech.*, **19**, 369–402.
- Klemp, J. and R. Rotunno, 1983: A study of the tornadic region within a supercell thunderstorm. *J. Atmos. Sci.*, **40**, 359–377.
- Knight, C. and N. Knight, 1970: Hailstone embryos. *J. Atmos. Sci.*, **27**, 659–666.
- Koch, S., M. desJardins, and P. Kocin, 1983: An interactive Barnes objective map analysis scheme for use with satellite and conventional data. *J. Appl. Meteor.*, **22**, 1487–1503.
- Kottmeier, C., N. Kalthoff, C. Barthlott, U. Corsmeier, J. van Baelen, A. Behrendt, R. Behrendt, A. Blyth, R. Coulter, S. Crewell, et al., 2008: Mechanisms initiating deep convection over complex terrain during COPS. *Meteorologische Zeitschrift*, **17**(6), 931–948.
- Kottmeier, C., T. Reetz, P. Ruppert, and N. Kalthoff, 2001: A new aerological sonde for dense meteorological soundings. *J. Atm. Oc. Tech.*, **18**, 1495–1502.

- Kunz, M., 2007: The skill of convective parameters and indices to predict isolated and severe thunderstorms. *Nat. Hazards Earth Syst. Sci.*, **7**, 327–342.
- Kurz, M., 1984: Leitfäden für die Ausbildung im Deutschen Wetterdienst, Nr. 8: Synoptische Meteorologie. *Selbstverlag des Deutschen Wetterdienstes, Offenbach am Main*.
- LeMone, M., 1973: The structure and dynamics of horizontal roll vortices in the planetary boundary layer. *J. Atmos. Sci.*, **30**, 1077–1091.
- Manzato, A. and G. Morgan, 2003: Evaluating the sounding instability with the lifted parcel theory. *Atmos. Res.*, **67**, 455–473.
- Market, P., S. Allen, R. Scofield, R. Kuligowski, and A. Gruber, 2003: Precipitation efficiency of warm-season midwestern mesoscale convective systems. *Wea. Forecasting*, **18**, 1273–1285.
- Markowski, P., C. Hannon, J. Frame, E. Lancaster, A. Pietrycha, R. Edwards, and R. Thompson, 2003: Characteristics of vertical wind profiles near supercells obtained from the Rapid Update Cycle. *Wea. Forecasting*, **18**, 1262–1272.
- Marshall, T. and S. Robinson, 2006: The Birmingham, UK Tornado: 28 July 2005. In *Preprints, 23rd Conference on Severe Local Storms, 6-10 November 2006, St. Louis, MO, USA*.
- McCaul Jr, E. and M. Weisman, 1996: Simulations of shallow supercell storms in land-falling hurricane environments. *Mon. Wea. Rev.*, **124**, 408–429.
- Nakamura, K., R. Kershaw, and N. Gait, 1996: Prediction of near-surface gusts generated by deep convection. *Meteorol. Appl.*, **3**.
- Normand, C., 1938: On instability from water vapour. *Quart. J. Roy. Meteor. Soc.*, **64**, 47–69.
- Radlach, M., A. Behrendt, and V. Wulfmeyer, 2008: Scanning rotational Raman lidar at 355 nm for the measurement of tropospheric temperature fields. *Atmos. Chem. Phys.*, **8**, 159–169.
- Rasmussen, E., 2003: Refined supercell and tornado forecast parameters. *Wea. Forecasting*, **18**, 530–535.
- Ritter, B. and J.-F. Geleyn, 1992: A comprehensive radiation scheme for numerical weather prediction models with potential applications in climate simulations. *Mon. Wea. Rev.*, **120**, 303–325.
- Rotunno, R. and J. Klemp, 1982: The influence of the shear-induced pressure gradient on thunderstorm motion. *Mon. Wea. Rev.*, **110**, 136–151.
- Rotunno, R. and M. Weisman, 2003: Comment on 'linear and nonlinear propagation of supercell storms'. *J. Atmos. Sci.*, **60**, 2413–2419.
- Schättler, U., G. Doms, and C. Schraff, 2007: *A description of the nonhydrostatic regional COSMO-model, Part VII: User's Guide*. Available at: <http://www.cosmo-model.org>.

- Schultz, D., P. Schumacher, and C. Doswell, III, 2000: The intricacies of instabilities. *Mon. Wea. Rev.*, **128**, 4143–4148.
- Seifert, A., M. Baldauf, J. Förstner, T. Hanisch, C. Schraff, and K. Stephan, 2007: Forecasting of severe weather with the convection-resolving model COSMO-LMK. *Preprints, 4th European Conference on Severe Storms, 10–14 September 2007, Trieste, Italy*.
- Shusse, Y. and K. Tsuboki, 2006: Dimension characteristics and precipitation efficiency of cumulonimbus clouds in the region far south from the Mei-Yu front over the eastern asian continent. *Mon. Wea. Rev.*, **134**, 1942–1953.
- Srivastava, R., 1985: A simple model of evaporatively driven downdraft: Application to microburst downdraft. *J. Atmos. Sci.*, **42**, 1004–1023.
- Thompson, R., R. Edwards, J. Hart, K. Elmore, and P. Markowski, 2003: Close proximity soundings within supercell environments obtained from the Rapid Update Cycle. *Wea. Forecasting*, **18**, 1243–1261.
- Tiedtke, M., 1989: A comprehensive mass flux scheme for cumulus parameterization in large-scale models. *Mon. Wea. Rev.*, **117**, 1779–1800.
- Wakimoto, R., 2001: Convectively driven high wind events. *Severe Convective Storms, Meteor. Mononogr., C.A. Doswell III (ed.)*, **28**, 255–432.
- Walser, A., D. Lüthi, and C. Schär, 2004: Predictability of precipitation in a cloud-resolving model. *Mon. Wea. Rev.*, **132**, 560–577.
- Weckwerth, T., D. Parsons, S. Koch, J. Moore, M. LeMone, B. Demoz, C. Flamant, B. Geerts, J. Wang, and W. Feltz, 2004: An overview of the International H2O Project (IHOP_2002) and some preliminary highlights. *Bull. Amer. Meteor. Soc.*, **85**, 253–277.
- Weckwerth, T., J. Wilson, and R. Wakimoto, 1996: Thermodynamic variability within the convective boundary layer due to horizontal convective rolls. *Mon. Wea. Rev.*, **124**, 769–784.
- Weisman, M. and J. Klemp, 1982: The dependence of numerically simulated convective storms on vertical wind shear and buoyancy. *Mon. Wea. Rev.*, **110**, 504–520.
- Weisman, M. and R. Rotunno, 2000: The use of vertical wind shear versus helicity in interpreting supercell dynamics. *J. Atmos. Sci.*, **57**, 1452–1472.
- Williams, E., V. Mushtak, D. Rosenfeld, S. Goodman, and D. Boccippio, 2005: Thermodynamic conditions favorable to superlative thunderstorm updraft, mixed phase microphysics and lightning flash rate. *Atmos. Res.*, **76**, 288–306.
- Wulfmeyer, V., A. Behrendt, H. Bauer, C. Kottmeier, U. Corsmeier, A. Blyth, G. Craig, U. Schumann, M. Hagen, S. Crewell, et al., 2008: The Convective and Orographically-induced Precipitation Study: A research and development project of the World Weather Research Program for improving quantitative precipitation forecasting in low-mountain regions. *Bull. Amer. Meteor. Soc.*, **89**, 1477–1486.

- Yuter, S. and R. Houze Jr., 1995: Three-dimensional kinematic and microphysical evolution of florida cumulonimbus. Part I: Spatial distribution of updrafts, downdrafts, and precipitation. *Mon. Wea. Rev.*, **123**, 1921–1940.
- Ziegler, C., P. Ray, and N. Knight, 1983: Hail growth in an Oklahoma multicell storm. *J. Atmos. Sci.*, **40**, 1768–1791.

Appendix A

A kinematic interpretation of the terms in the diagnostic pressure equation

The three-dimensional velocity gradient, which is a tensor of order 2, can be split into a symmetric and an antisymmetric part:

$$\nabla \mathbf{v} = \begin{pmatrix} \frac{\partial u}{\partial x} & \frac{\partial u}{\partial y} & \frac{\partial u}{\partial z} \\ \frac{\partial v}{\partial x} & \frac{\partial v}{\partial y} & \frac{\partial v}{\partial z} \\ \frac{\partial w}{\partial x} & \frac{\partial w}{\partial y} & \frac{\partial w}{\partial z} \end{pmatrix} = \frac{1}{2} \begin{pmatrix} \frac{\partial u}{\partial x} + \frac{\partial u}{\partial x} & \frac{\partial u}{\partial y} + \frac{\partial v}{\partial x} & \frac{\partial u}{\partial z} + \frac{\partial w}{\partial x} \\ \frac{\partial v}{\partial x} + \frac{\partial u}{\partial y} & \frac{\partial v}{\partial y} + \frac{\partial v}{\partial y} & \frac{\partial v}{\partial z} + \frac{\partial w}{\partial y} \\ \frac{\partial w}{\partial x} + \frac{\partial u}{\partial z} & \frac{\partial w}{\partial y} + \frac{\partial v}{\partial z} & \frac{\partial w}{\partial z} + \frac{\partial w}{\partial z} \end{pmatrix} + \frac{1}{2} \begin{pmatrix} 0 & \frac{\partial u}{\partial y} - \frac{\partial v}{\partial x} & \frac{\partial u}{\partial z} - \frac{\partial w}{\partial x} \\ \frac{\partial v}{\partial x} - \frac{\partial u}{\partial y} & 0 & \frac{\partial v}{\partial z} - \frac{\partial w}{\partial y} \\ \frac{\partial w}{\partial x} - \frac{\partial u}{\partial z} & \frac{\partial w}{\partial y} - \frac{\partial v}{\partial z} & 0 \end{pmatrix} \quad (7.1)$$

More compactly this can be written as:

$$\nabla \mathbf{v} = \underbrace{\frac{1}{2} \left(\frac{\partial u_i}{\partial x_j} + \frac{\partial u_j}{\partial x_i} \right) \mathbf{e}_i \mathbf{e}_j}_{\mathbf{D}} + \underbrace{\frac{1}{2} \left(\frac{\partial u_i}{\partial x_j} - \frac{\partial u_j}{\partial x_i} \right) \mathbf{e}_i \mathbf{e}_j}_{\mathbf{\Omega}} = \mathbf{D} + \mathbf{\Omega} \quad (7.2)$$

where \mathbf{e}_i stands for the unit vector in the direction i , and the Einstein summation convention is implied.

The antisymmetric part $\mathbf{\Omega}$ is also known as the *spin tensor*, and represents solid-body rotation. The square of its magnitude is half the square of the magnitude of the vorticity vector $\boldsymbol{\omega} = \nabla \times \mathbf{v}$:

$$\begin{aligned} \|\mathbf{\Omega}\|^2 &= \Omega_{ij}\Omega_{ij} \\ &= \frac{1}{2} \left(\left(\frac{\partial u}{\partial y} \right)^2 + \left(\frac{\partial u}{\partial z} \right)^2 + \left(\frac{\partial v}{\partial x} \right)^2 + \left(\frac{\partial v}{\partial z} \right)^2 + \left(\frac{\partial w}{\partial x} \right)^2 + \left(\frac{\partial w}{\partial y} \right)^2 \right) \\ &\quad - \left(\frac{\partial u}{\partial y} \frac{\partial v}{\partial x} + \frac{\partial w}{\partial x} \frac{\partial u}{\partial z} + \frac{\partial v}{\partial z} \frac{\partial w}{\partial y} \right) \\ &= \frac{1}{2} \|\boldsymbol{\omega}\|^2 \end{aligned} \quad (7.3)$$

The symmetric part is called the *deformation tensor* or *rate-of-strain tensor*. It represents several types of deformation including expansion, elongation, and shearing. Its magnitude is

$$\begin{aligned}
\| \mathbf{D} \|^2 &= d_{ij}d_{ij} \\
&= \left(\frac{\partial u}{\partial x} \right)^2 + \left(\frac{\partial v}{\partial y} \right)^2 + \left(\frac{\partial w}{\partial z} \right)^2 \\
&\quad + \frac{1}{2} \left(\left(\frac{\partial u}{\partial y} \right)^2 + \left(\frac{\partial u}{\partial z} \right)^2 + \left(\frac{\partial v}{\partial x} \right)^2 + \left(\frac{\partial v}{\partial z} \right)^2 + \left(\frac{\partial w}{\partial x} \right)^2 + \left(\frac{\partial w}{\partial y} \right)^2 \right) \\
&\quad + \left(\frac{\partial u}{\partial y} \frac{\partial v}{\partial x} + \frac{\partial w}{\partial x} \frac{\partial u}{\partial z} + \frac{\partial v}{\partial z} \frac{\partial w}{\partial y} \right)
\end{aligned} \tag{7.4}$$

The diagnostic pressure equation can be written as

$$-\frac{1}{\rho_0} \nabla^2 p' = \left(\frac{\partial u}{\partial x} \right)^2 + \left(\frac{\partial v}{\partial y} \right)^2 + \left(\frac{\partial w}{\partial z} \right)^2 + 2 \frac{\partial u}{\partial y} \frac{\partial v}{\partial x} + 2 \frac{\partial u}{\partial z} \frac{\partial w}{\partial x} + 2 \frac{\partial v}{\partial z} \frac{\partial w}{\partial y} - \frac{\partial B_T}{\partial z} \tag{7.5}$$

Which, using the previous two equations, can be expressed as

$$-\frac{1}{\rho_0} \nabla^2 p' = \| \mathbf{D} \|^2 - \| \boldsymbol{\Omega} \|^2 - \frac{\partial B_T}{\partial z} \tag{7.6}$$

or alternatively as

$$-\frac{1}{\rho_0} \nabla^2 p' = \| \mathbf{D} \|^2 - \frac{1}{2} \| \boldsymbol{\omega} \|^2 - \frac{\partial B_T}{\partial z} \tag{7.7}$$

Appendix B

Implementation of the Barnes interpolation algorithm

The interpolation scheme developed by Barnes (1964) and described in detail by Koch et al. (1983) was used to analyse both surface observations and radiosondes in Chapter 5. This scheme can be used in an iterative way to reduce the remaining errors, as will be explained.

As a first step, pass Barnes scheme estimates the value q_p of a field q at some gridded point p by taking a weighted mean of observed points $i...$

$$q_p = \frac{\sum w_i q_i}{\sum w_i} \quad (7.8)$$

Here w_i is the relative weight given to point i . The weight is determined by the expression

$$w_i = \exp\left(-\frac{d_i^2}{D^2}\right) \quad (7.9)$$

Here, d_i is the distance between point i and the target point. D is a constant that may be called the *radius of influence*. For the radiosonde data of the U.K., $D= 100$ km was used. For the U.K. surface data, D was set to 50 km.

After this first pass, an error $\Delta q_i = q - q_i$ can be calculated at each point i . These error values can be interpolated just like the original field q to yield a gridded error field. Subsequently, the error field is subtracted from the original gridded field to yield an improved gridded field. For the computation of the gridded error field, the weighting function is slightly different and incorporates a factor γ , where $0 \leq \gamma \leq 1$, which has the effect of emphasizing the errors at smaller scales:

$$w_i = \exp\left(-\frac{d_i^2}{\gamma D^2}\right) \quad (7.10)$$

A value of 0.3 was used for γ for the interpolation of the surface data. For the radiosonde data interpolation, an additional error pass did not change the initial analysis field by much, regardless of the value of γ that was chosen, so that it was decided to omit the error correction pass altogether.

Acknowledgements

This work has been carried out at the Institut für Meteorologie und Klimaforschung (IMK) at the Forschungszentrum Karlsruhe (now Campus Nord of the Karlsruhe Institute of Technology, KIT).

I would like to thank Prof. Dr. Ch. Kottmeier for making it possible for me to write my Ph.D. thesis at the IMK and for his support.

Thanks are also due to Prof. Dr. K. D. Beheng for accepting to be co-reviewer of this work.

I am indebted to Dr. Ulrich Corsmeier, who was my advisor during my three-and-a-half years at the IMK. He has given me good advice whenever I needed it, for example, when I had doubts about choosing a specific direction in my work. Special thanks are due to him for reading through the manuscript of this thesis and providing me with valuable suggestions for improvement.

I want to thank Christian Barthlott for helping me to set up and start working with the COSMO model.

To Samiro Khodayar, with whom I shared a room and a research topic, I would like to express thanks for the cooperation. Thanks are due to many colleagues at IMK for their assistance. Andreas Wieser helped me work with lidar data and Jan Handwerker provided me with radar data. Many others helped me out in one way or another.

I would also like to thank the other Ph.D. students of the IMK who created a good atmosphere through the years.

To Mrs. Knierim I am very thankful for reading through the manuscript and indicating where my English formulations needed improvement.

Last but not least I want to thank my wife Yi, who takes so good care of me that she should receive a substantial part of the credit for this work, and to my family in the Netherlands who have supported me all the time.